



SCUOLA DOTTORALE IN SCIENZE MATEMATICHE E FISICHE

DOTTORATO DI RICERCA IN FISICA - XXVIII CICLO

# Study of colloidal suspensions of multi-responsive microgels

*Candidate: Valentina Nigro*

Advisor:

Prof. M.A.Ricci

Co-Advisors:

Dr. B.Ruzicka, Dr. R.Angelini

Ph.D. Coordinator:

Prof. R.Raimondi

*A thesis submitted in partial fulfillment of the requirements  
for the degree of Doctor of Philosophy in Physics*

January 2016

A Francesca

# Contents

<b>Introduction</b>	<b>1</b>
<b>1 Colloidal suspensions of IPN microgels</b>	<b>4</b>
1.1 Colloidal Systems . . . . .	4
1.1.1 Out-of-Equilibrium Colloidal States . . . . .	5
1.2 Colloidal Suspensions of Responsive Microgels . . . . .	11
1.2.1 Swelling Behavior . . . . .	12
1.2.2 Intra-particle structural behavior . . . . .	16
1.3 PNIPAM microgels . . . . .	21
1.3.1 Swelling and Phase Behavior . . . . .	23
1.3.1.1 Agents affecting the swelling behavior . . . . .	26
1.4 IPN microgels of PNIPAM and PAAc . . . . .	28
1.4.1 Swelling and Phase Behavior . . . . .	29
<b>2 Experimental Section</b>	<b>32</b>
2.1 Light Scattering . . . . .	32
2.1.1 Basic Theory of Light Scattering . . . . .	33
2.1.2 Dynamic Light Scattering . . . . .	40
2.1.3 Multi Angles Dynamic Light Scattering Setup . . . . .	43
2.2 Neutron Scattering . . . . .	46
2.2.1 Basic Theory of Neutron Scattering . . . . .	48
2.2.2 Small-Angle Neutron Scattering . . . . .	58
2.3 Materials and Samples preparation . . . . .	65
2.3.1 Synthesis Procedure . . . . .	65
2.3.2 Samples preparation . . . . .	68
<b>3 Results and Discussion</b>	<b>70</b>
3.1 Dynamics: Dynamic Light Scattering . . . . .	70
3.1.1 PNIPAM microgel suspensions in H <sub>2</sub> O solvent . . . . .	72
3.1.2 IPN microgel suspensions in H <sub>2</sub> O solvent . . . . .	75
3.1.3 Deprotonated IPN microgel suspensions in H <sub>2</sub> O solvent . . . . .	81

---

3.1.4	IPN and Deprotonated IPN microgel suspensions in D <sub>2</sub> O solvent . . . . .	89
3.2	Local Structure: Small-Angle Neutron Scattering . . . . .	97
3.2.1	PNIPAM microgel suspensions in D <sub>2</sub> O solvent . . . . .	97
3.2.2	IPN microgel suspensions in D <sub>2</sub> O solvent . . . . .	101
3.2.3	Deprotonated IPN microgel suspensions in D <sub>2</sub> O solvent . . . . .	107
3.3	Phase Diagram of IPN microgels . . . . .	112
	<b>Conclusions</b>	<b>116</b>
	<b>Bibliography</b>	<b>119</b>

# Introduction

Complex fluids, such as colloids, foams, emulsions and polymer solutions, appear in every day life and are characterized by properties between those of liquids and crystalline solids. Despite being very different at macroscopic level, they exhibit similar characteristics on mesoscopic and microscopic length scales and exotic and intriguing phase behaviors.

In this context colloidal systems have long been the subject of intense research either for technological applications and for theoretical implications. Indeed due to their larger tunability with respect to atomic and molecular glasses, they are very good model systems for understanding the general problem of dynamic arrest. The typical size of the constituent particles in fact makes colloids experimentally more accessible, since they can be easily investigated through conventional techniques, such as light scattering and microscopy. Moreover their interparticle potential can be easily controlled by tuning external parameters such as packing fraction, waiting time and ionic strength, thus leading to complex phase diagrams with different arrested states (such as gels (1, 2, 3) and glasses (4, 5)) and unusual glass-glass transitions (6, 7, 8), theoretically predicted and recently experimentally observed.

In particular among colloidal systems, soft colloids represent an interesting class of glass-forming systems, characterized by an interparticle potential with a finite repulsion at or beyond contact. As a result of the particle softness, a complex phase behavior emerges, thus providing new insight into glass formation. The complexity of the theoretically predicted phase behavior (9, 10, 11) has not yet been experimentally reproduced and many efforts are recently devoted to understanding the exact nature of the interparticle potentials.

In this framework microgels, aqueous dispersions of nanometre- or micrometre-sized hydrogel particles, such as PNIPAM microgels, have attracted great interest as repulsive-soft colloids (12, 13, 14), due to the possibility of changing their effective volume fraction by tuning their response to the external stimuli. They have been largely investigated in the last years because of their versatility and high sensitivity to stimuli such as pH, temperature, electric field, ionic strength, solvent, external stress or light and are therefore particularly attractive smart materials (15, 16, 17, 18). These features make these systems largely used for many applica-

tions in a lot of different fields, such as in agriculture, construction, cosmetic and pharmaceuticals industries, in artificial organs and tissue engineering (19, 20, 21, 22). On the other hand fundamental studies on this class of systems, have highlighted the richness of microgel properties, since they allow to modulate the interaction potential through easily accessible experimental parameters and give rise to unusual transition between different arrested states (13, 14, 23, 24, 25).

In particular the system investigated in this thesis is a colloidal suspension of Interpenetrated Polymer Network (IPN) microgels (26, 27, 28, 29), composed by two interpenetrated homopolymeric networks of a thermo-sensitive polymer, the poly(N-isopropylacrylamide), usually known as PNIPAM, and a pH-sensitive one, the poly(acrylic acid), usually known as PAAc. An additional pH-sensitivity with respect to pure PNIPAM microgel is introduced by adding the PAAc, due to its different solubility at acidic and neutral pH (28, 30, 31, 32, 33), and a more complex phase behavior is expected, even more interesting both for technological applications and theoretical implications. Indeed through the pH-sensitivity an additional control of the particles size and a balance between repulsive and attractive interactions can be obtained, thus providing a new control parameter to explore the phase behavior of soft-repulsive colloids.

To give further contributions to the understanding of the phase behavior of colloidal suspensions of PNIPAM-PAAc IPN microgel, we present in this thesis an investigation of their dynamics and local structure both in  $H_2O$  and  $D_2O$  solutions. The aim of this thesis is to investigate the typical swelling behavior of this system and to provide a preliminary picture of its phase diagram as a function of temperature, pH and concentration. To this purpose the most suitable synthesis procedure has been firstly identified to obtain an IPN microgel with the desired characteristics, i.e. particle size, required degree of softness (defined in term of elasticity) and thermo- and pH-responsiveness. An effort has been made to achieve a good control of all these parameters and the support of Dynamic Light Scattering (DLS) measurements has been crucial to identify the best synthesis protocol.

A systematic characterization of the swelling behavior of aqueous suspensions IPN microgel has been performed through Dynamic Light Scattering in a  $Q$ -range ( $6.2 \times 10^{-4} < Q < 2.1 \times 10^{-3}$ )  $\text{\AA}^{-1}$  and in the temperature range  $T = (293 \div 313)$  K, in order to study the transition from the swollen to the shrunken state as temperature increases. Moreover the concentration and pH-dependence of the swelling behavior has been carefully investigated in the weight concentrations range  $C_w = (0.10 \div 1.70)$  %. Finally,  $D_2O$  suspensions of IPN microgels have been characterized through DLS, to understand the role played by the solvent in the phase behavior and to open the way for neutron scattering measurements that need the use of  $D_2O$  to gain contrast.

Small-Angle Neutron Scattering (SANS) measurements have been performed in a  $Q$ -range ( $0.004 \div 0.7$ )  $\text{\AA}^{-1}$  at the same concentrations and temperature ranges

of DLS, to probe the intraparticle structure during the cross-over from the fully swollen to the completely shrunken state.

The thesis is organized in three sections. Chapter 1 reports the achieved state of the art on PNIPAM-based microgels and in particular on PNIPAM-PAAc IPN microgel subject of this thesis. Chapter 2 introduces the basic theory of light and neutron scattering, with particular attention to Dynamic Light Scattering and Small-Angle Neutron Scattering techniques and describe the protocol for sample preparation. Chapter 3 is dedicated to discuss the obtained results and to provide new insights in the understanding of the dynamical and intra-particle structural behaviors of colloidal suspensions of IPN microgels.

# Chapter 1

## Colloidal suspensions of IPN microgels

In this chapter the system studied in this thesis, a colloidal suspension of IPN microgels based on PNIPAM and PAAc, is introduced. A description of the main features of swelling and intra-particle structural behaviors are presented together with recent advances in the understanding of the complex phase diagram of PNIPAM and PNIPAM-PAAc microgels.

### 1.1 Colloidal Systems

The simplest definition of a colloidal suspension is that of a system composed by two separated phases, where particles of any nature, with colloidal size between 1 nm up to 1  $\mu\text{m}$ , are suspended (due to frequent collisions with the solvent molecules) in a continuous medium of different composition.

These systems have long been the subject of intense research, due to the wide range of their technological applications and to their theoretical and experimental implications for understanding the general phenomenon of dynamical arrest. In the last years glass transition in colloidal suspensions has attracted great attention since it has many features in common with those of glass transition in molecular materials and great advances in the understanding of the structural arrest phenomena, that is on the transition from an ergodic to a non-ergodic dynamics and in particular on the gel and/or glass transition, have been obtained.

This has been possible because colloidal suspensions exhibit great advantages with respect to their atomic and molecular counterparts. In fact from an experimental point of view, their characteristic length and time scales are large enough to allow their investigation through light scattering and confocal microscopy techniques, with a resolution up to a single-particle. Moreover the involved time scales



and their slow dynamics make colloids good model systems for studying out-of-equilibrium states. Finally despite being very complex systems, they can be well described theoretically as particles interacting via simple effective potentials. The possibility of tuning the particle-particle interactions, usually not allowed in standard atomic systems, gives the additional possibility to synthesize *ad hoc* colloidal particles with specific properties, thus ensuring a great control of the interparticle interactions. Once a potential model is taken into account, the theoretical tools of statistical mechanics for molecular liquids can be usefully exported.

In particular the control of their interparticle potential (34) by tuning external parameters such as packing fraction, waiting time or ionic strength, has given rise to exotic phase diagrams with different arrested states, such as gels (1, 2, 3, 35) and glasses (4, 5, 36) and unusual glass-glass transitions (6, 7, 8, 37, 38).

Although many advances have been obtained in understanding dynamical arrest in colloidal systems, it is still unclear whether any existing theory provides a correct and complete description of the dynamics and the related glass transition. Indeed experimental and theoretical studies on systems of hard spherical particles with infinitive repulsive interactions at contact (Hard-Spheres (HS) model), have clarified several aspects of the glass-transition (4, 39). Nevertheless Hard-Spheres colloids do not exhibit the same versatility as molecular glasses. In this framework an interesting class of glass-forming systems is that of soft colloids which, at variance with hard colloids, are characterized by an interparticle potential with a finite repulsion at or beyond contact. As a result of particle softness, a more complex phase behavior emerges, thus providing new insight into glass formation in molecular systems. Nevertheless these more complex colloidal systems cannot be easily explained in term of the theories usually applied to repulsive potentials. In addition theoretical studies (9, 10, 11) have suggested the existence of an even more complex phase behavior, not yet experimentally reproduced up to now.

### 1.1.1 Out-of-Equilibrium Colloidal States

Glass formation is a generic phenomenon, observed in distinct systems encompassing hard and soft particles. At variance with condensed physics systems, where a glass is obtained by temperature quenching thus freezing atoms in an amorphous configuration, in soft glassy materials, such as colloids, this can be achieved by decreasing temperature or by increasing packing fraction or waiting time. In this way dynamics is slowed down and the system stops relaxing towards equilibrium, thus resulting frozen in a so-called *out-of-equilibrium state*. In this sense the glass transition is a kinetic rather than a thermodynamic transition, being all the thermodynamic functions continuous upon crossing the arrest transition.

The ideal Mode Coupling Theory (MCT), developed by *Götze* and coworkers (40, 41), provides the statistical tools to describe the dynamical behavior of colloidal systems approaching the glass transition, in terms of the normalized density

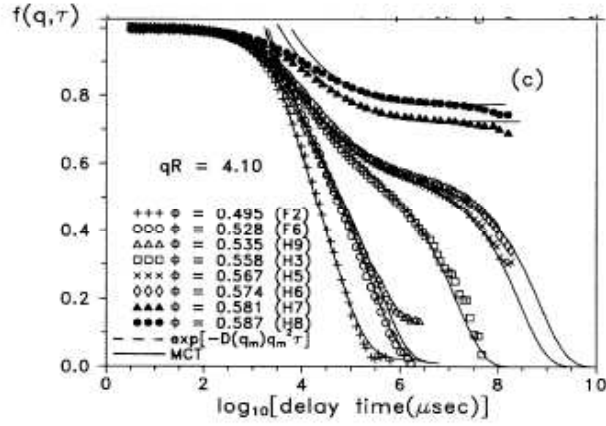


**Figure 1.1:** Comparison between intermediate scattering functions obtained by experiments (symbols) and those predicted by the MCT (solid curves), as reported in (42). By increasing the packing fraction  $\phi$  the two-relaxations behavior is observed due to the freezing of the density fluctuations.

autocorrelation function:

$$F(Q, t) = \frac{\langle \rho^*(Q, 0) \rho(Q, t) \rangle}{NS(Q)} \quad (1.1)$$

where  $N$  is the number of particle,  $\rho(Q, t) = \sum_{j=1}^N \exp(i\mathbf{Q} \cdot \mathbf{r}_j(t))$  is the Fourier transform of the local density variable and  $S(Q) = \langle |\rho(Q)|^2 \rangle / N$  is the static structure factor.

The main hypothesis of the MCT is the non-linear coupling of the density fluctuations. By increasing the strength of this coupling, either by decreasing the temperature or increasing the density, a dynamic instability occurs and the structure of the system becomes permanently frozen. Being in a non-ergodic state, the system can explore only a restricted number of all the available configurations in the phase space

In the HS systems, the MCT predicts the existence of a critical volume fraction  $\phi$  where the system undergoes from a simple liquid behavior to a slowing down of the dynamics, usually defined as ergodic-to-non-ergodic transition (4). This system can be experimentally realized with PMMA (Poly(methyl methacrylate)) particles and it allows the first direct comparison between theory and experiments (42, 43). Indeed light scattering measurements on these systems, directly provide the observable  $F(Q, t)$  (Eq.(1.1)) to be compared with MCT results, and have shown that the glass transition is approached upon super-compressing the system, leading to a phase behavior which is completely described throughout the pack-

ing fraction  $\phi$ , defined as the effective occupied volume fraction. This allows a qualitative comparison between theory and experiments (44, 45, 46). As shown in Fig.1.1,  $F(Q, t)$  exhibits the typical two-step relaxation predicted by the MCT with increasing  $\phi$ . The initial fast microscopic relaxation, the so-called  $\beta$  relaxation (see Fig.1.2), corresponding to the vibrations of particles around their initial configuration, is followed by a plateau which becomes longer and longer upon increasing  $\phi$ . The presence of such plateau indicates that particles are trapped in cages formed by their nearest-neighbors and the height of such plateau, coinciding with the long-time limit of  $F(Q, t)$ , defines the non-ergodicity parameter  $f_Q$ . A second slow structural relaxation, named  $\alpha$ -relaxation, is observed when upon breaking such a cage the particles escapes from its initial configuration, thus restoring ergodicity (see Fig.1.2). This behavior is well described by a "master curve" with a single-exponential decay, given by the so-called Kohlrausch-Williams-Watts equation:

$$F(Q, t) \sim e^{-\left(\frac{t}{\tau}\right)^\beta} \quad (1.2)$$

where  $\tau$  is the  $\alpha$ -relaxation time. Otherwise, if the system remains trapped in a non-ergodic state, at least on the timescale of experiments, typically larger than  $10^2 s$ , the  $\alpha$ -relaxation time diverges, due to the progressive frozen-in of the density fluctuations, and the out-of-equilibrium state is reached. Nevertheless the quantitative agreement between MCT and experiments is satisfactory only for HS repulsive systems, whilst the behavior of more complex colloidal systems in some cases cannot be easily explained in terms of the MCT applied to repulsive potentials.

By adding a short range attraction to the interparticle potential (experimentally obtained by adding non-adsorbing polymers to PMMA hard-sphere colloidal particles (34)) a more complex phase behavior emerges and two distinct glassy states at high density are identified (6, 7, 36, 41, 47): a repulsion-dominated glass, where non-ergodicity is due to the topological trapping of the particles in "cages", and an attraction-dominated glass, where particles are trapped by nearest-neighbor "bonds". The competition between these two glasses also leads to a re-entrance in the glassy phase diagram where a pocket of liquid is found between these two glasses.

The scenario of short-ranged attraction is even more complex in the region of low particle concentrations, where a gel state is found (48). It is known that colloids with strong enough interparticle short-range attraction can form gels if the particle volume fraction  $\phi$  is sufficiently low ( $\phi \approx 10^{-2}$ ). Gelation is usually associated to the formation of an infinite network with finite shear modulus and infinite zero-shear viscosity, leading the system to stop flowing at the gelation point. Gelation arises from particle aggregation into mesoscopic clusters and networks, due to interparticle attraction, which can be generated by both physical and chemical

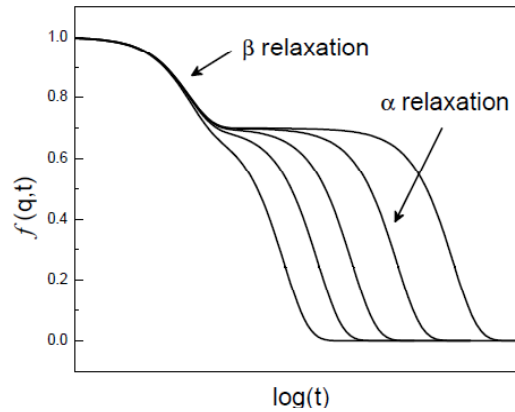


**Figure 1.2:** Typical two-steps relaxation of the autocorrelation function, where the fast  $\beta$  relaxation is associated to the vibrational motion and the slow  $\alpha$  relaxation to the structural rearrangements of the particles.

mechanisms. Chemical gelation is an irreversible process well described in terms of the percolation theory developed by Flory (49) and Stockmayer (50). This formalizes the gelation process in term of the infinite spanning network with bonds of infinite lifetime. Consequently, chemical gelation is associated to the connectivity of the systems, rather than to its physical properties. Physical gelation is instead driven by depletion interactions, hydrogen bonds or hydrophobic effects and is typically observed in colloidal and soft particles as well as associative polymers. Therefore physical gels are characterized by bonds originated from physical interactions of the order of  $k_B T$ , implying that clusters of bonded particles are continuously created and destroyed. An extension of the percolative theory to the physical gelation is problematic, due to the finite lifetime of bonds. Nevertheless if a spanning cluster approaches large dimension, for a time larger than the observation one, although finite, it is possible to draw in the phase diagram a line, which plays the role of a percolative line, and to assume that the system is undergoing a non-ergodic transition across this line. On the other hand, this is not a sufficient condition, since very strong and directional interactions may lead to longer bond lifetimes, eventually leading to phase-separation. Therefore at low density we need to distinguish between system undergoing gelation with or without phase separation.

Many experiments have recently shown that gelation of spherical particles with isotropic, short-range attractions is initiated by spinodal decomposition. This thermodynamic instability triggers the formation of density fluctuations, leading to spanning clusters that dynamically arrest to create a gel. This suggest that (non-equilibrium) gelation can be interpreted as a direct consequence of the equilibrium

liquid-gas phase separation (1, 35) and that the relation between the gel locus, the percolation and the liquid-gas spinodal lines is crucial. Moreover it has been recently shown that for a particular class of systems, characterized by anisotropic interactions, a novel scenario emerges. In this case gelation can be approached in equilibrium and is characterized by arrested networks of bonded particles which do not require an underlying phase separation (35).

Even if some advances have been done, solid understanding of the low-density region of the colloids phase diagram and of the processes leading to gel formation is actually limited by both experimental and theoretical drawbacks. Experimental results are often in contradiction one with each other and, sometimes, the investigated systems are too complicated to be used as a general model system for the gel transition. On the other hand a theoretical unifying framework for the description of the colloidal gel transition is not yet available and application of the MCT when short-ranged attractive forces are dominant is questionable.

The phenomenology is even enriched and still largely unexplored in the case of soft colloids which, at variance with hard spheres, are able to interpenetrate or compress, allowing for the existence of very dense states with interpenetration of particles. Indeed soft particles are usually characterized by a polymeric structure, which is able to reorganize according to the external conditions. Therefore their interparticle potential must account for both the at least partial overlap between particles and/or the change of their volume due to their swelling/shrinking behavior and thus exhibits a finite repulsion at or beyond contact. The resulting phase diagram is clearly distinct from that of the hard-sphere systems and knowledge of the effective interparticle potential is not always trivial. Indeed as a result of the particle softness, interesting equilibrium and non-equilibrium phases have been theoretically predicted (9, 10, 11, 34), although not yet experimentally reproduced (51, 52). In this framework great attention has been focused on colloidal suspensions of responsive-microgels with a physical nature between that of classical hard sphere colloids and ultra-soft polymeric colloids. Their softness can be tuned both via chemical synthesis or by changing those experimental parameters that affect their size and thus the effective occupied volume fraction, such as temperature, pH or hydrostatic pressure (12, 13, 14). Thanks to this possibility of tuning the volume fraction without changing the constant number density of particles, microgels have been widely used as experimentally convenient tools to explore the phase behavior of hard and soft colloids. However due to the high complexity of their composition and to their both colloidal and polymer-like nature, microgel dispersions have emerged as a more fascinating system with a rich and intriguing phenomenology which can give new insights in the understanding of the glass/gel transition.

**Dynamic and Static features of Glasses and Gels** Glasses and gels are therefore both out-of-equilibrium metastable states resulting from a slowing down

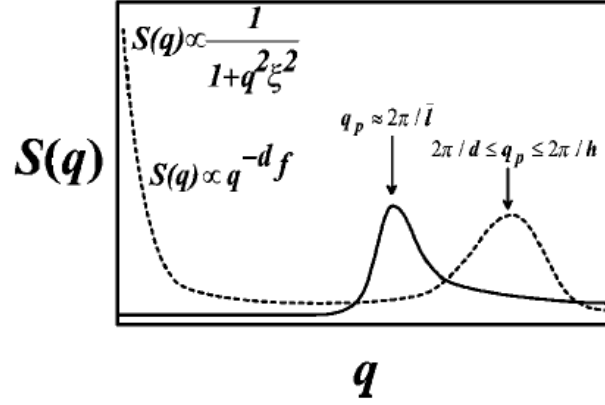


**Figure 1.3:** Static structure factor of a gel (dashed line) and a glass (full line) as reported by Tanaka et al. (53)

of the dynamics which leads the system to stop relaxing towards the equilibrium. This process is associated with a dramatic increase of the viscosity which can be quantitatively expressed in terms of the viscosity coefficient obtained through visco-elasticity measurements or in terms of the relaxation time  $\tau$  provided by DLS measurements.

In particular the dynamics of the systems on approaching the glass/gel transition can be characterized through the dynamical density fluctuations, provided by DLS experiments, to be compared with the MCT. It has to be noticed that the slow dynamics for the glass and the gel transition reflects different microscopic structural rearrangements. However the  $F(Q, t)$  exhibit similar kinetic behaviors with the typical two-steps relaxation in both cases and the nature of the arrested state cannot be evidenced through the density auto-correlation functions.

To distinguish gels from glasses usually structural inhomogeneities are detected, being generally glasses structurally homogeneous at all length scales at odds with gels. Indeed both of them are disordered solids: they do not flow and have finite elastic modulus, and are characterized by long-range disorder. Different structural signatures are evidenced in the static structure factor  $S(Q)$ : for a glass  $S(Q)$  (represented in Fig.1.3 by a full line) is flat at low  $Q$  values and exhibits a peak at a  $Q$ -value that corresponds to the average interparticle distance ( $r = 2\pi/Q_{max}$ ). The static structure factor of a gel (represented in Fig.1.3 by a dashed line) has instead a significant signal at low- $Q$  reflecting that they are locally dense, but with empty regions. The presence of such empty space, whose typical size depends on thermodynamic parameters, such as density, attraction strength and so on, allows in gels some residual motions at short length scales and therefore their compressibility. Moreover the  $S(Q)$  has a peak at higher  $Q$ -values respect to that of a glass since the attractive nature of gels gives rise to a percolated aggregates network with a shorter interparticle distance with respect to glasses. Since gels

can be formed through different routes, the behavior of  $S(Q)$  at low  $Q$  is often indicative of the underlying interactions determining the final arrested state.

## 1.2 Colloidal Suspensions of Responsive Microgels

Among soft colloids, systems like hydrogels, with an interparticle potential strongly dependent on external parameter, have attracted great interest due to their smart response to changes in the external stimuli.

Hydrogels are networks of polymer chains containing hydrophilic groups which are able to swell and retain large amounts of water. The majority of stimuli responsive hydrogels were created using conventional methods of synthesis of a relatively small number of synthetic polymers, especially (meth)acrylate derivatives and their copolymers. In 1968, Dušek and Paterson (54) theroretically predicted that changes in external conditions might result in abrupt changes of the hydrogels degree of swelling, ten years later these predictions were experimentally verified by Tanaka and others (55, 56). Lately numerous responsive hydrogels have been designed and synthesized by copolymerizing, grafting or interpenetrating stimuli-responsive monomers in the presence of a cross-linker and/or by cross-linking different polymer chains.

The resulting polymer gels are characterized by very weak mechanical properties, i.e. they are soft and brittle, and cannot withstand large deformation. This is mainly due to the fact that gels are far from fully-connected polymer networks, and contain various types of inhomogeneities, such as dangling chains and loops.

In this context microgels are nanometers or micrometer sized hydrogel particles which in water exhibit intermediate properties between soluble polymers, responsive macrogel able to swell and insoluble colloidal particles. On one hand the typical feature of the microgel particles are strictly related to the balance between polymer-polymer and polymer-solvent interactions, as observed for polymers soluble in water. On the other hand they exhibit a cross-linking density, a degree and a characteristic time of swelling which are typical of aqueous macrogels. Finally, like colloids based on hydrophobic polymers, colloidal microgels can be prepared to obtain a monodisperse size distribution. Therefore both their colloidal and polymer-like nature have to be taken into account to describe their phase behavior.

For these reasons, aqueous dispersions of responsive microgel allow to modulate the interaction potential through easily accessible parameters usually not relevant in ordinary colloids, thus showing the evidence of unusual transitions between different arrested states (12). In particular responsive microgels can reversibly change their volume (swelling/shrinking behavior) in response to slight changes in the properties of the medium. Their volume phase transition affects the solvent-mediated interparticle forces and leads to a novel phase-behavior drastically dif-

ferent from those of conventional hard-spheres-like colloidal systems. Indeed due to their softness, microgels can be highly packed to effective volume fraction far above those of hard colloids, with interesting consequences on their structural and dynamical behavior. Moreover the swelling behavior has been shown to be the driving mechanism for tuning the effective packing fraction, thus enabling an experimental control parameter to explore the phase behavior. Therefore they are good candidates as ideal model systems for providing new insight into the glass-formation in molecular systems, due to the possibility to tune the particle softness not only through the synthesis procedure, but also through the response of the polymer to variations in temperature, pH, ionic strength, solvent, external stress or light.

On the other hand these features make responsive-microgels particularly interesting smart materials (15, 16, 18, 57) and have attracted great attention due to their impact on both industry and fundamental science. Indeed colloidal microgels have applications in agriculture, construction, cosmetics and pharmaceuticals industries, in artificial organs and tissue engineering (16, 18, 19, 21, 22, 58).

### 1.2.1 Swelling Behavior

The swelling behavior of thermo-responsive micro and macrogels has attracted great interest in the last years. Both theoretical and experimental works have highlighted the evidence of a Volume Phase Transition (VPT) from a swollen hydrated phase to a shrunken dehydrated one (see Fig.1.4) in response to changes in the external environment. Moreover it has been shown that the driving force and the equilibrium extent of the swelling behavior is the same for microgels and macrogels, while the dynamics result highly sensitive to the gel size. Indeed microgel particles retain the unique physical properties of bulk hydrogels, while their swelling/shrinking kinetics is much faster respect to macrogels: in response to temperature changes, microgels achieve the swollen state in less than a second, whereas macrogels can take a very long time because shrinking of the exterior layer prevents water transport from the interior. For many practical applications, rapid response to environmental stimuli is of crucial importance, thus a deep understanding of the swelling behavior of colloidal suspension of microgels is required.

Although the thermodynamic theory of gel swelling is a classical subject, there have been a number of recent theoretical works aimed at describing the swelling behavior of gels. In particular, gels based on thermo-sensitive polymers such as the Poly(N-isopropylacrylamide), usually known as PNIPAM, which we will better introduce in Par.1.3, have been largely studied. For example Lele et al. (59) applied an extended lattice theory that accounts for hydrogen bonding. Prausnitz's group (60) has applied semi-empirical extended Flory-Huggins theory (61) to predict the VPT for PNIPAM macrogels, by using model parameters arising from the experimental properties of linear PNIPAM solutions. Inomata et al. (62)



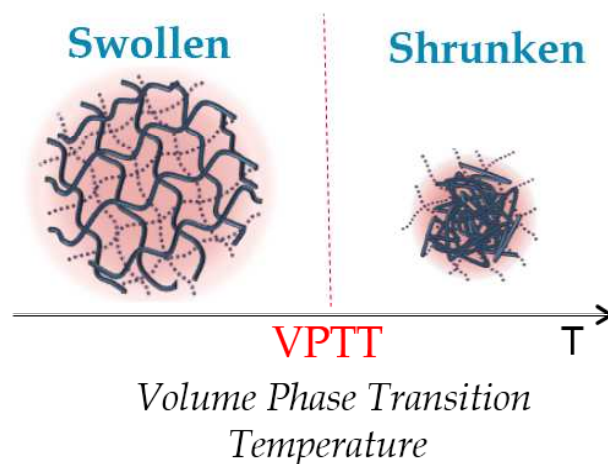


**Figure 1.4:** Schematic picture of the volume phase transition of microgel particles from a swollen hydrated phase to a shrunk dehydrated one by crossing the VPT temperature (VPTT).

interpreted PNIPAM microgel swelling by starting from one of the Prausnitz's earlier models in order to calculate the osmotic pressure in equilibrated swollen systems, thus highlighting the cross-linker influence on the PNIPAM-water interaction. Therefore it has been shown that the driving force for swelling can be estimated from the properties of linear PNIPAM solutions, whereas the gel elasticity opposing swelling comes mainly from the network topology, which depends on the cross-linker concentration. In conclusion, to predict the microgel swelling a number of semi-empirical extensions to Flory-Huggins theory are available.

### Interparticle Potential and Swelling Behavior

Responsive microgels based on thermo-sensitive polymers, such those investigated in this work, exhibit a phase behavior driven by the response to temperature changes. In this framework the major problem up to now has been finding an appropriate interparticle potential between microgel particles which takes into account the double polymeric/colloidal nature of microgel suspensions and is able to describe its complex phase behavior. Nevertheless it is well known that the VPT of microgel particles is closely related to the coil-to-globule transition of the polymer chains and it can be extensively explained by using the revised Flory-Huggins theory. In 1953 Flory and Rehner (61) proposed a modified theory by assuming uniform distribution of polymer and cross-linking points throughout the polymer network. Experimental investigations have instead highlighted the heterogeneous nature of microgel particles, hence an empirical modification of the Flory-Rehner theory has been proposed by Hino and Prausnitz (60). This theory has been successfully applied to describe the volume transition of bulk gels, however being the

physics of the volume transition independent on the particle size and the surface effect irrelevant, the same model can be also applied to microgel particles. Therefore it allows to correlate the particle diameter to temperature and to calculate the phase diagram by using a first-order perturbation theory for the fluid phase and an extended cell model for the crystalline solid phase. Here we report only the main results of this theory for the swelling behavior.

In a binary mixture containing the solvent and the cross-linked polymer particle, the change of chemical potential upon solution of a crosslinked polymer particle consists of a mixing contribution and an elastic contribution:

$$\Delta\mu = \Delta\mu^{mixing} + \Delta\mu^{elasticity} = \mu_{water}^{gel} - \mu_{water}^{pure} \quad (1.3)$$

When the swollen gel is in equilibrium with the surrounding solvent, thus  $\Delta\mu = 0$  and the chemical potential of water results equal inside and outside the microgel particle

$$\mu_{water}^{gel} = \mu_{water}^{pure} \quad (1.4)$$

where the chemical potential inside the gel,  $\mu_{water}^{gel}$ , includes the contribution equivalent to that of aqueous solutions of polymers, and a contribution arising from the cross-linking of polymer chains or equivalently from the gel elasticity. Therefore it can be written as

$$\mu_{water}^{gel} = \mu_{water}^{polymer\ solution} + \mu_{water}^{elasticity} \quad (1.5)$$

On the other hand the chemical potential of water in an aqueous solution of microgel particles can be calculated from the Flory-Huggins theory as

$$\Delta\mu^{mixing}/(k_B T) = \mu_{water}^{polymer\ solution} - \mu_{water}^{pure}/(k_B T) = \ln(1 - \phi) + \phi + \chi\phi^2 \quad (1.6)$$

where  $k_B$  is the Boltzmann constant,  $T$  is the absolute temperature,  $\chi$  is the Flory polymer-solvent energy parameter (empirically given as a function of temperature and composition) and  $\phi$  is the volume fraction of polymer inside the individual particles. The second term on the right-hand of Eq.(1.5) accounts for gel elasticity, through the effect of the network on the chemical potential of the solvent. According to Hino and Prausnitz, the chemical potential of water due to gel elasticity is given by

$$\Delta\mu^{elasticity}/(k_B T) = \mu_{water}^{elasticity}/(k_B T) = \frac{\phi_0}{N} \left[ \left( \frac{\phi}{\phi_0} \right)^{1/3} - \left( \frac{\phi}{\phi_0} \right)^{5/3} + \left( \frac{\phi}{2\phi_0} \right) \right] \quad (1.7)$$

where  $N$  is the average number of segments between two neighboring cross-linking points in the gel network and  $\phi_0$  is the polymer volume fraction in the reference state, where the conformation of the network chains is closest to that of unperturbed Gaussian chains. Approximately,  $\phi_0$  is equal to the volume fraction of polymer within the microgel particles as obtained at the condition of preparation. Therefore from Flory-Rehner theory the gel elasticity contribution can be directly evaluated by introducing the expansion factor  $\alpha$ , which can be calculated throughout the affine model (61) by assuming the network chains deforming affinely with the volume of a gel as

$$\alpha = \frac{\sigma}{\sigma_0} = \left(\frac{\phi}{\phi_0}\right)^{1/3} \quad (1.8)$$

where  $\sigma_0$  is the particle diameter at the reference state and  $\sigma$  is the particle diameter at a given state. According to this model, the equilibrium conditions of the solvent can be classified as follows:  $\theta$  solvents, when polymer coils act like ideal chains and the excess chemical potential of mixing between polymer and solvent is zero, implying that the expansion factor  $\alpha = 1$ ; good solvents, when interactions between polymer segments and solvent molecules are energetically favorable, allowing polymer coils to expand, and leading to  $\alpha > 1$ ; poor solvents, when polymer-polymer self-interactions are preferred, and the polymer coils contract, giving  $\alpha < 1$ .

Substitution of Eq.(1.6) and Eq.(1.7) into Eq.(1.5) yields to the equation of phase equilibrium

$$\frac{\Delta\mu}{k_B T} = \ln(1 - \phi) + \phi + \chi\phi^2 + \frac{\phi_0}{m} \left[ \left(\frac{\phi}{\phi_0}\right)^{1/3} - \left(\frac{\phi}{\phi_0}\right)^{5/3} + \left(\frac{\phi}{2\phi_0}\right) \right] = 0 \quad (1.9)$$

At a given temperature, Eq.(1.9) can be used to find the polymer volume fraction  $\phi$ .

The phase behavior of microgels dispersions can be quantitatively represented by a simple thermodynamic model, where the pair potential between neutral microgel particles is the sum of a short-range repulsive contribution and a longer-ranges van der Waals-like attraction arising from the differences between particles and solvent. Depending on the system, an appropriate interaction potential needs to be chosen. For the PNIPAM particles the most simple model proposed up to now is represented by a Sutherland-like function (63), where the hard-sphere diameter is related to the swelling of gel particles and can be calculated from Eq.(1.8) and the van der Waals attraction beyond the hard-sphere diameter can be represented by

$$u_A(r) = -\frac{H}{r^n} \quad (1.10)$$

where  $H$  is the Hamaker constant given in term of the number density  $\rho_m$  of polymeric groups within each particle as  $H \propto \rho_m^2$  and  $n$  accounts for the shorter range of attraction between colloidal particles compared to molecules.

The introduction of the Hamaker constant in Eq.(1.10), allows to obtain the attractive potential due to the van der Waals forces

$$\frac{u_A(r)}{k_B T} = -k_A \left(\frac{T_0}{T}\right) \left(\frac{\sigma_0}{\sigma}\right)^{6+n} \left(\frac{\sigma}{r}\right)^n \quad (1.11)$$

where  $k_A$  is a dimensionless constant and  $T_0$  is a reference temperature that is introduced for the purpose of dimensionality.

For a dispersion of microgel particles in the fluid state, we can calculate the Helmholtz energy, by using a first-order perturbation theory, because higher order terms are negligible when the perturbation arises only from short-range attractions. Accordingly, this energy for the fluid phase includes a hard-sphere contribution and a perturbation accounting for the van der Waals attraction (Eq.(1.11)). It is therefore given by

$$\frac{F_f}{N k_B T} = \ln(\eta) - 1 + \frac{4\eta - 3\eta^2}{(1 - \eta)^2} + 12\eta \int_1^\infty x^2 g_F^{HS}(x) \frac{u_A(x)}{k_B T} dx \quad (1.12)$$

where  $N$  represents the total number of particles,  $\eta = \pi\rho\sigma^3/6$  is the particle packing fraction,  $\rho$  is the particle number density, and  $g_F^{HS}(r)$  is the hard-sphere radial distribution function, calculated from the Percus-Yevick theory (64). By following the same perturbation approach, the Helmholtz energy for the solid phase is given by the contribution from the reference hard-sphere crystal and a perturbation taking into account the van der Waals attraction. Therefore the final expression for the Helmholtz energy of the solid phase is given by

$$\frac{F}{N k_B T} = -\frac{F_s^{HS}}{N k_B T} + 12\eta \int_1^\infty x^2 g_s^{HS}(x) \frac{u_A(x)}{k_B T} dx \quad (1.13)$$

where  $g_s^{HS}(r)$  is the radial distribution function for hard-sphere solid.

### 1.2.2 Intra-particle structural behavior

One of the most peculiar features of polymer gels, both on microscopic and macroscopic length scales, are the spatial inhomogeneities emerging in the forming process. Since both the elastic and the osmotic properties of polymer networks are affected by the structural defects, it is crucial to investigate their distribution and properties. Indeed the topological structure of polymer gels has been widely investigated in the last decades (65, 66, 67, 68, 69, 70), highlighting crucial differences

with respect to polymer solutions. In particular it has been shown (66) that the scattering from gels is always higher than that for polymer solutions, being strictly related to the degree of inhomogeneities.

In general polymer gels are composed by polymer chains connected by junctions or crosslinks randomly introduced in the space, with permanent chemical junctions required for achieving gelation. Several paths may be followed to obtain gels, each method bringing its own contribution to the disorder of the system. For example, gels obtained by copolymerization of the cross-linker together with the molecules of the principal monomer, frequently exhibit partial phase separation between the two constituents. On the other hand gels crosslinked in solution usually display elastic retraction. Independently on the synthesis procedure the resulting three dimensional structure is characterized by spatial irregularities and by a great variety of defects. Therefore unlike ideal gels with a homogeneous distribution of crosslinks, microgels always exhibit an inhomogeneous cross-link density distribution, closely connected to the spatial concentration fluctuations. The degree of spatial inhomogeneity has been shown to increase with the gel cross-link density, due to the simultaneous increasing of regions more or less rich of cross-links. On the other hand it has been shown (71) that the initial monomer concentration used in the gel preparation significantly affects the scattering intensities. Indeed the effective density of cross-links increases with the monomer concentration, so that the spatial inhomogeneity also increases. On the other hand, increasing monomer concentration, leads to a decrease of the swelling degree of gels which progressively reduces the concentration differences between densely and loosely cross-linked regions, so giving rise to a decrease of the apparent inhomogeneity.

One of the most useful models to illustrate inhomogeneities in polymer gels, is the mesh model proposed by Bastide and Leibler in 1998 (72). It has been schematically reported in Fig.1.5(a) and (b) (67), where blobs of polymer chains and crosslinks are represented by black lines and red dots. In a reaction bath, concentration fluctuations are suppressed and the distribution of crosslinks is not detected by scattering experiments. However, when the polymer is swollen, the clusters of first-chemical-neighbor junctions, which do not swell, become "visible" by scattering. Statistical fluctuations in the local density of crosslinking and defects of connectivity allow certain regions to swell more than others, thus creating permanent spatial variations in the polymer concentration that scatter visible light or other radiation.

Therefore scattering is the best way to measure these types of concentration fluctuations. Indeed scattering methods, such as light scattering, X-ray scattering and neutron scattering, have largely contributed to the structural characterization of polymeric systems. Light Scattering has been used to characterize polymers in solutions since the 1940s (73, 74), being Xenon or mercury light sources replaced by high-power lasers in the 1970s (75). Typical examples are the Guinier plot, Zimm plot and Kratky plot analysis, used to estimate average molecular weight,

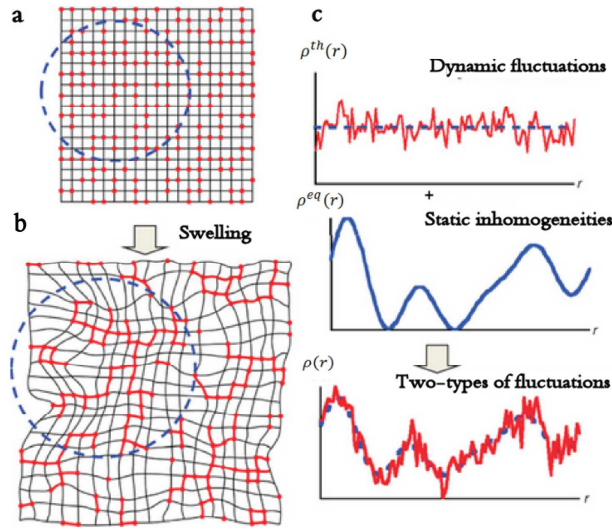


**Figure 1.5:** Schematic representations of the blob model proposed by Shibayama et al. (67) of (a) a two-dimensional reaction bath well above the chain gelation threshold, (b) an over-swollen gel by the addition of solvent and (c) dynamic, static and total concentration fluctuations as a function of space coordinate  $r$ . Red dots represent the randomly distributed interchain crosslinks.

radius of gyration and virial coefficients. Further progress has been determined by the availability of X-ray from synchrotron sources, and neutrons from intense steady state or pulsed sources.

In particular neutron scattering offers several advantages with respect to X-ray scattering, such as a suitable wavelength for nanometer-scale structural analysis, the sensitivity to elements and their isotopes, the high penetration power and finally the energy exchange between neutrons and nuclei, due to the finite mass of the neutron. Because of these properties, neutron scattering has been widely used to characterize both the structure and the dynamics of soft matter. Among the various types of neutron scattering, Small-Angle Neutron Scattering (SANS) is today one of the most powerful technique for structural characterization of polymeric systems on submicron length scales (66, 68, 69, 70, 76), thanks to the isotopic substitution technique. For long time polymer gels have been considered too complicated system for SANS studies, due to their complex chemical composition. On the other hand, the H/D isotopic contrast on the solvent, allows to easily perform SANS experiments without the need for deuterated polymer networks. A wealth of information on the structure of polymer gels can be obtained from SANS studies, provided that a suitable model of their spatial inhomogeneities is available. Recently, the understanding of the frozen inhomogeneities in gels has been greatly advanced owing to the theoretical development and experimental studies. Indeed it is now known that the spatial inhomogeneities are built-in frozen concentra-

tion fluctuations, which become dominant by deforming and/or swelling the gel. Therefore it is particularly important to separate the scattering intensity function into two distinct contributions, with different background and properties: the first accounts for the dynamic fluctuations, and the second for the static inhomogeneities, since they have different background and properties, as we will report in the following.

### Theoretical Background

In order to predict the structure factor by taking into account both thermal and (equilibrium) frozen concentration fluctuations,  $\rho^{th}(r)$  and  $\rho^{eq}(r)$ , respectively, Panyukov and Rabin (77) proposed a sophisticated statistical theory of polymer gels by applying a path-integral and replica method. The concentration fluctuations are therefore given by:

$$\rho(r) = \rho^{th}(r) + \rho^{eq}(r) \quad (1.14)$$

and the thermal and frozen structure factors,  $G(Q)$  and  $C(Q)$ , by the Fourier conjugates of  $\rho^{th}(r)$  and  $\rho^{eq}(r)$ , respectively:

$$G(Q) = \langle \rho^{th}(Q) \rho^{th}(-Q) \rangle \quad (1.15)$$

and

$$C(Q) = \langle \rho^{eq}(Q) \rho^{eq}(-Q) \rangle \quad (1.16)$$

here  $\langle \dots \rangle$  denoting thermal averaging. As a result, the structure factor of gels is given by

$$S(Q) \equiv \overline{\langle \rho(Q) \rho(-Q) \rangle} = G(Q) + C(Q) \quad (1.17)$$

denoting with  $\overline{\dots}$  the ensemble average. The thermal average of  $\rho^{eq}(Q)$  is non-zero, that is,  $\langle \rho^{eq}(Q) \rangle \neq 0$ , if the system is non-ergodic, whereas its ensemble average is always  $\overline{\rho^{eq}(Q)} = \overline{\langle \rho^{eq}(Q) \rangle} = 0$  by definition. These functions have been obtained for various types of polymer gels, including neutral gels, weakly charged gels and deformed gels. There are various types of inhomogeneities in gels, such as spatial inhomogeneities, topological inhomogeneities and connectivity inhomogeneities. SANS is one of the best experimental techniques to quantitatively study gel inhomogeneities since it provides information on the spatial concentration fluctuations (in Fourier space) and the concentration differences between polymer-rich and -poor regions. The simplified expressions of  $G(Q)$  and  $C(Q)$  are

$$G(Q) \approx I_{OZ}(Q) = \frac{I_{OZ}(0)}{1 + \xi^2 Q^2} \text{(Ornstein-Zernike)} \quad (1.18)$$

$$C(Q) \approx I_{SL}(Q) = \frac{I_{SL}(0)}{(1 + \Xi^2 Q^2)^2} \text{(squared Lorentz, Debye Bueche)} \quad (1.19)$$

being  $\xi$  the correlation length and  $\Xi$  the characteristic size of the inhomogeneities.

As a result the scattered intensity,  $I(Q)$ , consists of two contributions, the thermal correlator (isotropic and independent of the network deformations),  $G(Q)$ , and the static correlator,  $C(Q)$ . Therefore  $I(Q)$  is expressed as the sum of the scattered intensity from the corresponding solution,  $I_{sol}(Q)$ , plus an excess scattering,  $I_{ex}(Q)$ , over a wide range of  $Q$

$$I(Q) = I_{sol}(Q) + I_{ex}(Q) \quad (1.20)$$

$I(0) = I(Q = 0)$  depends on the osmotic modulus of the systems, defined as  $K = \phi \partial \Pi / \partial \phi$  (where  $\phi$  is the solute volume fraction and  $\Pi$  the osmotic pressure), and according to the classical theory of polymer gels (61) can be written as:

$$I(0) = (C_{polym}^2 / m_{polym}^2) \left\{ N_A \left[ b_{D_2O} \left( \frac{v_{polym}}{v_{D_2O}} \right) - b_{polym} \right]^2 \right\} \frac{RT}{K} \quad (1.21)$$

where  $C_i$ ,  $m_i$ ,  $v_i$  and  $b_i$  are the monomer concentration, the monomer molecular weight, the monomer volume and the scattering length of the  $i$ -component, respectively.  $N_A$ ,  $R$  and  $T$  are the Avogadro's number, the gas constant and the absolute temperature, respectively.

In particular for swollen gels, the polymer concentration lies typically in the semi-dilute regime and therefore  $I_{sol}(Q)$  is given by a Lorentz function

$$I_{sol}(Q) = \frac{I_{sol}(0)}{1 + \xi^2 Q^2} \quad (1.22)$$

where  $\xi$  is the correlation length, or blob size. On the other hand, several functional forms of  $I_{ex}(Q)$  have been proposed in the literature, such as a stretched exponential function

$$I_{ex}(Q) = I_{ex}(0) \exp[-(Q\xi)^\alpha] \quad (1.23)$$

or a Debye-Bueche function



$$I_{ex}(Q) = \frac{I_{ex}(0)}{(1 + \Xi^2 Q^2)^2} \quad (1.24)$$

where  $\chi$  and  $\Xi$  are some characteristic length scales in the gel, and  $\alpha$  is an exponent in the range of 0.7 to 2. These functions are introduced in order to describe additional fluctuations and/or solid-like inhomogeneities. Eq.(reflexp) is an extended form of the Guinier equation ( $\alpha = 2$ ), where non-interacting domains of higher or lower monomer densities are assumed to be randomly distributed in the network. In this case, the distribution is Gaussian and results from the built-in inhomogeneity due to crosslinking formation. The Guinier function is usually written as

$$I(Q) = I(0)\exp(-R_g^2 Q^2/3) \quad (1.25)$$

where  $R_g = 3^{1/2}\Xi$  is the radius of gyration of polymer rich (or poor) domains. Therefore, Eq.(1.20) can be written as:

$$I(Q) = \frac{I_L(0)}{\{1 + \xi^2 Q^2\}} + I_G(0)\exp(-R_g^2 Q^2/3) \quad (1.26)$$

However, the asymptotic behavior predicted by Eq.(1.26),  $I(Q) \propto Q^{-2}$ , does not always hold, and for some gel the scattering function has a higher negative exponent than  $-2$ . Therefore for physically cross-linked gels in water, a scaling form of the scattering function has been proposed (66), by assuming gels composed of closely packed uncorrelated domains of size  $S$  in which the polymer chains are correlated one to each other with the fractal dimension  $D$ . The corresponding scattering function is given by

$$I(Q) = \frac{I_L(0)}{\{1 + [(D+1)/3]\xi^2 Q^2\}^{D/2}} + I_G(0)\exp(-R_g^2 Q^2/3) \quad (1.27)$$

Eq.(1.27) is a generalized Ornstein-Zernike (OZ) equation for a system having the fractal dimension  $D$ . Hence it reduces to the OZ equation when  $D = 2$ , which is the case for linear polymer solutions. Moreover Eq.(1.27) predicts the asymptotic behavior of  $I(Q) \propto Q^{-D}$ , with values of the exponent  $D$  higher than 2 attributed to the presence of hydrogen bonding in the system.

### 1.3 PNIPAM microgels

Most of the responsive-microgels investigated in the last years are based on a thermo-sensitive polymer, the poly(N-isopropylacrilamide), usually known in literature as PNIPAM (or PNIPA, PNIPAAm and PNIPAA), whose chemical formula

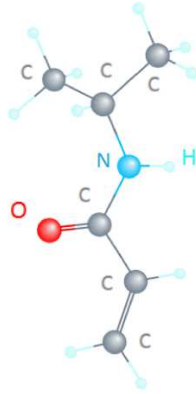


**Figure 1.6:** Schematic picture of the chemical composition of the NIPAM monomer chain.

is  $(C_6H_{11}NO)_n$  (see Fig.1.6). It is known to be soluble in water with a *Lower Critical Solution Temperature* (LCST) (defined as the critical temperature below which two components of a mixture are miscible, thus indicating the critical temperature of solubility) around  $305 - 307$  K, where it undergoes a reversible volume phase transition from a swollen hydrated to a shrunken dehydrated state, losing about 90 % of its volume.

By cross-linking the NIPAM polymer and the N,N'-methyl-bis-acrylamide (BIS) a tridimensional microgel is formed. The main properties of the resulting microgel depends on temperature in the range  $(288 \div 323)K$ , being its properties directly mutuated from the NIPAM polymer. In particular its typical swelling/shrinking transition is the driving mechanism of the phase behavior of PNIPAM microgels dispersed in water, which are thus expected to show a reversible and continuous volume phase transition at temperature around the NIPAM LCST. Indeed the LCST-like behavior of PNIPAM microgels affects the interactions between particles, thus these systems have emerged as potentially useful model soft colloids due to the tunability of both softness and volume as a function of temperature (12, 13, 14, 78). Indeed soft repulsive interactions arising from repulsion between coronas around PNIPAM particles and their deformability confer to PNIPAM microgel suspensions the ability to exhibit a richer phase behavior than hard sphere colloids. The temperature-induced volume phase transition of PNIPAM provides a relatively simple experimental variable, since the effective volume fraction occupied by the microgels in a dispersion can be modulated by changing temperature and driving the system through its VPT.

### 1.3.1 Swelling and Phase Behavior

PNIPAM microgels exhibits a thermo-reversible transition from a swollen to a shrunken state around  $305 - 307\text{K}$ , accompanied by water release. It has been shown that VPT is driven by the coil-to-globule transition of the polymer chains. Indeed at temperature below the LCST, PNIPAM chains are hydrophilic and the polymer-solvent interactions dominate, whilst above the LCST the polymeric chains become hydrophobic and the polymer-polymer interactions are dominant. Thus crossing the LCST the globules collapse and an increasing of both turbidity and viscosity is observed. Indeed, at variance with conventional colloidal particles, such as silica and polystyrene, the PNIPAM microgel spheres in the swollen phase contain up to 97 wt% of water. Consequently, the density and the refractive index of the particles closely match those of water at temperature below the VPT, whilst their differences rapidly increase as the microgel particles expel their water content upon crossing the LCST.

PNIPAM phase behavior has been intensively investigated by using different techniques, such as DLS, UV-visible transmission spectroscopy, rheometry and so on (23, 25, 32, 79). These works have shown that since the particle size decreases with increasing temperature, the volume fraction can be changed by varying the temperature of a single colloidal dispersion, thus exhibiting phase transition at both high and low temperature and leading to a novel phase behavior.

PNIPAM dispersion exists as a clear liquid at low polymer concentration where the absence of spatial constraints allows particle to freely diffuse, thus leading to a liquid-like behavior both below and above the VPT. At higher concentrations the phase behavior of such colloidal suspension resembles that for hard spheres below the VPT temperature (VPTT), where the microgel spheres are fully swollen and the van der Waals attractive interactions are attenuated by the presence of the solvent inside and outside each particle. In particular a FCC-crystal transition is observed by decreasing temperature below 298 K (freezing temperature), where PNIPAM particles self-assembly into a crystalline phase, leading to an iridescent pattern due to Bragg diffraction (24). Above 298 K the iridescent grains completely disappear, the dispersion becomes a homogeneous liquid with small turbidity and the Bragg peak in the crystalline phase progressively disappears by increasing temperature.

By further increasing concentration a cage between neighboring particles gradually forms and limits their motion. Nevertheless in this regime of moderate concentration, the particles are still independent. Therefore in this case neither interpenetration nor compression occur and the system undergoes a transition to a glass state where the microgel particles exhibit repulsion due to their charge or to steric stabilization. Above the VPT van der Waals attractions become dominant originating a fluid-fluid arrested phase separation (25, 79). At temperature well below the VPT ( $T \approx 290\text{ K}$ ), the fluid structure can be well described by a

Hertzian potential (13, 14). Indeed different models have been recently proposed for describing the interaction of uncharged and densely cross-linked microgel in the swollen state in the fluid regime. It has been shown that in this limit, i.e. almost to close packing, the microgel size  $\sigma$  and thus the interparticle potential are independent on concentration. Therefore a Hertzian potential can describe their interaction in the entire fluid regime below freezing, i.e. for  $\phi_{eff} < \phi_{freezing}$  (14). In this case the interactions between spheres are well described by a potential in the form:

$$U_{Hertz}(r) = \begin{cases} \epsilon_H(1 - r/\sigma)^{5/2} & r \leq \sigma \\ 0 & r \geq \sigma \end{cases} \quad (1.28)$$

where  $\epsilon_H$  is the repulsive strength of the potential. A good agreement between the pair correlation functions as obtained from theory and simulations through a Hertzian interaction potential, and the experimental  $g(r)$ , has been evidenced by P.S.Mohanty and coworkers (14), as shown in Fig.1.7. At the lowest investigated effective packing fraction,  $\phi_{eff}$ , the typical features of weakly correlated liquids are exhibited: a weak first peak appears in the  $g(r)$  and the asymptotic values is reached at higher  $r$ . By increasing  $\phi_{eff}$  the height of the first peak increases and higher order peaks appear, indicating an increase in the spatial correlation among the particles.

At even higher concentration, the interpenetration of the outer and less-linked regions of the PNIPAM microgels occurs as well as soft particles compression, leading to a deviation from the spherical shape and to a favorite direction of interaction between particles. At this point the cage structure is destroyed and the system finally percolates, yielding the gel transition, as shown in Fig.1.8 (23).

Despite these findings, the phase diagram is far from being completely clear and in particular the understanding of the phase behavior at high temperature and concentrations is still lacking, despite the evidences of formation of an attractive glass (23). Indeed until now the exact nature of the interaction potential to describe the behavior of microgel particles and therefore the role of repulsive interactions and the origin of attractive ones, such as the real nature (gel or attractive glass) of the state at high concentration, are still ambiguous. In this framework a number of theoretical and experimental studies on PNIPAM microgel dispersion have been recently provided and a great variety of interaction pair potentials, beside the Hertzian one, have been proposed to model the soft colloids in the swollen state (13, 14). In particular other models with a dependence on the outer diameter of the microgel particles, have been introduced, such as an inverse power law pair potential :

$$U_n(r) = \epsilon_n(\sigma/r)^n \quad (1.29)$$

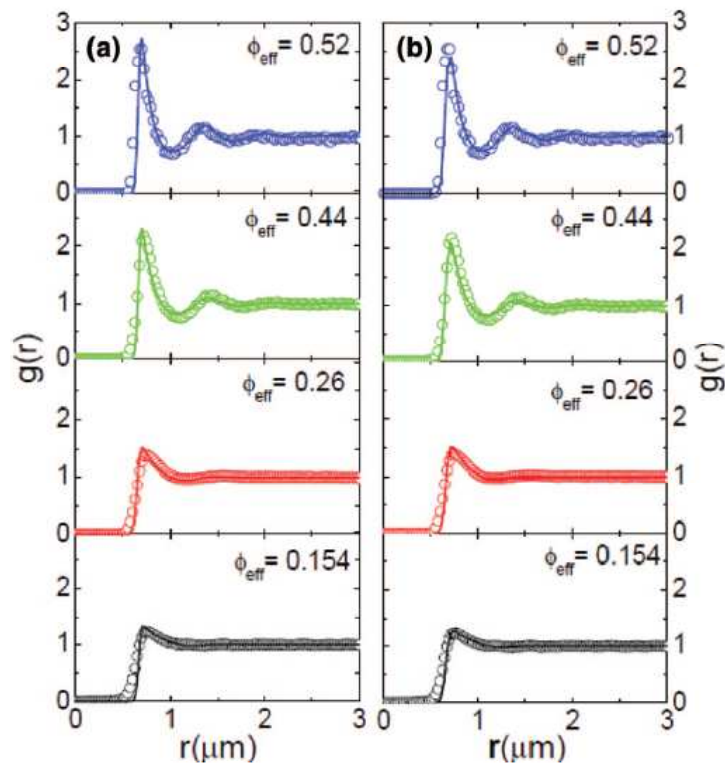


**Figure 1.7:** Comparison between experimental pair-correlation functions  $g(r)$  (open circles) as obtained through confocal laser scanning microscopy and  $g(r)$  obtained from (a) theory and (b) simulation (lines) at different  $\phi_{eff}$  and at  $T = 288K$ , as reported in (14).

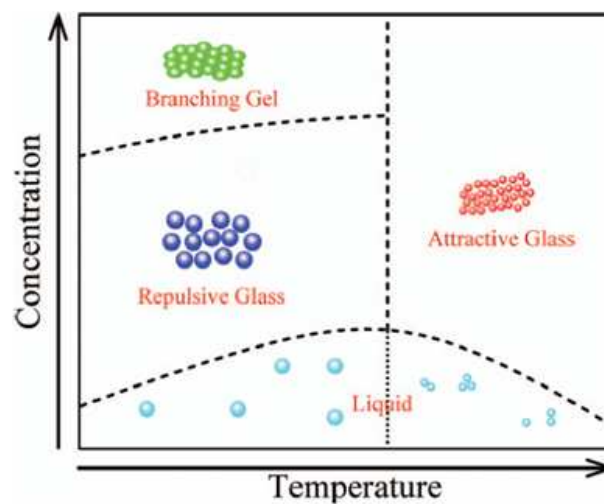


**Figure 1.8:** Phase diagram of PNIPAM microgel suspensions as a function of temperature and concentration, as reported in (23)

where  $\epsilon_n$  is associated to the interaction strength and  $n$  is the power-law exponent describing the potential softness, or a Harmonic potential with a spring constant  $2\epsilon_{harm}$  (80), defined as:

$$U_{harm}(r) = \begin{cases} \epsilon_{harm}(1 - r/\sigma)^2, & r \leq \sigma \\ 0, & r \geq \sigma \end{cases} \quad (1.30)$$

which well captures the behavior of the experimental  $g(r)$  in the investigated fluid region, especially if a more sophisticated model for a two levels description, is used (81, 82). Moreover it has been shown that a high-degree of cross-linking makes the core stiff and incompressible, therefore in the swollen state the mass is concentrated in an incompressible inner-core of size  $R_b$ , whereas all the dynamical features are governed by the effective size  $R = R_b + L_0$  due to the presence of a polymer brush-like corona decorating the dense core, whose thickness  $L_0$  allows to tune the softness of the potential. The result is a harmonic potential, whose spring constant depends on the microgel concentration, whilst the soft corona layer can be modeled through the Alexander-De Gennes scaling. By using this model the physics of the interparticle interactions and the elastic properties of these kind of systems are well predicted. Nevertheless the intrinsic softness in the fully swollen state leads to a concentration dependence of the particle size, and thus of the volume fraction, which makes hard to experimentally reproduce these findings. In particular some failures especially at very high concentrations, impose further investigations.

### 1.3.1.1 Agents affecting the swelling behavior

The swelling capability of the PNIPAM microgel can be tuned both by slightly changing the synthesis procedure and by introducing different additives ranging from salts, non-electrolytes, hydrotropes and surfactants (83).

For example PNIPAM forms mixed hydrophobic aggregates with surfactants, especially in case of anionic ones, such as *Sodium Dodecyl Sulfate* (SDS). The electrostatic repulsion between the charged polymer-bound aggregates contrasts the polymer coil collapse at high temperatures, thus leading to a remarkable increase of the LCST, whilst no changes are observed for cationic or non-ionic surfactants. In addition PNIPAM microgels can be prepared by employing positively charged free radical initiators, thus obtaining microgels with covalently bonded cationic initiator fragments (16) or by adding several inorganic salts such as  $NaI$ ,  $NaBr$ ,  $NaCl$ ,  $NaF$ ,  $Na_2SO_4$  and  $Na_3PO_4$  for investigating their effect on the cloud point (defined as the temperature where the mixture starts to phase separate, thus becoming cloudy) (83). Indeed the electrolytes are known to increase or decrease the LCST of the polymer solutions, thus affecting the phase behavior of uncharged polymers due to the destruction of the hydration structure surrounding

the dissolved polymer chains.

Particular attention has to be paid to the role played by cross-linkers, such as N,N'-(methylene bisacrylamide) (BIS), employed during the synthesis of the microgel particles. Indeed their use is required to prevent the gel from dissolving in water, but taking into account how the swelling capability of the system can be affected by the presence of cross-links is crucial. Indeed it has been shown (30) that the swelling capability decreases with increasing BIS concentration, due to the topological constraints introduced within the PNIPAM microgel particles. Therefore the elastic response of the system can be deeply controlled by changing the cross-linker concentration, leading to microgel particles characterized by a different degree of softness, defined in term of their elastic response to changes of the external parameters.

Moreover introduction of charged monomers, such as acrylic acid (AAc), methacrylic acid (MAAc) or similar (30, 84), has an influence on the swelling of the microgels, due to local electrostatic repulsion. The effective charge density can be controlled by the amount of comonomer, the pH or the ionic strength of the medium. In particular it has been shown (30, 32) that the reduction of the swelling capability of PNIPAM microgel deeply depends on the AAc concentration. In this context the synthesis procedure plays a crucial role, being the response of the PNIPAM/AAc microgels strictly related to the mutual interference between the two monomers, as we will better explain in the next section. Indeed for randomly copolymerized PNIPAM/PAAc microgels, the volume phase transition temperature is observed to increase with PAAc concentration, whilst by interpenetrating the hydrophilic PAAc into the PNIPAM microgels network a little influence on the globule-to-coil transition of the PNIPAM chains is observed (28).

Besides the synthesis procedure, the solvent may affect the dynamics of the system. PNIPAM linear polymers and microgels display interesting phase behavior, called "cononsolvency" in water-acetic acid or water-alcohol mixtures (83, 85). Indeed the response of polymer microgels in water-miscible solvents is believed to be important for understanding the role played by hydrophobicity and hydrogen bonding in the polymer-solvent interactions in the dynamics of polymer solutions. In this framework it is interesting to discuss the Deuterium isotope effects on the swelling kinetics and volume phase transition of polymer microgels. The slower swelling kinetics of microgels in  $D_2O$  than in  $H_2O$  have been shown to be mainly due to the high viscosity of the medium (86). Therefore the LCST of PNIPAM microgels dispersed in  $D_2O$  solutions are expected to be slightly shifted forward with respect to the  $H_2O$  solutions.

Therefore a deeply understanding of the influence of each of these factors on the swelling behavior is crucial to obtain a colloidal system with the required properties, thus ensuring a careful control of the phase behavior.

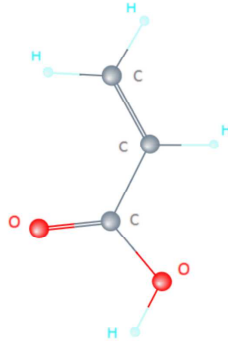


**Figure 1.9:** Schematic picture of the chemical composition of the AAc monomer chain.

## 1.4 IPN microgels of PNIPAM and PAAc

The addition to the PNIPAM network of a pH-sensitive polymer such as the Poly(Acrylic Acid), usually known as PAA or PAAc, whose chemical formula is  $(C_3H_4O_2)_n$  (see Fig.1.9), introduces an additional sensitivity to the pH. In particular in an Interpenetrated Polymer Network (IPN) microgel, typically two or more polymer networks are interpenetrated, leading to a resulting system with an independent responsiveness to those parameters to which the involved homopolymeric network are sensitive. Indeed, whilst by random copolymerization of two monomers a single network of both monomer is obtained, such as in the PNIPAM-co-AAc microgels (30, 31, 32, 87, 88, 89, 90, 91), conversely through polymer interpenetration, such as in the case of the IPN PNIPAM-PAAc microgel (26, 27, 29, 33, 92, 93) investigated in this work, the resulting microgel is made of two interpenetrated homopolymeric networks. Therefore whilst the former exhibits properties dependent on the monomer ratio (30), the latter exhibits the same independent response as the two components to temperature and pH, since their interpenetration leads to a mutual interference between the polymer networks largely reduced (33).

Both the PNIPAM and IPN particles are usually prepared by precipitation polymerization in aqueous media (27, 28, 29). Basically as the PNIPAM particles have been synthesized, the second step of the IPN formation starts with the polymerization of acrylic acid within each PNIPAM nanoparticle. Indeed the interaction between the acrylic acid and the PNIPAM chains, through H-bonds, is stronger within each individual PNIPAM nanoparticle where a higher density of isopropyl (CONH-) groups of PNIPAM is found. Therefore polymerization of AAc primarily occurs within each single nanoparticle and, with further proceeding of the reaction, every single particle acts as a skeleton for the polymerization of acrylic acid. Later reaction mainly takes place on the IPN-forming particle surface, where a greater number of unreacted AAc monomers is available, thus leading to the fast growing of the particle size. The nanoparticles therefore undergo a struc-



tural transition from PNIPAM to IPN microgels, which will be characterized by a highly dense core of interpenetrated PNIPAM and PAAc networks, surrounded by a low density shell mainly populated by PAAc chains.

By following this synthesis procedure the main features of PNIPAM microgel are preserved and the resulting IPN exhibits the same temperature dependence of the VPT with respect to the case of pure PNIPAM microgel, with a transition temperature increased as the acrylic acid concentration increases. Nevertheless the pH-sensitivity of the acrylic acid, due its different solubility at acidic and neutral pH, introduces in the system an additional pH and ionic strength tunability, which gives rise to a more complex phase behavior, since they affect the pair interaction between colloidal particles. Indeed at acidic pH the PAAc chains are not effectively solvated by water and the formation of H-bonds between the carboxylic (COOH-) groups of PAAc and the isopropyl (CONH-) groups of PNIPAM is favored (94). At neutral pH instead the acrylic-acid is soluble in water, thus forming H-bonds with water molecules. Both compounds are therefore solvated by water, that mediates their interaction, and the lower number of interchain H-bonds between PAAc and PNIPAM, makes the two network completely independent one to each other. The temperature and pH-tunability of the swelling properties of this class of microgels have attracted great interest due to the delicate balance between repulsive and attractive interaction which allows the system to exist as a liquid, a colloidal crystal or a disordered state by changing temperature, pH and concentration (12, 32).

### 1.4.1 Swelling and Phase Behavior

For highly diluted IPN microgel suspensions the interaction between particles can be neglected and the particle size variation with temperature has been widely investigated through DLS measurements (27, 28, 30). As shown in Fig.1.10, IPN microgel exhibits the same LCST around  $305 - 307K$  as pure PNIPAM microgels. Despite of this the swelling capability of the IPN microgel is reduced with respect to the pure PNIPAM, due to presence within IPN microgel particles of the hydrophilic PAAc chains which hinders further shrinking of PNIPAM skeleton. Moreover the additional pH sensitivity due to the interpenetration of PAAc, leads to different response of the IPN microgels at different pH values (27). The sharp decrease of the hydrodynamic radius,  $R_h$ , observed at pH below 5 has to be attributed to the strong hydrophobicity of the IPN at acidic pH. Indeed it is well known that at this pH the acrylic acid is mainly in ionic state and forms H-bonds with the PNIPAM chains, rather than with water molecules, thus extruding water from its interior and resulting in a sharp decrease of the particle size. If the pH is increased above 5, the carboxylic groups of the PAAc chains become deprotonated, leading to a strong charge repulsion force which limits the hydrogen-bonding capability of the microgel. Moreover in the range of pH between 5 and 10 an almost constant size of the IPN particles is found, since PNIPAM is pH-insensitive in this range.

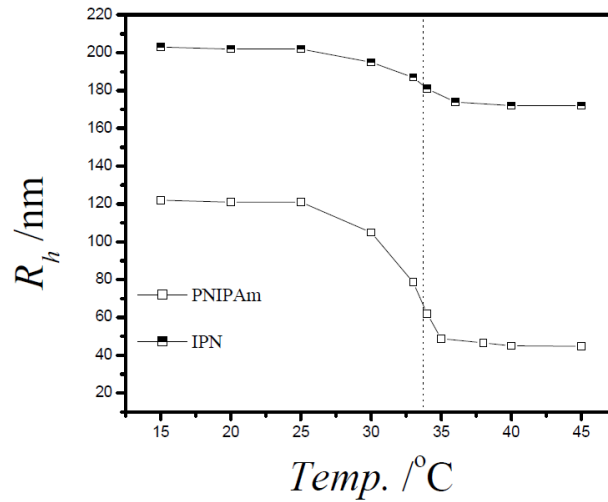


**Figure 1.10:** Hydrodynamics radius for PNIPAm and IPN microgel as reported by Xia et al. (27). In both the cases a volume phase transition is exhibited at the same phase transition temperature, even being the swelling capability reduced for the IPN microgels.

By combining visual inspection, turbidity and viscosity measurements it has been shown (27, 32) that at low polymer concentrations the IPN dispersions undergo a transition from a translucent and easily flowing state, at temperature below the LCST, where the IPN microgels particles are fully swollen, to a shrunken state as temperature increases above the VPT. Nevertheless also at these low concentrations the formation of small aggregates without flocculation is observed, thus suggesting the presence of an attractive interparticle potential.

By increasing concentration it has been shown (32) that the system evolves from a diffusive liquid to a subdiffusive one, characterized by a stretched exponential behavior of the intensity autocorrelation functions, which arises from the cage effect due to close proximity of neighboring particles.

By further increasing concentration a transition to a FCC crystal is observed also at temperature far above the intrinsic LCST, in contrast to pure PNIPAM crystals. Indeed at room temperature it is found as a colloidal crystal, with iridescent patterns due to Bragg diffraction, as a result of the delicate balance between soft repulsive interactions and short-range weak attractions. In particular the soft repulsive interactions presumably arise from the solvation repulsion between solvated PNIPAM-PAAC coronas around the particles, from the compression and/or interpenetration of PNIPAM-PAAC coronas, and from the deformation of microgels upon close contact. Short-range attractive interactions instead have been shown to have three sources: van der Waals attractions, hydrogen bonding between protonated carboxylic groups of PAAC and the surfaces of neighboring microgels and hydrophobic interactions between isopropyl groups of PNIPAM and/or the main

chain of PNIPAM-PAAc coronas. Therefore one can conclude that at high concentration interactions are dominated by attractive short-range interactions, such as hydrophobic interactions and H-bonding. However the presence of soft repulsive interactions makes the initial attractive potential very close to the thermal energy  $k_B T$ , as evidenced by the lack of extensive aggregation between microgel particles. As the particles approach close contact, this attractive potential arising from short-range H-bonding yields to their aggregation, whilst thermal fluctuations lead to the continuously dissociation of these aggregates, thus permitting crystallization as opposed to frustrating it. This would explain the thermostability of the colloidal crystals and the observed increase of their melting point to temperature much higher than the intrinsic LCST, as a result of the stabilization of the assemblies against melting due to the strong attractive interaction potential between particles.

Moreover as the pH is increased above 5, the crystal region of the phase diagram collapses and the dispersion undergoes a transition from an ergodic fluid to a glassy state, which requires further investigation. In addition, at very high polymer concentrations the system exists in a glassy state with a drastic increase of the viscosity above the VPT. The formation of this motionless disordered state can be explained in terms of the frustration of the diffusion of the attractive spheres due to the high viscosity of the suspension which makes the global minimum of the free energy inaccessible.

Even if many aspects of the IPN microgel behavior have been clarified, a systematic investigation of its phase behavior as a function of temperature, pH and concentration, such as a complete theoretical paradigm, are still poorly provided. Moreover the IPN microgel intra-particle response to changes in the external parameters has not been deeply investigated, in particular at high temperatures and/or concentrations. Thus the role played in this region by the additional topological constraints and by H-bonding, when the PAAc is introduced into the PNIPAM network, is still poorly understood. Therefore further theoretical and experimental investigation are required to obtain details on how the PAAc affects both the swelling/shrinking behavior and the transition to a non-ergodic state in a wide range of temperature, pH and concentration.

# Chapter 2

## Experimental Section

The temperature, pH and concentration behavior of a colloidal suspension of microgel particles has been investigated through two different techniques: Dynamic Light Scattering (DLS) and Small-Angle Neutron Scattering (SANS), to probe the dynamics in the  $\mu\text{s}$  time scale and the local structure in the  $nm$  length scale, respectively. In this chapter the basic theory of light and neutron scattering and the information accessible through these two techniques, will be discussed. Finally the sample procedure preparation will be described.

### 2.1 Light Scattering

Light Scattering is one of the experimental techniques broadly used to investigate dynamics and structure of soft materials. Indeed when coherent light impinges on a scattering medium with characteristic distances or dimensions of the same order of its wavelength, a diffraction figure of speckles is observed, with regions of minimum and maximum intensity, due to the constructive or destructive interference between different scattered light beams. The phase of the scattered radiation changes due to changes of the particle's position,  $R_j(t)$ , during its Brownian motion, thus leading to random fluctuations in time of the diffraction figure. Therefore the scattered intensity,  $I_s(\mathbf{Q}, t)$ , embodies information on the particles motion and on their density fluctuations, hence giving details about their spatial configuration, dynamics and relaxations. Light scattering experiments can be divided into two big classes: static experiments, giving measurements of the spatial (or wavevector) dependence of the scattering intensity, and dynamic measurements, giving information about the time-dependence of the fluctuations of the scattered radiation. In particular, the latter includes inelastic (such as Brillouin or Raman scattering), and *quasi-elastic* scattering experiments (such as Rayleigh scattering and Dynamic Light Scattering (DLS)). In this work the DLS technique, also known as photocorrelation spectroscopy, has been exploited to probe the relaxation times

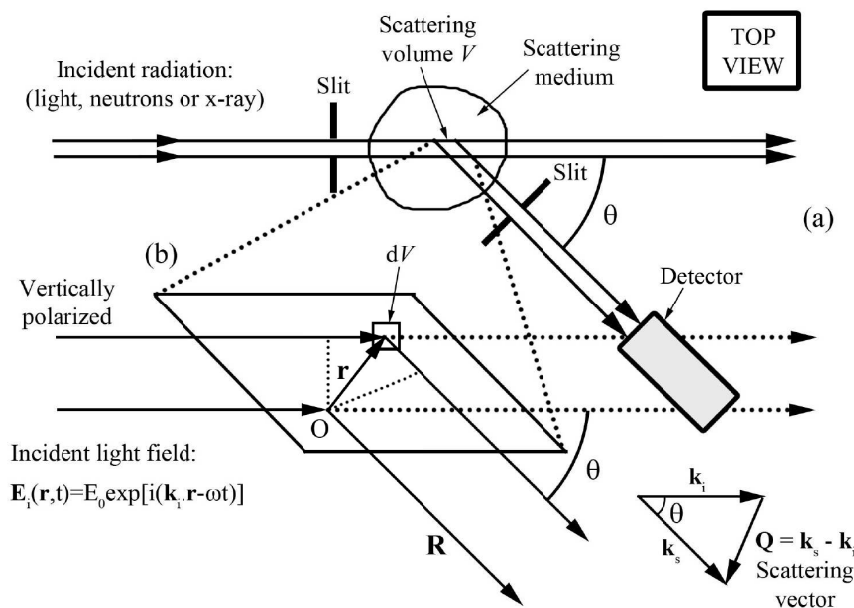


**Figure 2.1:** (a) Top view of a typical scattering experiment. (b) Expanded view of the scattering volume, showing rays scattered at the origin  $O$  and by a volume element  $dV$  at position  $\mathbf{r}$ .

of the system.

As in any scattering technique, DLS measurements are performed as a function of the scattering angle  $\theta$ , which defines the exchanged wave-vector or scattering vector,  $Q$  through the relation ( $Q \approx 2k_i \sin(\theta/2)$ ), where  $k_i$  is the wavevector of the incident wave, in the elastic approximation. The  $Q$  range accessible is between  $10^{-4}$  and  $10^{-2} \text{ nm}^{-1}$ , typical of the light wavelength. As a result, this technique, at odds with neutron and X-ray scattering, suitable for studying the dynamics of simple molecular liquids, is very efficient for studying colloidal systems.

### 2.1.1 Basic Theory of Light Scattering

The great advantage of the electromagnetic radiation as a probe of both the structure and the dynamics of condensed matter, is the access to information about size, shape, and molecular interactions of the scattering particles through the analysis of frequency shifts, angular distribution, polarization and intensity of the scattered radiation. Indeed with the aid of the electrodynamics and the theory of the time-dependent statistical mechanics one can extract structural and dynamical information from the scattered radiation, since its coupling with the system is usually weak enough to apply the linear response theory.

A sketch of a typical scattering experiment is shown in Fig.2.1. In the case of light scattering the monochromatic beam of laser light, with the electric field

component at position  $\mathbf{r}$  and time  $t$  given by  $E_i(\mathbf{r}, t)$ , goes through a polarizer which defines its polarization and then, after impinging on the sample, is scattered. A detector, placed at a scattering angle  $\theta$  with respect to the direction of the incident beam, measures the scattering intensity ( $I_s(\mathbf{Q}, t)$ ). The intersection between the incident and the scattered beam defines the *scattering volume*,  $V$ , whose dimension can be typically controlled by the optics (lenses, pinholes, slits, walls of the sample's container, etc.)

According to the theory reported in Ref.(95), the incident light can be considered as a monochromatic plane-wave, well described by:

$$E_i(\mathbf{r}, t) = p_i E_0 e^{i(\mathbf{k}_i \cdot \mathbf{r} - \omega_i t)} \quad (2.1)$$

where  $p_i$  is the polarization,  $E_0$  is the amplitude,  $\mathbf{k}_i$  is the propagation vector, and  $\omega_i$  is the angular frequency of the incident electric field. The magnitude of the propagation vector is given by  $|\mathbf{k}_i| = k_i = 2\pi n/\lambda$ , with  $\lambda$  being the wavelength of light and  $n$  the refractive index of the scattering medium. The plane wave impinges on a medium with a local dielectric constant

$$\epsilon_i(\mathbf{r}, t) = \epsilon_0 \mathbf{I} + \delta\epsilon(\mathbf{r}, t) \quad (2.2)$$

where  $\delta\epsilon(\mathbf{r}, t)$  represents the dielectric constant fluctuation tensor at position  $\mathbf{r}$  and time  $t$ ,  $\epsilon_0$  is the average dielectric constant of the medium and  $\mathbf{I}$  is the second-order unit tensor. By assuming that the dielectric behavior of the medium is scalar rather than tensorial and that the scattering of the light through the sample is weak, the following assumptions can be made. First of all most of the photons pass through the sample without deviations and only a few of them are scattered once, whilst the probability of double and higher-order scattering events can be neglected. Moreover the incident beam is not significantly distorted by the medium, hence the first Born approximation or its equivalent in the specific context of light scattering (the so-called Rayleigh-Gans-Debye approximation) can be applied. Since the scattering process is "quasi-elastic" and only very small changes of frequency are implied, the magnitude of the propagation vector  $k_s$  of the scattered light,  $k_s = 2\pi n/\lambda$ , is not changed.

In a particle suspension, as those investigated in this work, we can distinguish between the refractive index of the particles and that of the surrounding fluid, implying that the wavelengths of the light inside the particle and inside the fluid solvent are different. This determines a phase difference between the electric field across the particle and the fluid, equal to  $2\pi[\frac{a}{\lambda_p} - \frac{a}{\lambda_f}]$ , where  $a$  is the radius of the particle and  $\lambda_p$  and  $\lambda_f$  are the wavelengths of the light inside the particle and inside the fluid, respectively. Let's now denote with  $\lambda_0$  the wavelength of the light in vacuum, being  $\lambda_p = \lambda_0/n_p$  and  $\lambda_f = \lambda_0/n_f$ , where  $n_p$  and  $n_f$  are the refractive

index of the particle and the fluid, respectively. We can write the phase difference as  $2\pi[n_p - n_f]\frac{a}{\lambda_0}$ , and Eq.(2.1) can be considered as a good approximation if the phase shift is small enough, i.e. if the condition

$$2\pi[n_p - n_f]\frac{a}{\lambda_0} \ll 1 \quad (2.3)$$

is verified. In the following, we will also assume the direction of the incident field to be the same everywhere in the scattering volume, thus neglecting the refraction of light at the interface fluid/particle, based on Eq.(2.3).

The amplitude  $E_s(\mathbf{R}, t)$  of the electric field of the scattered radiation to a point detector at position  $\mathbf{R}$  in the far field can be calculated by applying the Maxwell's equations to the problem of a plane electromagnetic wave which is propagating in a medium with a local dielectric constant given by Eq.(2.2). Therefore it is given by

$$E_s(\mathbf{R}, t) = \frac{E_0}{4\pi\epsilon_0} \frac{e^{i(k_s R - \omega_i t)}}{R} \int_V e^{i\mathbf{Q} \cdot \mathbf{r}} [\mathbf{p}_s \cdot [\mathbf{k}_s \times (\mathbf{k}_s \times (\delta\epsilon(\mathbf{r}, t) \cdot \mathbf{p}_i))]] d^3\mathbf{r} \quad (2.4)$$

where  $V$  indicates the integral over all the scattering volume,  $\mathbf{p}_s$  is the polarization of the scattered electric field and  $\mathbf{Q}$  is the scattered wave-vector defined as the difference between the scattered and the incident wavevectors ( $\mathbf{Q} = \mathbf{k}_s - \mathbf{k}_i$ ), from the scattering geometry. In particular the quasi-elastic assumption of the scattering process, leads to a wavelength of the incident light almost unchanged, so that  $|\mathbf{k}_i| \sim |\mathbf{k}_s|$ . Thus, the scattering geometry in Fig.2.1 easily affords the magnitude of  $\mathbf{Q}$  from the law of cosines,

$$Q^2 = |\mathbf{k}_s - \mathbf{k}_i|^2 = k_s^2 + k_i^2 - 2\mathbf{k}_i \cdot \mathbf{k}_s = 2k_i^2 - k_i^2 \cos(\theta) = 4k_i^2 \sin^2(\theta/2) \quad (2.5)$$

$$|Q| = 2k_i \sin(\theta/2) = \frac{4\pi n}{\lambda} \sin \theta/2 \quad (2.6)$$

where  $\theta$  is the scattering angle between the directions of the incident and the scattered fields. Thanks to the identity  $a \times (b \times c) = b(a \cdot c) - c(a \cdot b)$ , Eq.(2.4) can be simplified to

$$E_s(\mathbf{R}, t) = -\frac{k_s^2 E_0}{4\pi\epsilon_0} \frac{e^{i(k_s R - \omega_i t)}}{R} \int_V e^{i\mathbf{Q} \cdot \mathbf{r}} \delta\epsilon_{is}(\mathbf{r}, t) d^3\mathbf{r} \quad (2.7)$$

where the component of the dielectric constant fluctuation tensor along the initial

and final polarization directions is defined as

$$\delta\epsilon_{is}(\mathbf{r}, t) \equiv \mathbf{p}_s \cdot \delta\epsilon(\mathbf{r}, t) \cdot \mathbf{p}_i. \quad (2.8)$$

The atoms of any infinitesimal region of volume  $dV \equiv d^3r$  of the total scattering volume, see the same electric incident field, consequently the scattered field is the overlap of the fields scattered by each region. Therefore Eq.(2.7) can be rewritten as the sum of the amplitudes of the infinitesimal fields  $dE_s(\mathbf{R}, t)$  scattered by each elementary volume  $dV$  at position  $\mathbf{r}$ :

$$E_s(\mathbf{R}, t) = \int_V dE_s(\mathbf{R}, t) \quad (2.9)$$

where

$$dE_s(\mathbf{R}, t) = -\frac{k_s^2 E_0}{4\pi\epsilon_0} \frac{e^{i(k_s R - \omega_i t)}}{R} e^{i\mathbf{Q} \cdot \mathbf{r}} \delta\epsilon_{is}(\mathbf{r}, t) d^3\mathbf{r} \quad (2.10)$$

One can notice that Eq.(2.10) is the expression for the radiation due to an oscillating point dipole. Therefore the incident electric field, of intensity  $E_0$  and propagation vector  $\mathbf{k}_s$ , induces in the elementary volume  $dV$  at position  $\mathbf{r}$ , a dipole moment of strength proportional to  $E_0 \delta\epsilon_{is}(\mathbf{r}, t)$  which oscillates at angular frequency  $\omega_i$ , thus radiating, or equivalently scattering, light in all directions. As evidenced by the second factor in Eq.(2.10) the radiation scattered from the origin  $O$  is described by a spherical wave. Moreover the term  $\exp(i\mathbf{Q} \cdot \mathbf{r})$  takes into account the shift in space of the radiation scattered by the volume element at position  $\mathbf{r}$  with respect to that scattered by an element at the origin  $O$ . Therefore Eq.(2.4) embodies all the fundamental physics of light scattering: the scattered electric field is described by a spherical wave radiated from the scattering volume with a  $\mathbf{Q}$ -dependent amplitude which is the spatial Fourier transform of the instantaneous variations in the dielectric constant of the system. Indeed in the case of a totally homogeneous medium,  $\delta\epsilon(\mathbf{r}, t) = 0$ , thus no scattering occurs, suggesting that scattering of radiation (for  $\mathbf{Q} \neq 0$ ) is due to the spatial fluctuations in the dielectric properties of the medium. Usually in a light scattering experiment, the scattered light rather than the electric field is directly measured, but since intensity and fields are related through  $I(\mathbf{Q}, t) = |E(\mathbf{Q}, t)|^2 = E(\mathbf{Q}, t)E^*(\mathbf{Q}, t)$ , one can easily get the expression for the instantaneous scattering intensity for the case of discrete scattering particles suspended in a liquid as

$$I_s(\mathbf{Q}, t) = \frac{E_0^2}{R^2} \sum_{j=1}^N \sum_{k=1}^N b_j(\mathbf{Q}, t) b_k^*(\mathbf{Q}, t) e^{i\mathbf{Q} \cdot [\mathbf{R}_j(t) - \mathbf{R}_k(t)]} \quad (2.11)$$

where  $b_j$  is the "scattering length".



The intensity of the scattering, averaged over time, provides information on the sample's structure, essentially on spatial correlations of the particles. On the other hand, any variation in time of the local dielectric constant is directly reflected in temporal variations of amplitude and intensity of the scattered field. Therefore light scattering directly probes both the structure and the dynamics of a sample in the reciprocal, or  $\mathbf{Q}$ , space.

## Intensity Autocorrelation Functions

Let's consider a scattering medium, such as a suspension of colloidal particles, illuminated by coherent light. At any instant, the far-field pattern of scattered light is constituted by a grainy random diffraction, or "speckle" pattern as shown in Fig.2.2, determined by the phase interference of light scattered by individual particles which yields to interchange of dark or bright regions.

Furthermore, the Brownian motion of the particles determines fluctuations of the speckle pattern from one random configuration to another. Thus, as sketched in Fig.2.2 (b), the scattered intensity  $I_s(\mathbf{Q}, t)$  randomly fluctuates in time. The important structural and dynamical information about position and the orientation of the particles are embodied in these time-dependent fluctuations. The information can be extracted by performing a time average:

$$\langle I_s(\mathbf{Q}, t_0, T) \rangle = \frac{1}{T} \int_{t_0}^{t_0+T} I_s(\mathbf{Q}, t) dt \quad (2.12)$$

where  $t_0$  is the time at which the measurement has begun and  $T$  is the time over which it is averaged. In the ideal experiment the average would be over an infinite time:

$$\langle I_s(\mathbf{Q}, t_0) \rangle = \lim_{T \rightarrow \infty} \frac{1}{T} \int_{t_0}^{t_0+T} I_s(\mathbf{Q}, t) dt \quad (2.13)$$

In practice,  $T$  must be large, compared to the fluctuations period,  $T_c$ . Under general conditions it can be shown that  $\langle I_s(\mathbf{Q}, t_0) \rangle$  is independent of starting time  $t_0$  (95). Moreover, as shown in Fig.2.2(b), the intensity fluctuates around its time average, therefore Eq.(2.13) can be written as

$$\langle I_s \rangle = \lim_{T \rightarrow \infty} \frac{1}{T} \int_0^T I_s(\mathbf{Q}, t) dt \quad (2.14)$$

In general, the intensity of the scattered light at two different instants ( $t$  and  $t+\tau$ ) will be different ( $I_s(\mathbf{Q}, t) \neq I_s(\mathbf{Q}, t+\tau)$ ). Nevertheless when  $\tau$  is very small compared to the times scale of a single fluctuation ( $T_c$ ),  $I_s(\mathbf{Q}, t)$  will be very close to  $I_s(\mathbf{Q}, t+\tau)$ . On the other hand, as  $\tau$  increases, the deviation of  $I_s(\mathbf{Q}, t)$  from

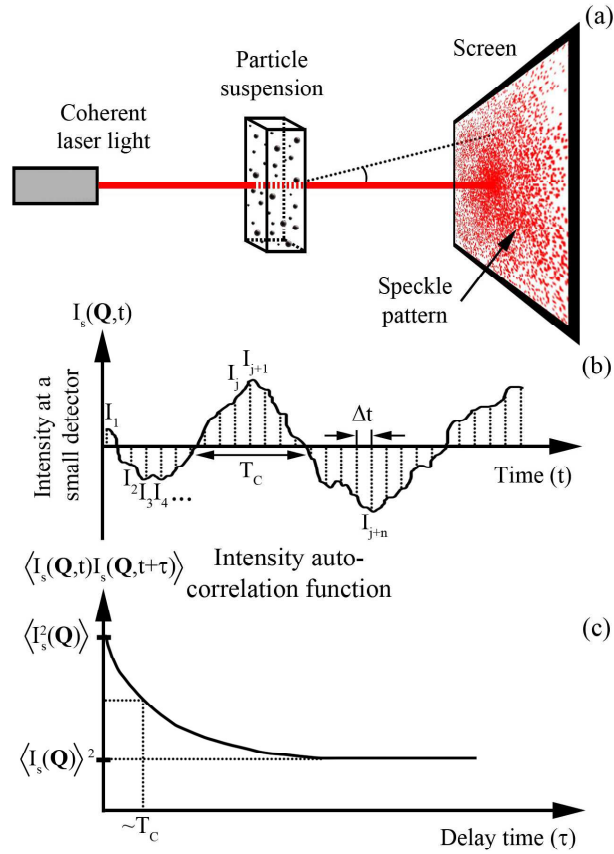


**Figure 2.2:** (a) Coherent (laser) light scattered by a random medium such as a suspension of colloidal particles gives rise to a random diffraction pattern, or speckle, in the far field. (b) Fluctuating intensity observed at a detector with the size of about one speckle. (c) The time-dependent part of the correlation function decays with a time constant  $T_c$  equal to the typical fluctuation time of the scattered light.

$I_s(\mathbf{Q}, t + \tau)$  will be sensibly different from zero. Therefore, the value of  $I_s(\mathbf{Q}, t)$  is correlated with  $I_s(\mathbf{Q}, t + \tau)$  when  $\tau$  is small enough, whilst the correlation is lost as  $\tau$  becomes large compared to the typical fluctuation time of the system. A measure of this correlation is given by the intensity autocorrelation function, defined as

$$\langle I_s(\mathbf{Q}, 0) I_s(\mathbf{Q}, \tau) \rangle = \lim_{T \rightarrow \infty} \frac{1}{T} \int_0^T I_s(\mathbf{Q}, t) I_s(\mathbf{Q}, t + \tau) dt \quad (2.15)$$

Demonstration of how the time-correlation function changes with time is now crucial. Let's start by looking at Eq.(2.15) at zero delay, where it is

$$\lim_{\tau \rightarrow 0} \langle I_s(\mathbf{Q}, 0) I_s(\mathbf{Q}, \tau) \rangle = \langle I_s^2(\mathbf{Q}) \rangle \quad (2.16)$$

For delay times much greater than the typical fluctuation time of the intensity ( $T_C$ ), fluctuations in  $I_s(\mathbf{Q}, t)$  and  $I_s(\mathbf{Q}, t + \tau)$  are uncorrelated, thus the average in Eq.(2.15) can be separated

$$\lim_{\tau \rightarrow \infty} \langle I_s(\mathbf{Q}, 0) I_s(\mathbf{Q}, \tau) \rangle = \langle I_s(\mathbf{Q}) \rangle \langle I_s(\mathbf{Q}, \tau) \rangle = \langle I_s(\mathbf{Q}) \rangle^2 \quad (2.17)$$

If  $I_s$  is a constant of the motion and taking into account that  $\langle I_s^2(\mathbf{Q}) \rangle \geq \langle I_s(\mathbf{Q}) \rangle^2$ , thus the autocorrelation function either remains equal to its initial value for all times  $\tau$ , or it decays from its initial value, which therefore corresponds to its maximum. The scattered intensity  $I_s(\mathbf{Q}, t)$  is a non-conserved and non-periodic property of the system, therefore the intensity correlation function decays from the mean of the squared intensity  $\langle I_s^2(\mathbf{Q}) \rangle$  at small delay times to the square of the mean intensity  $\langle I_s(\mathbf{Q}) \rangle^2$  at long times (Fig.2.2). The characteristic time of this decay is a measure of the typical fluctuation time of the intensity ( $T_c$  in Fig.2.2 (b) and (c)).

We conclude this section by giving the expression for the intensity correlation function in the discrete case, which is usually used to compute the time-correlation functions in light scattering experiments. Let's divide the time axis into discrete intervals  $\Delta t$  as shown in Fig.2.2(b), i.e.  $t = j\Delta t$ ,  $\tau = n\Delta t$ ,  $T = N\Delta t$  and  $t + \tau = (j + n)\Delta t$  and assume that the intensity  $I_s(\mathbf{Q}, t)$  does not change significantly over the time interval  $\Delta t$ . From the definition of integral Eqs.(2.14) and (2.15) can be approximated

$$\langle I_s \rangle \cong \lim_{N \rightarrow \infty} \frac{1}{N} \sum_{j=1}^N I_j \quad (2.18)$$

$$\langle I_s(\mathbf{Q}, 0) I_s(\mathbf{Q}, \tau) \rangle \cong \lim_{N \rightarrow \infty} \frac{1}{N} \sum_{j=1}^N I_j I_{j+n} \quad (2.19)$$

where  $I_j$  is the scattering intensity at the beginning of the  $j^{th}$  interval. Eq.(2.18) and Eq.(2.19) approximate the infinite time averages as  $\Delta t \rightarrow 0$ .

### 2.1.2 Dynamic Light Scattering

In a typical Dynamic Light Scattering experiment the incident radiation beam is diffused by the scattering sample and then analyzed by a photomultiplier. Therefore it is possible to obtain information about the system from the variation of the scattered intensity, quantitatively formalized in the autocorrelation function of the scattered intensity. Nevertheless by choosing the opportune DLS setup it is possible to directly obtain information from different signals. In particular the normalized autocorrelation function of the scattered field  $g^{(1)}(\mathbf{Q}, \tau)$  can be directly measured by using a heterodyne setup, whilst the homodyne setup, as used in this work, gives access to the time correlation function of the scattered intensity  $I_s(\mathbf{Q}, t) = |E_s(\mathbf{Q}, t)|^2$ . Therefore heterodyne and homodyne techniques yield different information on the system dynamics, although intrinsically related one with the other as described in the following.

In the homodyne setup only the scattered light impinges on the detector and the normalized autocorrelation function of the intensity defined as

$$g^{(2)}(\mathbf{Q}, \tau) = \frac{\langle I_s(\mathbf{Q}, 0) I_s(\mathbf{Q}, \tau) \rangle}{\langle I_s(\mathbf{Q}, 0) \rangle^2} \quad (2.20)$$

is measured.

Otherwise, in the heterodyne setup a small portion of the incident beam (called local oscillator) is mixed with the scattered light and the detector surface is wet by the sum of these two interfering fields  $E_{LO}(t) + E_s(\mathbf{Q}, t)$ , where  $E_{LO}(t)$  stands for the  $\mathbf{Q}$ -independent local oscillator. The time correlation function of the collected intensity  $I_{he}(\mathbf{Q}, t) = |E_{LO}(t) + E_s(\mathbf{Q}, t)|^2$  is therefore recorded. In this case the normalized time correlation function of the scattered field defined as

$$g^{(1)}(\mathbf{Q}, \tau) = \frac{\langle E_s(\mathbf{Q}, 0) E_s^*(\mathbf{Q}, \tau) \rangle}{\langle E_s(\mathbf{Q}, 0) \rangle^2} \quad (2.21)$$

can be directly measured.

For a system of identical particles one can derive the "Siegert relation"

$$g^{(2)}(\mathbf{Q}, \tau) = 1 + [g^{(1)}(\mathbf{Q}, \tau)]^2 \quad (2.22)$$

which reflects the factorization properties of the correlation functions of a complex Gaussian variable.

It can be shown that the above equation is valid even if the hypotheses of Gaussian distribution of the diffuse field  $E_s(\mathbf{Q}, t)$  is not verified, due to a non ideal incident beam or to non-independent scattered fields.

In a DLS experiment, the intermediate scattering function  $F(\mathbf{Q}, \tau)$ , or equivalently  $g^{(1)}(\mathbf{Q}, \tau)$ , is usually the interesting quantity and it can be obtained directly from the intensity correlation function  $g^{(2)}(\mathbf{Q}, \tau)$  by inverting Eq.(2.22):

$$F(\mathbf{Q}, \tau) = g^{(1)}(\mathbf{Q}, \tau) = \sqrt{g^{(2)}(\mathbf{Q}, \tau) - 1} \quad (2.23)$$

The results obtained in this section correspond to the limit of "far field", since they have been derived considering the amplitude of the electric field scattered to a point in the field far enough from a point given as the origin (Eq.(2.7)). Nevertheless, a detector has a non-zero active area and therefore on its surfaces it sees different scattered fields at different points. Then it can be shown that in real experiments Eq. (2.22) needs to be modified to

$$g^{(2)}(\mathbf{Q}, \tau) = 1 + B[g^{(1)}(\mathbf{Q}, \tau)]^2 \quad (2.24)$$

where  $B$  is a factor which represents the degree of spatial coherence of the scattered light over the detector and is determined by the ratio of the detector area to the area of one speckle. When this ratio is much smaller than 1, as is the case of a "point detector",  $B \rightarrow 1$ . On the contrary when the detector is detecting many independently fluctuating speckles, thus  $B \rightarrow 0$ . Essentially the detector aperture is usually chosen in order to accept about one speckle, hence giving  $B \approx 0.8$ . By inverting Eq.(2.24) one can obtain the relation

$$B^{1/2}F(\mathbf{Q}, \tau) = \sqrt{g^{(2)}(\mathbf{Q}, \tau) - 1} \quad (2.25)$$

which helps in obtaining the setup dependent coherence factor  $B$  by fitting the time correlation functions. This parameter is useful for the alignment of the experimental apparatus and once the setup is aligned it remains unchanged.

In the most general case of particles with anisotropic shape, the anisotropic polarizability tensor has eigenvectors correspondent to the directions perpendicular and parallel to the symmetry axis. Therefore, for a vertically polarized incident field, the vertical and horizontal scattering components give information about the translational and rotational degrees of freedom. On the contrary by dealing with optically isotropic samples, the averaged quantities, such as  $g^{(1)}(Q, \tau)$  and  $g^{(2)}(Q, \tau)$ , only depend on the modulus of the scattering vector ( $|\mathbf{Q}|$ ). Thus for particles with spherical symmetry the parallel and perpendicular polarizabilities are equal, hence the intrinsic particle anisotropy vanishes and only the polarized signal is relevant.

Therefore, for a dilute suspension of identical non-interacting spheres, the autocorrelation function of the scattered field, given by Eq.(2.21), has only the contribution of the polarized component of the electric field, thus by defining the displacement of the particle in time as

$$\Delta \mathbf{R}(\tau) = \mathbf{R}(\tau) - \mathbf{R}(0) \quad (2.26)$$

it can be written as:

$$g^{(1)}(\mathbf{Q}, \tau) = \langle e^{i\mathbf{Q} \cdot \Delta \mathbf{R}(\tau)} \rangle \quad (2.27)$$

which means that DLS provides information on the average translational motion of a single particle. The displacement of a particle in Brownian motion is a (real) three-dimensional random variable with a Gaussian probability distribution

$$P[\Delta R(\tau)] = \left[ \frac{3}{2\pi \langle \Delta R^2 \rangle} \right]^{\frac{3}{2}} \exp \left[ -\frac{3\Delta R^2(\tau)}{2 \langle \Delta R^2(\tau) \rangle} \right] \quad (2.28)$$

where the particle's mean square displacement in time is

$$\langle \Delta \mathbf{R}^2(\tau) \rangle = 6D_t\tau \quad (2.29)$$

The free-particle translational diffusion coefficient is given by the well known Stokes-Einstein relation

$$D_t = \frac{k_B T}{6\pi\eta r} \quad (2.30)$$

where  $k_B$  is the Boltzmann's constant,  $T$  is the temperature,  $\eta$  the shear viscosity of the suspension medium, and  $r$  the particles radius. Evaluation of the average in Eq.(2.27) over the Gaussian probability distribution (Eq.(2.28)) gives the autocorrelation function of the scattered field

$$g^{(1)}(\mathbf{Q}, \tau) = \exp \left[ -\frac{Q^2}{6} \langle \Delta R^2(\tau) \rangle \right] = e^{-Q^2 D_t \tau} \quad (2.31)$$

In this simple case the autocorrelation function behaves as a single exponential decay. The normalized intensity correlation function on the other hand can be calculated by using the Siegert expression of Eq.(2.24), and it takes the form

$$g^{(2)}(\mathbf{Q}, \tau) = 1 + B[e^{D_t Q^2 \tau}]^2 \quad (2.32)$$

In the case of Brownian motion the translational diffusion coefficient  $D_t$  can be related to the relaxation time of the system through the relation  $\tau_r = 1/(Q^2 D_t)$ , giving a measure of the decay with time of the correlation between the particle positions, due to the Brownian diffusion.

Therefore Eq.(2.32) can be rewritten in term of the relaxation time as

$$g^{(2)}(\mathbf{Q}, \tau) = 1 + B[e^{\tau/\tau_r}]^2 \quad (2.33)$$

In the limit of non interacting spherical particles, the hydrodynamic radius can be easily calculated from the relaxation time by inverting Eq.(2.30).

In the case of colloidal systems, the interactions between particles can be neglected only at very low concentrations. In the majority of the samples of interest, instead, this condition is not verified and the intensity correlation functions cannot be described by Eq.(2.33), and the Kohlrausch-Williams-Watts expression (96, 97) is generally used:

$$g_2(Q, \tau) = 1 + B[(e^{-\tau/\tau_r})^\beta]^2 \quad (2.34)$$

where the introduced parameter  $\beta$  is a measure of the deviation from the simple exponential decay ( $\beta = 1$ ). Indeed colloidal systems present a distribution of relaxation times leading to a stretching of the correlation functions, as for any glassy material. This behaviour is usually referred to as "stretched", and is characterized by an exponent  $\beta < 1$ .

### 2.1.3 Multi Angles Dynamic Light Scattering Setup

The setup used for this work is a five angles dynamic scattering setup built and used to acquire DLS measurements, as shown in Fig.2.3 and in Fig.2.4.

A solid state laser with a wavelength of  $\lambda = 642nm$  (red) and a power of  $100mW$  has been used. The laser beam is vertically polarized with a polarization ratio of 500 : 1. In order to control the intensity of the laser impinging on the sample, and consequently the intensity of the scattered light, neutral density filters are placed in front of the laser. These filters have been used in order to choose an incident intensity that provides the best correlation quality, i.e. high coherence factor and low noise. The laser beam is then focused on the sample by a lens ( $L_1$ ) of focal equal to 125mm, to give a minimum beam diameter of approximately  $50\mu m$ . The sample environment is a cylindrical transparent glass cell, called VAT, with 111mm of diameter, filled with distilled water as index matching fluid, in order to reduce the refraction of the scattered light through the walls and stray light scattering.

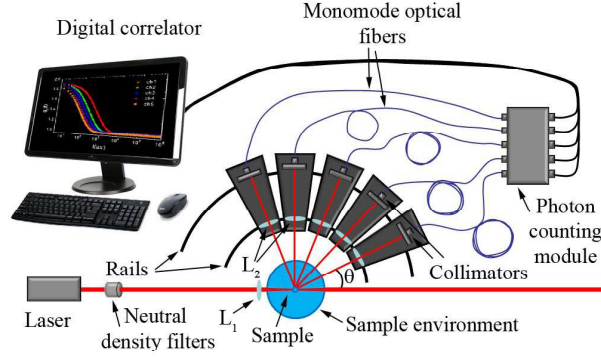


**Figure 2.3:** Sketch of the five angles dynamic light scattering setup. The laser beam of wavelength 642 nm is focused through lens  $L_1$  on the center of the sample. The scattered field is collected through lenses  $L_2$  at five different scattering angles  $\theta$  and then collimated on five monomode optical fibers. The collection/collimation devices can move on circular rails, in such a way that the scattering angles can be chosen before the experiment. Five photomultiplier tubes collect photon-counts that are analyzed by the software correlator to compute time autocorrelation functions.

The sample cuvette with cylindrical shape is placed in the center of the VAT, which is connected to a HAAKE **DC50** thermo-regulator for temperature control. The focal point is at the center of the circular optical geometry defined by the concentric rails used to move the detection lenses  $L_2$  and the collimators coupled by a metallic base. The scattered intensity is collected at five different values of the scattering angle  $\theta$ , which corresponds to five different values of the scattering vector (in the range  $6.2 \times 10^{-4} < Q \text{ (\AA}^{-1}) < 2.1 \times 10^{-3}$ ), according to the relation  $Q = (4\pi n/\lambda) \sin(\theta/2)$ . The values  $\theta_i$  with  $(i = 1, \dots, 5)$  of the scattering angles can be chosen by displacing the bases that are free to move on circular rails centered on the scattering cell. Each base holds the optics and mechanics necessary for the collection of the scattered beam as well as for its collimation on an optical fiber. The minimum angular offset between adjacent collection device is  $20^\circ$ . The scattered light is collected by biconvex lenses ( $L_2$ ) with focus on the illuminated sample volume, so that the scattering volume  $V$  is defined by the intersection of the Gaussian beam profiles determined by the  $L_1$  and  $L_2$ . The scattered light is collimated in the core of each monomode optical fiber that brings the signal to the photomultipliers used in single photon counting mode. The five different values of the scattering angle used in my experiment are  $\theta = 30^\circ, 50^\circ, 70^\circ, 90^\circ, 110^\circ$ , that correspond to five different values of the momentum transfer  $Q$ , according to the relation  $Q = (4\pi n/\lambda) \sin(\theta/2)$ . The number of photons detected by each photomultiplier is transferred to a computer through an input-output digital card from National Instruments<sup>®</sup>, and the time autocorrelation functions are computed using a software correlator developed by Di Leonardo (98).



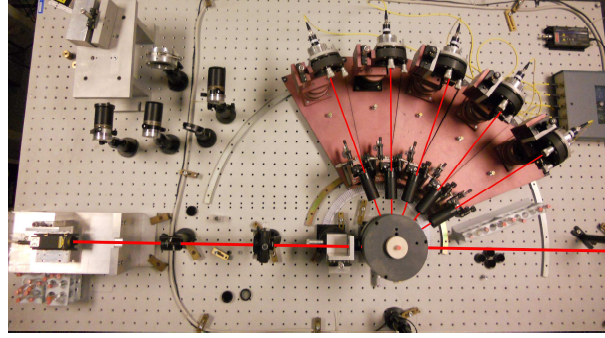


**Figure 2.4:** Top view photograph of the five angles DLS setup. The laser beam and the scattered light are evidenced by red lines drawn only to guide the eyes. All the optical components shown in the schematic Fig.2.3 can be observed in this photograph.

A top view photograph of the five angles DLS setup is shown in Fig.2.4. The laser beam as well as the scattered light at five different  $\theta$  are highlighted by red lines. All the optical components shown in the schematic Fig.2.3 can be evidenced in this photograph. In our set-up no optical polarizer were used, since the depolarized intensity of the laser source is much lower than the polarized one giving no significant contribution to the polarized correlation function, as discussed above. The experimental setup has been calibrated by using a standard sample, i.e. a highly dilute colloidal suspension of microspheres of latex with known diameter  $\phi = 91nm$ , by following the standard DLS data analysis procedure discussed in the previous section.

## 2.2 Neutron Scattering

Neutron beams available for condensed matter studies cover a range of wavelengths between 0.001 – 3 nm, which extends the range covered by light scattering by orders of magnitude. Although X-rays can cover the same range of wavelengths, neutrons have some characteristics that make them particularly suitable for condensed matter investigation (99).

Neutrons are neutral elementary particles with a mass  $m = 1.675 \times 10^{-24}g$  and spin 1/2, kinetic energy  $E$  and momentum  $p$  equal to  $E = \frac{1}{2}mv^2$  and  $p = mv$ , respectively, where  $v$  is the velocity. These features make neutrons useful probes for condensed matter investigation for the following reasons:

1. they have no charge, thus neutrons can deeply penetrate the matter, giving bulk information and allowing measurements in extreme temperature and pressure conditions;
2. their wavelength (for thermal neutrons  $\lambda \approx 1.8 \text{ \AA}$ , as we will see in the following) is comparable with the interatomic distances, allowing structural studies on these length scales;
3. in inelastic scattering experiment, the energies of the thermal neutrons are about  $E_n \approx k_B T_{amb} \approx 25 meV$  and thus of the same order of magnitude of the elementary excitations in solids, yielding information about molecular vibrations and collective motion;
4. at odds with X-rays, neutrons do not interact with the electrons of the atoms via electromagnetic interaction, but with the nuclei, via the strong interaction (100). For this reason they interact also with the H atoms and allow to distinguish isotopes of the same element. Indeed, as shown in Fig.2.5, at variance with the X-rays, for neutrons the scattering length is completely independent on the atomic number  $Z$  of the radiated atom. This characteristics of neutrons is the basis of the isotopic substitution techniques;
5. their spin is a useful tool for studies of magnetic properties.

In general, the important factors for a neutron experiment are the energy and the intensity of the neutrons in the beams and the time structure of the flux, as well as any background radiation, as for instance  $\gamma$ -rays. Indeed the characteristic energy determines the type of structural or dynamical investigation suited to the source, while the time structure of the flux, continuous or pulsed, determines the design of the spectrometer. There are two ways to produce neutrons in sufficient quantities for worthwhile experiments. The most obvious of these is to use a nuclear reactor: neutrons are released by the fission of uranium-235, releasing, for each fission event, 2 - 3 neutrons, though one of these is needed to sustain the

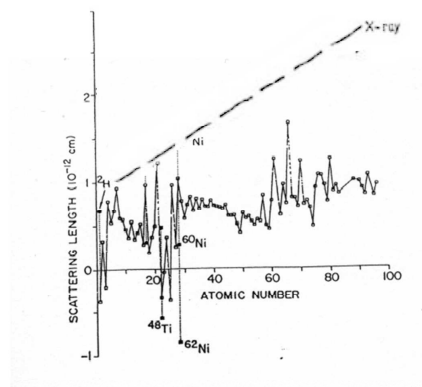


**Figure 2.5:** Scattering Length behavior of X-rays (dot line) and neutrons (full line) as a function of the atomic number of the radiated atom.

chain reaction. Today the most powerful reactor source in the world is the 55 MW HFR (High-Flux Reactor) at the Institute Max Von Laue - Paul Langevin ("ILL") in Grenoble, France. The other approach to neutron production is that used in spallation neutron sources: particle accelerators and synchrotrons are used to generate intense, high-energy, proton beams which are, in turn, directed at a target composed of heavy nuclei. Provided that the protons have sufficient kinetic energy they are able to overcome the intrinsic long-range electrostatic and short-range nuclear forces and effectively blast the target nuclei apart. Presently in Europe there is a spallation source in construction (ESS) and another in operation (ISIS). The ISIS Facility, where the experiments described in the following have been performed, operates nearby Oxford in the United Kingdom. It is based on a 200  $\mu A$ , 800 MeV (i.e., 160 kW), proton synchrotron operating at 50 Hz, and a tantalum target which releases approximately 12 neutrons per incident proton.

Whether produced by a nuclear fission reaction as in a nuclear reactor or by spallation, the emerging neutrons have very high velocity, and therefore they need to be moderated down to energies useful for scattering from condensed matter. This is usually achieved by collisions with a hydrogenous material, called moderator. Moderated neutrons can be considered as a "gas" in equilibrium at the temperature of the moderator, with Maxwell-Boltzmann distribution of velocities, given by

$$f(v) = 4\pi \left( \frac{m}{2\pi k_B T} \right)^{3/2} v^2 e^{-\frac{1}{2}mv^2/k_B T} \quad (2.35)$$

where  $f(v)dv$  is the fraction of gas molecules with velocity between  $v$  and  $v + dv$  and  $k_B$  is the Boltzmann's constant equal to  $1.381 \times 10^{-23} J/K$ , with a maximum of the function  $f(v)$  occurring at  $v = (2k_B T/m)^{1/2}$ . The so-called cold neutrons emerge from a small volume of liquid deuterium maintained at around 25 K, whilst

thermal neutrons are those moderated with heavy water at around  $330\text{ K}$ . A block of hot graphite at  $T \approx 2000\text{ K}$  works as a source of hot neutrons. The flux, that is the number of neutrons of velocity  $v$  emerging from the moderator per second, is proportional to  $v$  times  $f(v)$ .

Several general characteristics can be identified in any spectrometer which uses radiation to investigate organization or motion at molecular level, nevertheless the wide diversity of neutron spectrometers depends crucially on those aspects of structure or motion in the scattering systems which are to be studied. A description of specific neutron scattering techniques should then necessarily be closely associated with a discussion of the scattering systems and model structure factors. Therefore hereafter I will focus the attention on the determination of the microscopic structure of materials, and in particular on Small Angle Neutron Scattering (SANS) experiments.

### 2.2.1 Basic Theory of Neutron Scattering

Neutrons exhibit both classical and quantum behaviors. Indeed on one hand the mean free path  $L$  into the sample is of the order of  $nm$  or  $cm$ , that is much larger than their wavelength  $\lambda$ , making the neutron transport classically treatable. Nevertheless it is not possible to understand the scattering process itself without taking into account that neutrons also exhibit wave-like behavior, with wavelength  $\lambda$  given by the *de Broglie* relation:

$$\lambda = \frac{h}{p} = \frac{h}{mv} \quad (2.36)$$

where  $h$  is the Planck constant.

Therefore when thermal neutrons, with wavelength of the order of the interatomic distances interact with the nuclei of the sample, the interference of waves scattered from each nucleus leads to Bragg diffraction. The scattered wave from each nucleus, being isotropic, spreads out over all directions, and the detector collects the interference of all the waves at that point. The collected wavefronts will only be in phase with each other, leading to constructive interference, if the extra distance traveled is a whole number of wavelengths:

$$n\lambda = 2d \sin(\theta/2) \quad (2.37)$$

where  $n$  is any integer and  $d$  the distance of the nuclei one from each other. Eq.(2.37) immediately gives a relationship between the neutron wavelength and a property of the sample.

By following the general derivation for any scattering theory, as seen in section 2.1.1, for light scattering, we start by interpreting the scattering in terms of the

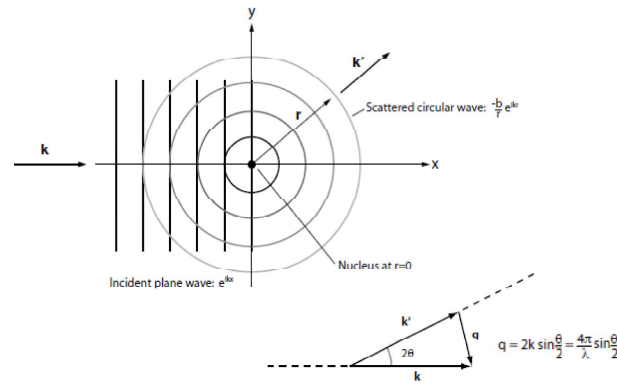


**Figure 2.6:** Elastic scattering of neutrons with a nucleus in a given position.

neutrons wavevectors of magnitude  $2\pi/\lambda$ , as shown in Fig.2.6. In the hypothesis that in the scattering event the neutron does not exchange energy with the system, its wavelength does not change, while its wavevector changes direction. Thus the magnitude of the initial wavevectors  $\mathbf{k}_i$  and of the final wavevectors  $\mathbf{k}_s$  are the same and the exchanged wave-vector,  $\mathbf{Q} = \mathbf{k}_s - \mathbf{k}_i$ , is given by

$$|\mathbf{Q}| = Q = \frac{4\pi}{\lambda} \sin(\theta/2) \quad (2.38)$$

as shown in Fig.2.6. Therefore Eq.(2.37) can now be expressed in terms of  $Q$  as

$$2\pi/Q = d/n \quad (2.39)$$

By introducing the momentum transfer, all the expressions relating the neutron scattering event to the real space properties of the sample in real space can be expressed in terms of  $Q$  and the inverse relationship between distance and  $Q$  (Eq.2.39) becomes fundamental. Indeed to explore large-scale structure within the sample very small values of  $Q$  are required and conversely small distance scales are observed via large  $Q$  values, as we will better explain in the following. However since  $Q$  depends on two parameters, wavelength and scattering angle, it can be changed by changing either one or both quantities.

## Relationship Between Scattering and Structure

As in any scattering experiment, all the information about the properties of the system are embodied in the scattered intensity  $I(Q)$ , generally given by

$$I(Q) = f(\sigma)C(Q)S(Q) \quad (2.40)$$

where  $S(Q)$  is the structure factor, defined as the density probability that neutrons are scattered and that exchange a wavevector in the range  $Q - Q + dQ$ ,  $C(Q)$  accounts for all the factors due to the spectrometer and  $f(\sigma)$  expresses the interaction neutron-nucleus as a function of the scattering cross-section  $\sigma$ .

In order to express  $S(Q)$ , in terms of the positions of the nuclei in the sample, let's start by considering a neutron as a one-dimensional wave plane traveling along the x-axis (101), in analogy to derivation followed for light scattering in terms of the electric fields. It can be written as

$$\psi(x, t) = \psi_0 \cos(2\pi x/\lambda - \omega t) \quad (2.41)$$

where  $\lambda$  is the wavelength,  $\omega$  is the angular frequency and  $t$  is the time. The term  $2\pi x/\lambda$  gives the phase of the wave at a point at distance  $x$  from an arbitrary origin and thus the relative phase of two waves, starting in phase and traveling over different path to a detector.

The plane wave in Eq.(2.41), striking a nucleus in a point  $O$ , is scattered as a spherical wave, but in the case of isotropic elastic scattering, far enough from its origin, and in particular at the detector site, it can be approximated by a plane wave, of amplitude proportional to  $1/|\mathbf{r}| = 1/r$ . The incident and the scattered waves are respectively defined by the vectors  $\mathbf{k}_i$  and the scattered one by the vector  $\mathbf{k}_s$  and the angle between  $\mathbf{k}_i$  and  $\mathbf{k}_s$  is the scattering angle  $\theta$ . Assuming that there is no change in phase upon scattering, the phase difference depends only on the different distance traveled,  $d$ , and it can be expressed, in terms of the vector  $\mathbf{r}$  and of the wavevectors, as

$$\Delta\phi = \frac{2\pi}{\lambda}(\mathbf{k}_s \cdot \mathbf{r} - \mathbf{k}_i \cdot \mathbf{r}) = \frac{2\pi}{\lambda}\mathbf{Q} \cdot \mathbf{r} \quad (2.42)$$

being  $\mathbf{Q}$  the exchanged wave-vector as defined before. Taking into account the  $r$  dependence of the amplitude of the scattered wave, one can write:

$$\psi'(x, t) = -\frac{b}{r} \cos(\mathbf{Q} \cdot \mathbf{r} - \omega t) \quad (2.43)$$

where  $b$ , the so-called scattering length, is the amplitude of the scattered wave relative to that of the incident one. By replacing the cosine in Eq.(2.43) with the more powerful notation of complex exponentials, the wave scattered can be written as

$$\psi'(x, t) = -\frac{b}{r} e^{i(\mathbf{Q} \cdot \mathbf{r} - \omega t)} = -\frac{b}{r} e^{i\mathbf{Q} \cdot \mathbf{r}} e^{-i\omega t} \quad (2.44)$$

The frequency term in  $\omega t$  will only change if a change in the energy of neutrons occurs, thus it can be ignored when elastic scattering is considered. The relative amplitude of waves scattered by any of the  $N$  nuclei in the sample just depends on the term  $b \exp(-i\mathbf{Q} \cdot \mathbf{r})$ , thus the total amplitude at the detector can be easily expressed as

$$\psi'(Q) = -\frac{b}{r} \sum_{i=1}^N e^{i\mathbf{Q} \cdot \mathbf{r}_i} \quad (2.45)$$

Taking into account the interference of the waves scattered by different nuclei, Eq.(2.45) gives the scattered intensity as

$$\begin{aligned} I(Q) = \psi(Q)\psi^*(Q) &= \sum_{i=1}^N \frac{b_i}{r} e^{+i\mathbf{Q} \cdot \mathbf{r}_i} \sum_{j=1}^N \frac{b_j}{r} e^{-i\mathbf{Q} \cdot \mathbf{r}_j} = \\ &= \frac{1}{r^2} \sum_{i=1}^N \sum_{j=1}^N b_i b_j e^{+i\mathbf{Q} \cdot (\mathbf{r}_i - \mathbf{r}_j)} \end{aligned} \quad (2.46)$$

Therefore this result is independent of the choice of the origin,  $O$ , since only the differences  $(\mathbf{r}_i - \mathbf{r}_j)$  enter into the final formula. Thus Eq.(2.46) is the basis for calculating the structure factor  $S(Q)$ , under the elastic approximation. As shown by Eq.(2.46),  $S(Q)$  depends on the relative positions of each pair of atoms within the sample.

In order to evaluate the length scattering  $b$ , we remind that its squared modulus  $bb^*$  is the probability that an incident plane wave is scattered in the direction  $\mathbf{r}$ . Then we describe the interaction between the neutron and the nucleus by the time-independent Schrödinger equation

$$\left( \frac{-\hbar^2}{2m} \nabla^2 + V(\mathbf{r}) \right) \psi(r) = E\psi(r) \quad (2.47)$$

where  $\nabla^2$  is the Laplacian operator and  $V(\mathbf{r})$  is the so-called Fermi pseudopotential. Since nuclear interactions are relevant only at very short distances ( $10^{-13} \text{cm}$ ), it can be shown that  $V(\mathbf{r})$  can be replaced by a delta function times the constant  $b$

$$V(\mathbf{r}) = -\frac{2\pi\hbar^2}{m} b \delta(\mathbf{r}) \quad (2.48)$$

The required solution of Eq.(2.47), obtained by a perturbation method in the first

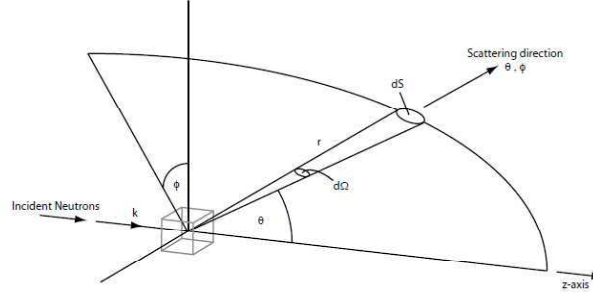


**Figure 2.7:** Geometry of a scattering experiment.

Born approximation, is stationary and satisfies the boundary conditions. At large distances it is of the form

$$\psi'(\mathbf{r}, t) = e^{i(\omega t - \mathbf{r} \cdot \mathbf{k}_i)} + \frac{b}{r} e^{i(\omega t - \mathbf{k}_f \cdot \mathbf{r})} \quad (2.49)$$

where the first term corresponds to the incident neutron beam and the second to the scattered one. After some calculation, when the quantum state of the nucleus or, equivalently, its energy  $E$  do not change, the following solution is obtained

$$\psi(\mathbf{r}) = e^{i\mathbf{k}_i \cdot \mathbf{r}} + \frac{e^{i\mathbf{k}_i \cdot \mathbf{r}}}{r} \frac{m}{2\pi\hbar^2} \int \int \int e^{-i\mathbf{k}_s \cdot \mathbf{r}'} V(\mathbf{r}') e^{i\mathbf{k}_i \cdot \mathbf{r}'} d\mathbf{r}' \quad (2.50)$$

By introducing the exchanged wave-vector  $\mathbf{Q}$ , as defined in Eq.(2.38), and assuming elastic scattering, from the comparison between Eq.(2.47) and Eq.(2.50) we obtain for  $b$  the following expression:

$$b = \frac{m}{2\pi\hbar^2} \int \int \int e^{-i\mathbf{Q} \cdot \mathbf{r}'} V(\mathbf{r}') d\mathbf{r}' \quad (2.51)$$

This shows that  $b$  is the Fourier transform of the Fermi pseudopotential as defined in (Eq.(2.48)). Its sign is a conventional choice (a negative value of  $b$  is associated to a repulsive interaction potential), whilst its modulus describes the strength of the interaction with the neutrons. Moreover, being dependent on the nucleus type, it allows to distinguish different isotopes, such as hydrogen and deuterium, leading to the isotopic substitution technique.

## Scattering Cross-Section

In a general scattering experiment a beam of monochromatic neutrons with momentum  $\hbar\mathbf{k}$  and energy  $E = \hbar^2 k^2 / 2m$  impinging on a sample is scattered in a solid angle  $d\Omega$  (Fig.2.7), with final momentum and energy equal to  $\hbar\mathbf{k}'$  and



$E' = \hbar^2 k'^2 / 2m$ , respectively. The incident neutron flux,  $\Phi$ , is defined as

$$\Phi = \frac{\text{numbers of neutrons}}{\text{area} \cdot \text{time}} \frac{\text{numbers of particles}}{\text{volume}} \cdot \text{velocity} \quad (2.52)$$

The scattered particles are then collected by a detector which counts all the neutrons arriving within a solid angle  $d\Omega$  around  $\Omega(\theta, \phi)$  and, by performing an energy analysis, the double differential cross-section for each scattering event is defined as

$$\frac{d^2\sigma}{d\Omega dE} = \frac{\text{numbers of neutrons scattered in } d\Omega \text{ in directions } \theta, \phi \text{ per second}}{\text{flux of the incident beam}} \quad (2.53)$$

which gives a measurement of the probability that a neutron impinging on the sample is scattered in  $\Omega$  per unit solid angle and energy interval. If instead neutrons are collected without energy analysis, therefore the measured quantity is the differential cross-section:

$$\frac{d\sigma}{d\Omega} = \int \frac{d^2\sigma}{d\Omega dE'} dE' \quad (2.54)$$

which is interpreted as

$$\frac{d\sigma}{d\Omega} = \frac{\text{numbers of neutrons scattered in } d\Omega \text{ in directions } \theta \text{ and } \phi}{\text{flux of the incident beam } d\Omega} \quad (2.55)$$

Integrating the differential cross-section through the solid angle  $\Omega$  the *total scattering cross section* is given by

$$\sigma_{tot} = \int \frac{d\sigma}{d\Omega} d\Omega = \int_0^{2\pi} \int_0^\pi \sin \Theta d\Theta d\Phi \quad (2.56)$$

which is therefore

$$\sigma_{tot} = \frac{\text{total number of neutrons scattered in all directions per second}}{\text{flux of the incident beam}} \quad (2.57)$$

having the dimension of an area.

### Expressions for the Scattering Cross-Section

A formally correct derivation of  $\frac{d\sigma}{d\Omega}$  requires application of the scattering theory (99, 101). Nevertheless, in the case of neutrons, it can be calculated within the Born approximation, since the perturbation brought by the scattering event to the incident beam is so small that the wavefunction of the neutron-nucleus system can be factorized as the product of the wave functions of the unperturbed components of the system. In practice, this means that the amplitude of the neutron wave, scattered by a nucleus, is already very small at a distance from the scattering center which is of the order of the first neighbor distance. When this condition is realized, the cross section can be evaluated within the linear response theory: under the hypothesis that the probe does not sensibly perturbs the target, the total scattering from an ensemble of  $N$  molecules is the sum of the scattering from the individual nuclei. We can therefore evaluate the cross section starting from the Fermi's golden rule for the transition probability between the initial and final state of the system.

Let's consider the most general case of a beam of monochromatic neutrons with momentum  $\hbar\mathbf{k}$  and energy  $E = \hbar^2 k^2 / 2m$  in the initial state  $|k, s\rangle$ , impinging on a sample whose atoms are in the state  $|\lambda\rangle$  with energy  $E_\lambda$ . Neutrons will interact with the system throughout a generic potential  $V(r)$  and the transition probability,  $W_{ks\lambda \rightarrow k's'\lambda'}$ , from the initial state  $|k, s\rangle |\lambda\rangle$  to the final state  $|k', s'\rangle |\lambda'\rangle$  is given by the Fermi's golden rule. Therefore the differential cross-section can be written as

$$\left(\frac{d\sigma}{d\Omega}\right) = \frac{k}{k'} \left(\frac{m_n}{2\pi\hbar^2}\right)^2 [W_{ks\lambda \rightarrow k's'\lambda'}(V)]^2 \quad (2.58)$$

For neutrons, a good choice of  $V$  is the Fermi pseudopotential defined in Eq.(2.48). Indeed being the neutron wavelength of the order of  $\approx 10^{-8}cm$  and the range of the nuclear forces is of the order of  $\approx 10^{-13}cm$ , neutrons see the atoms as points and the scattering from a single atom is characterized only by the scattering length  $b$  and the  $\delta$  function.

However in the simple case of a neutron scattered by a single nucleus at a fixed point  $\mathbf{r}$ , the expression for the differential cross-section can be easily derived. Indeed the number of scattered neutrons through the infinitesimal surface  $dS$  per second is given by

$$v dS |\psi_i|^2 = v dS \frac{|b|^2}{r^2} = v |b|^2 d\Omega \quad (2.59)$$

since the flux of neutrons with velocity  $v$  is  $\Phi = v |\psi_i|^2 = v$ . Therefore the differential cross-section of Eq.(2.55) can be written as

$$\frac{d\sigma}{d\Omega} = \frac{v |b|^2 d\Omega}{\Phi d\Omega} = |b|^2 \quad (2.60)$$

and by integrating over all the space, the total cross-section  $\sigma$  will be

$$\sigma = \int \int \frac{d\sigma}{d\Omega} d\Omega = 4\pi b^2 \quad (2.61)$$

### Coherent and Incoherent Elastic Scattering

In the previous paragraph we have seen how the differential cross-section can be written in the case of a wave scattered by a single nucleus. Let's now consider the more general case of  $N$  identical atoms, and assume that the  $j$ -nucleus in the position  $j$  has length scattering  $b_j$ . Therefore the pseudopotential for a system of  $N$ -nuclei is given by the sum of the  $N$  terms  $V_j(\mathbf{r}_j)$  for any nucleus and Eq.(2.48) becomes

$$V_j(\mathbf{r}_j) = -\frac{2\pi\hbar^2}{m} b_j \delta(\mathbf{r}_j) \quad (2.62)$$

In the same approximation the differential cross-section for  $N$  scatterers is therefore:

$$\left( \frac{d\sigma}{d\Omega} \right) (\mathbf{Q}) = \overline{\left\langle \left| \sum_{j=1}^N b_j e^{i\mathbf{Q} \cdot \mathbf{r}_j} \right|^2 \right\rangle} = \left\langle \sum_{i,j=1}^N \overline{b_j b_i^*} e^{i\mathbf{Q} \cdot \mathbf{r}_{ji}} \right\rangle \quad (2.63)$$

where  $r_{ji} = r_i - r_j$  defines the relative position of the scatterers  $j$  and  $i$ . The  $\langle \rangle$  and the horizontal bar, represent the thermal average over all the position occupied by the nuclei and the average over the isotopes distribution, the nuclear spin orientation and the  $b_j$  values. Moreover by splitting the sum over  $j, i$ , being  $\langle b_j b_i^* \rangle$  equal to  $|\langle b \rangle|^2$ , if  $j = i$ , and to  $\langle |b|^2 \rangle$ , if  $j \neq i$ , the differential cross-section (Eq.(2.63)) can be seen as the combination of two components, a coherent and an incoherent one:

$$\left( \frac{d\sigma}{d\Omega} \right) = \left( \frac{d\sigma}{d\Omega} \right)_{coh} + \left( \frac{d\sigma}{d\Omega} \right)_{incoh} \quad (2.64)$$

where

$$\left( \frac{d\sigma}{d\Omega} \right)_{coh} = |\bar{b}|^2 \left| \sum_{l=1}^N e^{i\mathbf{Q} \cdot \mathbf{r}_l} \right|^2 \quad (2.65)$$

and

$$\left(\frac{d\sigma}{d\Omega}\right)_{incoh} = N \left[ \overline{|b|^2} - |\bar{b}|^2 \right] = N \overline{|b - \bar{b}|^2} \quad (2.66)$$

From the physical point of view this means that neutrons don't see the array of nuclei as an ensemble of atoms with uniform scattering potential, but it changes from site to site. Nevertheless we can define an average potential, represented by the average scattering length  $\langle b \rangle$ , and imagine the array of nuclei as an "average array", which gives the coherent interference between the scattered neutrons, plus a random distribution of deviations from this average, which contribute to the incoherent scattering from the sample. Therefore the coherent contribution results from the interference between waves scattered by different nuclei, giving information about the structure of the sample through the pair-correlation function (both at the intramolecular and the intermolecular distances). On the contrary the incoherent scattering depends only on the isotropic fluctuations of the length  $b_j$  from its mean value, and is consequently  $Q$ -independent.

In conclusion, the information about the structure of the sample, is contained in the coherent contribution of the differential cross-section, which can be expressed in terms of the Static Structure Factor,  $S(\mathbf{Q})$ . Indeed, in general, structural and dynamical information about the system can be described by introducing the time-dependent radial distribution function (or pair-correlation function)  $g(\mathbf{r}, t)$ , defined as the probability that, within our sample, there will be a nucleus at the origin of our coordinate system at time zero as well as a nucleus at position  $\mathbf{r}$  at time  $t$ . In particular, the static structure of the system is obtained by the radial-distribution function evaluated at the time  $t = 0$ . This is related to the density fluctuations, which yield to the static structure factor  $S(Q)$ , defined as:

$$S(Q) = \frac{1}{N} \left\langle \sum_{i,j}^N e^{i\mathbf{Q} \cdot \mathbf{r}_{ij}} \right\rangle \quad (2.67)$$

and directly measured via the coherent cross-section. It is indeed defined as the Fourier Transform of the radial distribution function  $g(r)$ .

Indeed the differential cross-section per atom can be written as

$$\begin{aligned} \frac{1}{N} \left[ \frac{d\sigma}{d\Omega}(\mathbf{Q}) \right] &= \frac{1}{N} \left[ \frac{d\sigma}{d\Omega}(\mathbf{Q}) \right]_{coh} + \frac{1}{N} \left[ \frac{d\sigma}{d\Omega}(\mathbf{Q}) \right]_{inc} = \\ &= \bar{b}^2 S(Q) + (\bar{b}^2 - \bar{b}^2) = b_{coh}^2 S(Q) + b_{incoh}^2 \end{aligned} \quad (2.68)$$

where  $b_{coh} = \bar{b}$  is the coherent scattering length and  $b_{incoh}^2 = \bar{b}^2 - \bar{b}^2$  defines the

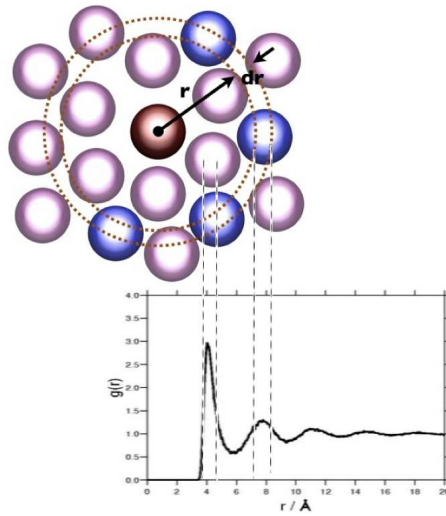


**Figure 2.8:** Typical radial distribution function  $g(r)$  for a liquid. The peaks indicate that the atoms are packed around each other in 'shells' of nearest neighbors and their attenuation at increasing radial distances from the center indicates the decreasing degree of order from the center particle.

incoherent scattering length of the sample, being, respectively, the average and the standard deviation of the length scattering distribution, respectively.

For liquids/amorphous systems, the  $g(r)$  has a "smooth" behavior approaching a limiting value of 1 at long distances, suggesting the absence of "long-range order", as shown in Fig.2.8. Thus the structure factor does not exhibit sharp peaks, although showing a certain degree of order at short-range. Moreover, being isotropic, the vectors  $r$  and  $Q$  can be substituted by their moduli and  $S(Q)$  can be written as:

$$S(Q) = 1 + \frac{1}{N} \left\langle \sum_{i \neq j} e^{-iQ(r_i - r_j)} \right\rangle \quad (2.69)$$

or, alternatively, as a function of the radial distribution function, as:

$$S(Q) = 1 + \rho \int_V g(r) e^{-iQr} dr \quad (2.70)$$

where the average number density of particles,  $\rho = N/V$  has been introduced. For a monoatomic fluid, the high and low- $Q$  limits of  $S(Q)$  are:

$$\lim_{Q \rightarrow \infty} S(Q) = 1 \quad (2.71)$$

and

$$\lim_{Q \rightarrow 0} S(Q) = \rho \chi_T k_B T \quad (2.72)$$

being  $\chi_T$  the isothermal compressibility.

### 2.2.2 Small-Angle Neutron Scattering

The theory of Neutron Scattering discussed above is focused on atomic properties. Nevertheless there are many problems in which the involved lengths scales are larger than the typical interatomic distances, thus it is useful to describe the system in term of its mesoscopic properties and we need to perform experiments at small  $Q$ . Indeed by inverting Eq.(2.39) the relation between the wave-vector  $Q$  and the investigated length scales, can be obtained:

$$Q = \frac{2\pi}{d} \quad (2.73)$$

where  $Q$  relates to the scattering angle throughout Eq.(2.38) and has the units of the inverse distance.

For example colloids, proteins, macromolecules have typical length scales of the order of the nanometers up to the micrometers, thus scattering at low angles is required to obtain information on these large structures. For this reason the technique is known as Small-Angle Neutron Scattering, or SANS (102, 103) and it will give different information with respect to diffraction. Indeed whilst from diffraction we obtain the static structure factor  $S(Q)$  and the pair-correlation function  $g(r)$  on distances of the order of the Å, in this case information about the atomic structure are lost, and information about shape, dimension and aggregation of particles can be derived.

In this case the expression of the scattering cross-section can be written by introducing the *scattering length density*, defined as

$$\rho(\mathbf{r}) b_i \delta(\mathbf{r} - \mathbf{r}_i) \quad (2.74)$$

or, equivalently, as

$$\rho = \frac{\sum_i^N b_i}{V} \quad (2.75)$$

where  $b_i$  is the scattering length of the  $i$ -atom and  $V$  is the volume containing  $N$  atoms. In particular the coherent contribute of the scattering cross-section of Eq.(2.65) can be rewritten, by replacing the sum over all the nuclei by the integral

normalized by the sample volume:

$$\left(\frac{d\Sigma(\mathbf{Q})}{d\Omega}\right) = \frac{N}{V} \left(\frac{d\sigma(\mathbf{Q})}{d\Omega}\right) = \frac{1}{V} \left| \int_V \rho(\mathbf{r}) \exp(i\mathbf{Q} \cdot \mathbf{r}) d\mathbf{r} \right|^2 \quad (2.76)$$

where  $\left(\frac{d\Sigma}{d\Omega}\right)$  is the macroscopic cross-section.

Eq.(2.76) is usually known as "Rayleigh-Gans equation" and gives the relation between small-angle scattering and the inhomogeneities in the scattering length density  $\rho(\mathbf{r})$ . The integral term is the Fourier transform of the scattering length density distribution and the differential cross section is proportional to the square of its amplitude. This implies that the phase information is lost and we cannot simply perform the inverse Fourier transform to go from the macroscopic cross section back to the scattering length density distribution.

In the case of particulate systems, where we have "countable" units that make up the scattering, we can think about the spatial distribution of those units such that

$$\left| \int_V \rho(\mathbf{r}) d\mathbf{r} \right|^2 \rightarrow \sum_i^N \sum_j^N \rho(\mathbf{r}_i - \mathbf{r}_j) \quad (2.77)$$

In non-particulate systems a statistical description may be appropriate whereby  $\rho(r)$  is described by a correlation function.

In particular, in the case of a two phase system, such as a particle suspension, in which two incompressible phases exist with length densities  $\rho_1$  and  $\rho_2$ , respectively, we can split the scattering volume in  $V = V_1 + V_2$  and rewrite Eq.(2.76) as:

$$\left(\frac{d\Sigma(\mathbf{Q})}{d\Omega}\right) = \frac{1}{V} \left| \int_{V_1} \rho_1(\mathbf{r}) e^{i\mathbf{Q} \cdot \mathbf{r}} d\mathbf{r}_1 + \int_{V_2} \rho_2(\mathbf{r}) e^{i\mathbf{Q} \cdot \mathbf{r}} d\mathbf{r}_2 \right|^2 \quad (2.78)$$

Therefore, being  $V_2 = V - V_1$ , we can write the macroscopic cross-section as:

$$\left(\frac{d\Sigma(\mathbf{Q})}{d\Omega}\right) = \frac{1}{V} (\rho_1 - \rho_2)^2 \left| \int_{V_1} e^{i\mathbf{Q} \cdot \mathbf{r}} d\mathbf{r}_1 \right|^2 \quad (2.79)$$

where the differences between the density length scattering embodies all the information about the material (such as density or composition) and the radiation (such as the length scattering), whilst the integral term describes the spatial arrangement of the system. The above equation leads to the "Babinet's Principle" that two structures, which are identical other than for the interchange of their scattering length densities, give the same incoherent scattering, due to the loss of phase information. For this reason in some cases it is useful to apply to the important "contrast matching" technique, often used in SANS to distinguish the particle from the matrix in which it is embedded.

In any Small-Angle Scattering experiment, a beam of collimated, though not necessarily monochromatic, neutrons is directed at a sample, illuminating a small scattering volume,  $V$ , and it is thus partially transmitted by the sample, whilst some is absorbed and some is scattered. A detector, or any detector element, of dimensions  $dx \times dy$  positioned at some distance  $L$  (usually between 2 and 20 m) and scattering angle  $\theta$  from the sample, collects the flux of scattered radiation into a solid angle element,  $\Delta\Omega = dxdy/L^2$ . This flux,  $I(\lambda, \theta)$ , may be generally expressed as:

$$I(\lambda, \theta) = I_0(\lambda) \Delta\Omega \eta(\lambda) T V \frac{d\sigma(Q)}{d\Omega} \quad (2.80)$$

where  $I_0$  is the incident flux,  $\eta$  is the detector efficiency (sometimes called the response),  $T$  is the sample transmission and  $(d\sigma(Q)/d\Omega)$  is the microscopic differential cross-section. The first three terms of Eq.(2.80) are clearly instrument-specific, whilst the last three are sample-dependent. In light of what shown above, the differential cross-section determined through SANS experiments can be easily modeled as

$$I(Q) = \frac{d\sigma(Q)}{d\Omega} = N_p V_p^2 (\Delta\rho)^2 P(Q) S(Q) + B_{inc} \quad (2.81)$$

where  $N_p$  is the number concentration of scattering bodies, i.e. particles,  $V_p$  is the volume of one scattering body,  $(\Delta\rho)^2$  is the square of the difference in neutron scattering length density (or contrast),  $P(Q)$  is a function known as the form factor, accounting for interference of neutrons scattered by different objects within the same particle and  $S(Q)$  is the interparticle structure factor (Eq.(2.67)), which accounts for the interference of neutrons scattered by different particles. In particular the static structure factor can be assumed equal to 1 for sufficiently dilute, non interacting systems and the  $Q$  dependence of the scattered intensity reflects only the internal structure of the particles. Fig.2.9 schematically shows the effect of  $S(Q)$  on  $I(Q)$ : non-interacting particles (hard spheres) and repulsive interactions push down  $I(Q)$  at small  $Q$  as concentration increases, culminating in an ordered structure with a "Bragg like" peak; attractive interactions tend to increase scatter at small  $Q$ , as transient large particles or actual aggregates form.  $B_{inc}$  is the (isotropic) incoherent background signal, often due to hydrogen, but often in reality also containing significant inelastic scattering.

## Data Reduction and Data Analysis

The two terms "data reduction" and "data analysis" are often used as alternatives, though technically they refer to different procedures. The data reduction is the correction of raw data from all instrumental and experimental artifacts, leading



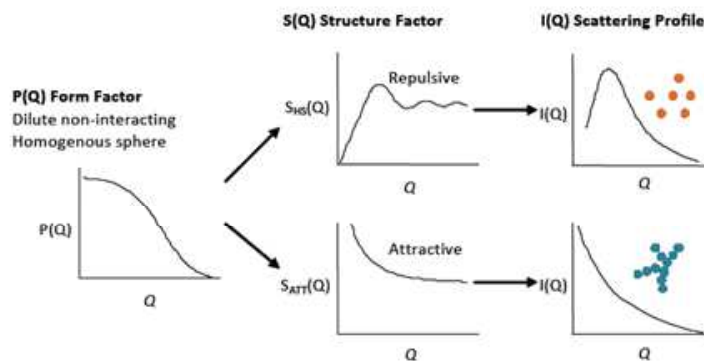


**Figure 2.9:** Schematic representation of  $P(Q)$  and  $S(Q)$  for both repulsive and attractive homogeneous spheres and their contribution to  $I(Q)$ .

from the measured intensity of scattered neutrons to the differential cross section; whilst the latter include the process of interpreting the data, fitting models, etc.

After averaging the 2-D scattering images to obtain the most commonly known 1-D small angle scattering pattern for the macroscopic cross section as a function of  $Q$ , the following steps are performed. First measurements of the direct beam are performed, in order to evaluate the transmission with respect to the empty beam; then the contribution of the empty cell is subtracted from the total scattering and the collected data can be normalized to the intensity of the transmitted beam. Secondly, the incoherent scattering, mainly coming from the hydrogen molecules, and determining a flat background is subtracted before the data analysis. This subtraction is a delicate point, since an under or over estimate of the incoherent background may misrepresent the slope or the position of a minimum in  $Q$  and thus alter the data interpretation. Different methods can be employed:

- The incoherent background can be estimated with measurement at the highest  $Q$  ( $> 0.4 \text{ \AA}^{-1}$ ) because the coherent scattering becomes negligible for big objects typical of soft matter.
- For very dilute deuterated compound in hydrogenated solvent, the subtraction of the scattering from the solvent is sufficient.

- A reference sample with no structure and containing the same amount of H and D molecules (for example, a mixture of  $H_2O/D_2O$ ) can be measured. This requires the exact knowledge the sample composition or the preparation of a mixture having the same transmission as the sample.
- If the scattering cross section has a  $Q$  dependence, it can be written as  $d\sigma/d\Omega \propto AQ^{-d} + B$ , where  $B$  represents the background and supposing that at high  $Q$  the Porod regime is reached, the incoherent background is given by the slope.

In our case the incoherent scattering has been estimated from a measurement done on the pure solvent ( $D_2O$ ).

Once the various instrumental effects have been removed and the data are put on an absolute scale of  $d\sigma(Q)/d\Omega(Q)$ , it is necessary to perform some sort of analysis to extract useful information. There are essentially two classes of analysis: model-dependent and model-independent, the former consisting of building a mathematical model of the scattering length density distribution, whilst the latter consisting of direct manipulations of the scattering data to yield useful information.

One of the most useful methods to extrapolate details on the sample from the  $I(Q)$  is the traditional graphical plot, which allows to distinguish between the  $Q$  regions where the Guinier (low  $Q$ ) or the Porod (high  $Q$ ) approximations hold. In particular the Guinier approximation relates the low  $Q$  part of the scattering profile to the radius of gyration,  $R_g$ , throughout the relation:

$$I(Q) = I(0)e^{-\frac{(QR_g)^2}{3}} \quad (2.82)$$

and in this region, being  $QR_g < 1$ , the form factor results insensitive to the particle shape. The high  $Q$  region, instead, embodies information about the scattering from local interfaces which can be obtained throughout Porod analysis, rather than the overall inter-particle correlations. In this case the scattering intensity can be modeled as

$$I(Q) \sim AQ^{-D} + B \quad (2.83)$$

where  $D$  is the so-called *Porod exponent*, relating to the fractal dimension of the system. In particular for isolated particles,  $D = 1$  is found for rods,  $D = 2$  for discs and  $D = 4$  for spheres, whilst in the case of aggregates of particles, values of  $D = 1$  characterize a chain,  $D < 1$  weakly interacting particles and  $D > 1$  spherical or non unidimensional aggregates. However a value of  $D$  between 3 and 4 characterizes rough surfaces with fractal dimension  $F$ , being  $D = 6 - F$ .

## Model-independent Analysis for Colloidal Suspensions of Microgels

Besides using standard models, information about the system can also be obtained throughout more detailed models which take into account the specific characteristics of the system.

The SANS differential cross-section  $I(Q)$  is generally given by Eq.(2.81) and, as explained above, in dilute suspensions, as those investigated here, the problem is reduced to model the form factor  $P(Q)$ , reflecting the intra-particle structure.

In particular in this work finding a suitable scattering function for colloidal suspensions of microgel particles, has been more complicated with respect to the case of polymer solutions, due to the complexity of the synthesis process. Indeed when a cross-linker generating the network is introduced, the polymer chains become connected one to each other. This determines non uniformity in the distribution and concentration of the polymer chains, leading to constraints to their relative arrangements. It has been found (65, 66) that similar network systems can be modeled through a deformable lattice model of blobs with two characteristic length scales: a short correlation length,  $\xi$ , which accounts for the rapid fluctuations of the position of the polymer chains, and a long correlation one,  $R_g$ , associated to the regions with higher polymer density and slower dynamics, which arise from the constraints imposed by junction points or clusters of such points (blobs). In particular, according to Shibayama et al. (66, 67, 76), while in the case of pure polymer solutions a Lorentzian contribution accounts for the whole elastic intensity  $I(Q)$ , in the case of cross-linked polymer chains, a Gaussian term accounting for the static inhomogeneities must to be added, thus giving the expression

$$I(Q) = \frac{I_L(0)}{\{1 + [(D + 1)/3]\xi^2 Q^2\}^{D/2}} + I_G(0)\exp(-R_g^2 Q^2/3) \quad (2.84)$$

where  $I_L(0)$  and  $I_G(0)$  are scale factors dependent on the polymer-solvent contrast and on the volume fraction of the microgel,  $\xi$  is the correlation length related to the size of the polymer network mesh and  $D$  is the Porod exponent, giving an estimate of the roughness of the interfaces between different domains of inhomogeneities. In the limit of non-interacting domains, the dense regions can be assumed to be randomly distributed within the network. Hence the spatial distribution of such regions is assumed to be a Gaussian, with standard deviation  $R_g$ . Due to the equivalence with the Guinier function,  $R_g$ , can be interpreted as the mean size of the polymer-rich or -poor domains, that is the static inhomogeneities introduced into the network by the chemical cross-links (76). On the other hand the Lorentzian term describes the fluctuations of the chains density and the interchains interactions which account for the thermodynamics of the swollen network.

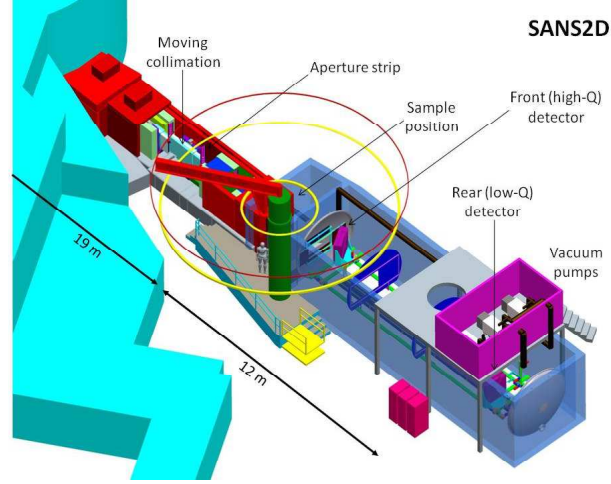


**Figure 2.10:** Sketch of the SANS2d beamline at ISIS Second Target Station (TS-2).

## Small-Angle Neutron Scattering Setup

SANS measurements have been performed on the SANS2d instrument at the 10 Hz pulsed neutron source ISIS-TS2 (104). The scattering geometry of this instrument has been set up to use a  $Q$ -range from  $0.004$  to  $0.7 \text{ \AA}^{-1}$ , corresponding to length scale from  $\sim 10$  to  $\sim 1500 \text{ \AA}$ . SANS2d is comparable to the best in the world, with an unsurpassed simultaneous  $Q$  range due to the use of time-of-flight coupled with large, movable detectors. The  $10Hz$  repetition rate of TS-2 allows wide wavelength band operation with wavelengths up to  $\sim 10 \text{ \AA}$  with a  $40 \text{ m}$  long beam line. The beamline is shown schematically in Fig.2.10.

SANS is particularly sensitive to neutrons and gamma backgrounds therefore a super mirror bender to deflect longer wavelength neutrons and  $10m$  of plain nickel guide in five  $2m$  removable sections, ensuring incident collimation, are followed by the beam chopper and then by  $10m$  of evacuated straight guide of suitable lengths to improve collimation. To maintain a continuous vacuum within the  $12m$  of guides/collimation a vacuum seals inflated with compressed air is used between the sections.

The sample is at  $\sim 19m$  from a coupled, grooved moderator, with sample-detector distances from  $\sim 2 \text{ m}$  up to  $12 \text{ m}$  with a full gain of 40% in flux per unit area reached by a sample-detector distance  $L_2 = 12m$ . A highly flexible sample area enables rapid changes of sample environment equipment by users themselves with sample-changer equipment. The SANS2d sample position is in air with access from above and can accommodate equipment up to  $2m^3$  in size, allowing to subject the samples to a range of different conditions (temperature, pressure, etc). Both disc-shaped cells and rectangular quartz cuvettes can be used with the advantage of using a larger diameter neutron beam, thus increasing the count rate on the sample. Their thickness depends on the H/D ratio in a hydrogenous sample. For

our samples quartz cuvettes of 2 mm of thickness have been used.

SANS2d is equipped with two approximately 1m square detectors mounted on a rigid rail system inside a vacuum tank, so that it can be moved in order to access the suitable scattering angle and  $Q$ . The first detector can be moved  $\pm 300$  mm sideways, whilst the second, at higher angles, can move from the beam centre up to  $\sim 1.4$ m sideways and can rotate to face the sample. A particular advantage of this choice is that if high- $Q$  is not needed both detectors may be used to improve count rate and for improved normalization and cross calibration with the small angle detector.

## 2.3 Materials and Samples preparation

### 2.3.1 Synthesis Procedure

An interpenetrated polymer-network (IPN) composed of poly(acrylic acid) (PAAc) and poly(N-isopropylacrylamide) (PNIPAM) has been synthesized by a two steps sequential method, by M. Bertoldo et al. from IPCF-CNR of Pisa, following a procedure already reported in literature (27).

Once the aqueous high concentrated suspension of IPN microgels has been prepared, all the samples at different weight concentrations have been obtained by dilution in our chemical laboratory.

**Materials** Both N-isopropylacrylamide (NIPAM) from Sigma-Aldrich and N,N'-methylene-bis-acrylamide (BIS) from Eastman Kodak were purified from hexane and methanol, respectively, by recrystallization; dried under reduced pressure (0.01 mmHg) at room temperature and stored at 253 K until used. Acrylic acid (AAc) from Sigma-Aldrich was purified by distillation (40 mmHg, 337 K) under nitrogen atmosphere in the presence of hydroquinone and stored at 253 K until used. Sodium dodecyl sulphate (SDS), 98% purity, potassium persulfate (KPS), 98% purity, ammonium persulfate, 98% purity, N,N,N',N'-tetramethylethylenediamine (TEMED), 99% purity, ethylenediaminetetraacetic acid (EDTA), NaHCO<sub>3</sub>, were all purchased from Sigma-Aldrich and used as received. Ultrapure water (resistivity: 18.2 M $\Omega$ /cm at 298 K) was obtained with Sarium<sup>®</sup> pro Ultrapure Water purification Systems, Sartorius Stedim from demineralized water. D<sub>2</sub>O (99.9 atom%) from Sigma-Aldrich. All other solvents were RP grade (Carlo Erba) and were used as received. A dialysis tubing cellulose membrane, HCWO 14000 Da, from Sigma-Aldrich, was cleaned before use by washing in running distilled water for 3 h; treating at 343 K for 10 min into a solution containing a 3.0% weight concentration of NaHCO<sub>3</sub> and 0.4% of EDTA; rinsing in distilled water at 343 K for 10 min and finally in fresh distilled water at room temperature for 2 h.

**Synthesis of PNIPAM microparticles** 65.15 g of a PNIPAM dispersion at weight concentration  $C_w=0.920\%$  were transferred into a 500 mL five-necked jacketed reactor washed up by three water/nitrogen cycles. 2.3 ml di AAc are then introduced into the reactor. 0.513 g di BIS in a solid state are added and the reaction mixture is deoxygenated, under stirring, by purging with nitrogen for 1h. 0.2086g of solid  $NH_4PS$  and 260  $\mu$ L of TEMED were added under nitrogen atmosphere of TEMED were diluted by using 5ml of deoxygenated water and transferred into the reactor at  $(295.5 \pm 0.5)K$ . 27 minutes later the mixture became turbid and was stopped by exposition to the air. The mixture is therefore transferred in a tube dialysis membrane and purified by dialysis against distilled water with frequent water change for 20 days. 426 g of dispersion were obtained. A fraction was lyophilized to determine the concentration, thus obtaining a product with 8.01% content of humidity (from TGA analysis).

**Synthesis of IPN microparticles** The IPN microgel was synthesized by a sequential free radical polymerization method. In the first step PNIPAM microparticles were synthesized by precipitation polymerization. In the second step acrylic acid was polymerized into the preformed PNIPAM network (26).  $(4.0850 \pm 0.0001)$  g of NIPAM,  $(0.0695 \pm 0.0001)$  g of BIS and  $(0.5990 \pm 0.0001)$  g of SDS were solubilized in 300 mL of ultrapure water and transferred into a 500 mL five-necked jacketed reactor equipped with condenser and mechanical stirrer. The solution was deoxygenated by purging with nitrogen for 30 min and then heated at  $(273.0 \pm 0.3)$  K.  $(0.1780 \pm 0.0001)$  g of KPS (dissolved in 5 mL of deoxygenated water) were added to initiate the polymerization and the reaction was allowed to proceed for 4 h. The resultant PNIPAM microgel was purified by dialysis against distilled water with frequent water change for 2 weeks. The final weight concentration and diameter of PNIPAM micro-particles were 1.02% and 80 nm (at 298 K) as determined by gravimetric and DLS measurements, respectively.  $(65.45 \pm 0.01)$  g of the recovered PNIPAM dispersion and  $(0.50 \pm 0.01)$  g of BIS were mixed and diluted with ultrapure water up to a volume of 320 mL. The mixture was transferred into a 500 mL five-necked jacketed reactor kept at  $(295 \pm 1)$  K by circulating water and deoxygenated by purging with nitrogen for 1 h. 2.3 mL of AAc and  $(0.2016 \pm 0.0001)$  g of TEMED were added and the polymerization was started with  $(0.2078 \pm 0.0001)$  g of ammonium persulfate (dissolved in 5 mL of deoxygenated water). The reaction was allowed to proceed for 65 min and then stopped by exposing to air. The obtained IPN microgel was purified by dialysis against distilled water with frequent water change for 2 weeks, and then lyophilized to constant weight. The PAAc second network amount in the IPN was 31.5% by gravimetric analysis and the acrylic acid monomer units content 22% by acid/base titration. The remeaning 9.5% being ascribed to BIS.

IPN samples were prepared by dispersing lyophilized IPN into ultrapure water at weight concentration 1.0 and 3.0 % by magnetic stirring for at least 3 h.

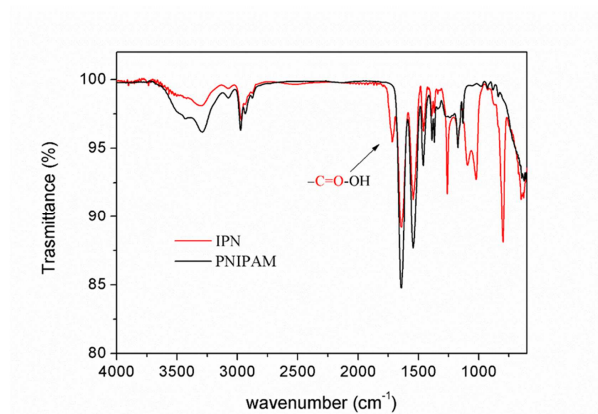


**Figure 2.11:** Comparison between the ATR spectra of lyophilized PNIPAM and IPN. Spectra have been recorded on Ge-IRE by accumulating 128 scan with a Jasco FT/IR-6200 spectrometer equipped with a Pike Technologie Miracle ATR accessory. The arrow indicates the -C=O-OH vibrational band, due to polymerization of the acrylic acid.

The weight concentration is increased by lyophilizing and redispersing a fraction of IPN microgel to decrease the water amounts and to obtain the required weight concentration. Samples at different concentrations were obtained by dilution.  $D_2O$  solutions were obtained by redispersing lyophilized IPN in  $D_2O$  by magnetic stirring for 1 day. The sample was then lyophilized and redispersed again in  $D_2O$  to obtain the final suspension at the required weight concentration. Samples at different concentrations were obtained by dilution with  $D_2O$ .

The same procedure was followed to prepare all the samples, although in some cases the involved quantities have been slightly changed to optimize the resulting IPN microgel samples.

**Characterization** The poly(acrylic acid) content in 10 g of IPN dispersion was determined by addition of 11 mL of 0.1 M NaOH, followed by potentiometric back titration with 0.1 M hydrochloric acid. The concentration of the dispersion was determined from the weight of the residuum after water removal by lyophilisation, corrected for the moisture residual amount obtained by thermogravimetric analysis (TGA). This was accomplished with a SII Nano-Technology EXTAR TG/DTA7220 thermal analyzer at 275 K/min in nitrogen atmosphere (200 mL/min). 5 mg of sample in an alumina pan were analyzed in the (313-473)K temperature range and the weight loss was assumed as moisture content.

The success of the AAc polymerization was assessed by Attenuated Total Reflectance (ATR) analysis of the recovered product after the second reaction step. As reported in Fig.2.11, the spectra clearly showed the presence of the PAAc ab-

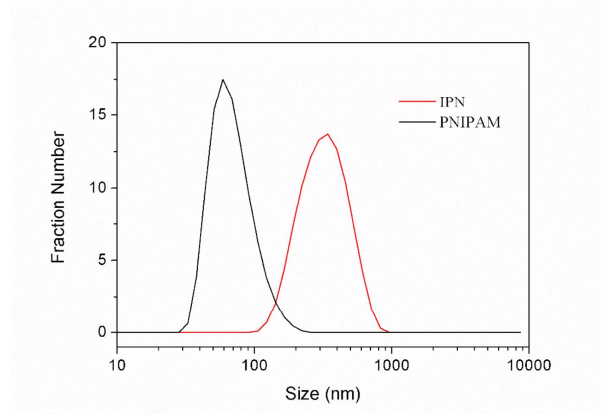


**Figure 2.12:** Particle size distributions of 0.01%wt aqueous dispersions of PNIPAM and IPN at 293K obtained through a Malvern Nanosizer.

sorption bands, the most significant being the stretching band of the carbonyl groups at  $1716\text{ cm}^{-1}$ .

The polymerization of PAAc results in a quite large increase of the particle diameter of IPN with respect to the starting PNIPAM (Fig.2.12). The amount of incorporated PAAc was determined by gravimetric analysis of the purified dispersion of the IPN and a weight increase of 46% was observed for the recovered dispersion with respect to the PNIPAM in the feed. Such weight increase corresponds to an IPN composed by 68.5% of PNIPAM network and 31.5% of PAAc network. Acid base titration provided a content of acrylic acid of 27% in the IPN, consistent with gravimetric analysis, assuming that the cross-linker accounts for the 4.5%.

### 2.3.2 Samples preparation

Samples at different weight concentrations have been obtained by dilution from the stock suspension of IPN microgel in  $H_2O$  or in  $D_2O$ . Indeed in this thesis we have investigated isotopic effects and therefore we have used both deuterium oxide ( $D_2O$ ) with purity  $> 99.9\%$  produced by Sigma-Aldrich® and ultra pure deionised water with an electroresistance above  $18\text{ m}\Omega\text{ cm}^{-1}$  obtained by a Milli-Q system present in our chemical laboratory. A glove box under a Nitrogen ( $N_2$ ) atmosphere was used during the preparation of all the diluted samples to minimize  $CO_2$  dissolution, in particular for the  $D_2O$  samples, and to minimize the presence of impurities within the sample.

To prepare all the samples at the required concentration, the dilution fraction  $x_{dil}$  has been firstly calculated through the relation



$$x_{dil} = \frac{C_{wf}}{C_{wi}} \quad (2.85)$$

where  $C_{wf}$  and  $C_{wi}$  are the final and initial weight concentrations of the IPN suspension, respectively. At this point, depending on the required final weight  $W_{SOL_f}$  of the sample, an amount  $W_{SOL_i}$  of the stock IPN suspension at  $C_{wi}$  is added into a beaker and its weight is measured with a digital balance that has an accuracy of  $\pm 0.001$  g. The amount  $W_{SOL_i}$  is calculated as

$$W_{SOL_i} = x_{dil} W_{SOL_f} \quad (2.86)$$

Finally an amount of ultrapure deionised water  $\Delta W_{H_2O}$ , given by

$$\Delta W_{H_2O} = W_{SOL_i} \left[ \frac{1 - x_{dil}}{x_{dil}} \right] \quad (2.87)$$

is added to the suspension. In the case of  $D_2O$  solutions the amount  $\Delta W_{D_2O}$  need to be calculated taking into account the fraction between the molar mass  $PM$  of  $D_2O$  and  $H_2O$ :

$$\Delta W_{H_2O} = W_{SOL_i} \left[ \frac{1 - x_{dil}}{x_{dil}} \right] \frac{PM_{D_2O}}{PM_{H_2O}} \quad (2.88)$$

where, in this case, the dilution factor  $x_{dil}$  is calculated by using the equivalent concentration in  $D_2O$ , given by

$$C_w^{D_2O} = C_w^{H_2O} PM_{H_2O} PM_{D_2O} \quad (2.89)$$

All the samples have been kept stirring for 30 minutes by using a magnetic stirrer. At this point the pH has been measured with a pH-meter CRISON BASIC 20.

Neutral pH suspensions have been obtained by increasing the pH with the addition of basic solutions of molarity  $0.2M$  of  $NaOH$  in  $H_2O$  samples and of  $KOD$  in  $D_2O$  samples in small quantities, calculated keeping constant the ratio between the weight of the amount of the basic solution  $W_{basic}$  and the weight  $W_{SOL_f}$  of the IPN suspension. The samples are left under stirring for 1 h and then the pH has been checked. In some cases the measured pH was not stable, therefore it has been left stand for a night and then remeasured. If necessary a small amount of  $W_{basic}$  has been added to optimize the pH value. The same procedure was strictly followed to prepare all the samples in order to permit a correct comparison between the results.

# Chapter 3

## Results and Discussion

This chapter is devoted to the presentation and discussion of the dynamics and the local structure of water and heavy water suspensions of PNIPAM-PAAc IPN microgels, obtained through Dynamic Light Scattering (DLS) and Small-Angle Neutron Scattering (SANS) respectively.

During the first year of Ph.D. a preliminary DLS characterization of aqueous suspensions of PNIPAM and PNIPAM-PAAc IPN microgels at low concentrations has been performed to support and improve the chemical synthesis protocol. This exchange has allowed to obtain monodisperse suspensions of IPN microgel particles with the desired sizes and responsiveness to the external stimuli. Once the synthesis procedure has been optimized, the PAAc and cross-linker content has been tuned, the carboxylic groups of PAAc have been deprotonated and high concentrated samples have been synthesized. A systematic investigation of the typical swelling and phase behavior as a function of temperature, pH, concentration and exchanged wave-vector in the high and low dilution regime has been performed for both  $H_2O$  and  $D_2O$  IPN microgel suspensions. Thereafter, through SANS measurements, the temperature, pH and concentration dependence of the intra-particle structure of the IPN microgels has been investigated during the crossover from the fully swollen to the completely shrunken state, in the high dilution regime to avoid interparticle interactions. The combination of DLS and SANS techniques has allowed to provide a preliminary picture of the phase diagram as a function of temperature, pH and concentration in both water and heavy water solutions.

### 3.1 Dynamics: Dynamic Light Scattering

The dynamics of aqueous suspensions of PNIPAM and PNIPAM-PAAc IPN microgels as a function of temperature and concentration has been studied through DLS. In particular the swelling behavior of PNIPAM and IPN microgels has been characterized in the high dilution regime in the temperature range  $293\text{ K} \leq T \leq$

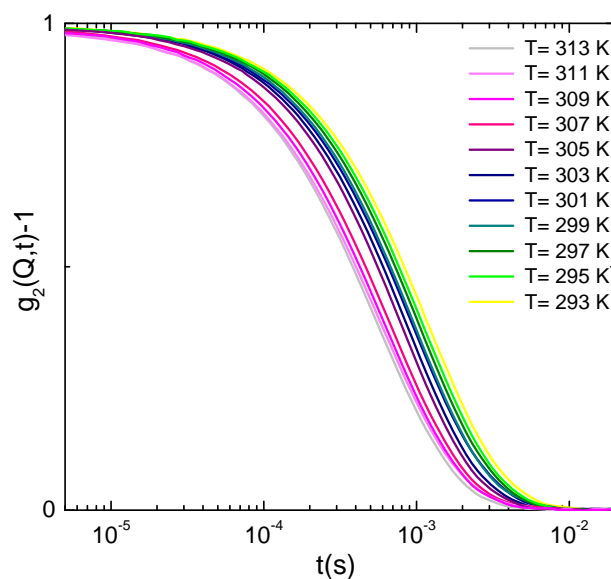


**Figure 3.1:** Normalized intensity autocorrelation functions of an aqueous suspension of IPN microgels at  $C_w=0.10$  %, pH 7 and  $\theta=90^\circ$  for the indicated temperatures.

313 K, where a Volume Phase Transition (VPT) is expected to occur. Moreover the pH and wave-vector ( $Q$ ) dependence of IPN microgels has been investigated, with particular attention to the role played by the PAAc and the possibility of driving the system through a non-ergodic transition across the VPT.

Fig.3.1 shows the typical behavior of the normalized intensity autocorrelation functions for an IPN sample at weight concentration  $C_w=0.10$  %, pH 7, collected by a detector at  $\theta=90^\circ$  with respect to the incident beam. The relaxation time, i.e the decay time of the correlation curve, is obtained from a fit with Eq.(2.34) and the hydrodynamic radius is derived through Eq.(2.30), once the viscosity is known. However, when the viscosity of the sample is unknown and approximated by the solvent viscosity and/or when the Stokes-Einstein relation does not strictly hold (for example in the shrunken high temperature state, characterized by the non spherical and/or interacting particles), the reliability of the estimated hydrodynamic radius is questionable. For these reasons in the following we will always refer to the behavior of the relaxation time rather than to the hydrodynamic radius, reminding that the relaxation of the dynamics is mainly due to the particles diffusion within the suspension, hence to their size and shape.

In this chapter we will report the results obtained on PNIPAM microgel suspensions in  $H_2O$  (Par.3.1.1) and IPN microgel suspensions in both  $H_2O$  (Par.3.1.2 and Par.3.1.3) and  $D_2O$  (Par.3.1.4) solvent, for clarifying their swelling behavior and drawing a clear picture of the IPN microgel as a function of temperature, pH and concentration, besides of the role played by the solvent.

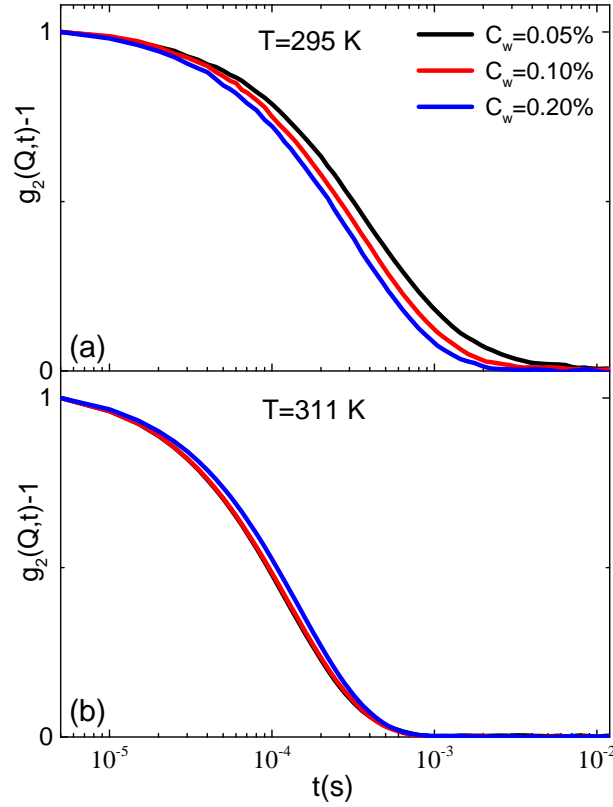


**Figure 3.2:** Normalized intensity autocorrelation functions for an aqueous suspension of PNIPAM microgels at (a)  $T=295$  K and (b)  $T=311$  K and  $\theta=90^\circ$  for the indicated concentrations.

### 3.1.1 PNIPAM microgel suspensions in $H_2O$ solvent

The swelling behavior of PNIPAM microgels has been investigated in the high dilution regime to avoid interparticle interactions and phase separation. In Fig.3.2 the typical behavior of the normalized intensity autocorrelation functions, below (panel (a)) and above (panel (b)) the Volume-Phase Transition Temperature (VPTT), for aqueous suspensions of PNIPAM microgels at three low weight concentrations ( $C_w=0.05$  %,  $C_w=0.10$  % and  $C_w=0.20$  %) collected by a detector at  $\theta=90^\circ$  with respect to the incident beam, is reported. The intensity autocorrelation functions result concentration-dependent below the VPT (Fig.3.2(a)), whilst above the VPT (Fig.3.2(b)) the spread between samples at different concentrations is widely reduced.

The relaxation time, as obtained from a fit with Eq.(2.34), is expected to decrease with temperature, as suggested by the behavior of the intensity autocorrelation curves. In Fig.3.3 its temperature behavior is reported: an almost continuous decrease with increasing temperature and a sharp transition above 305 K are ob-

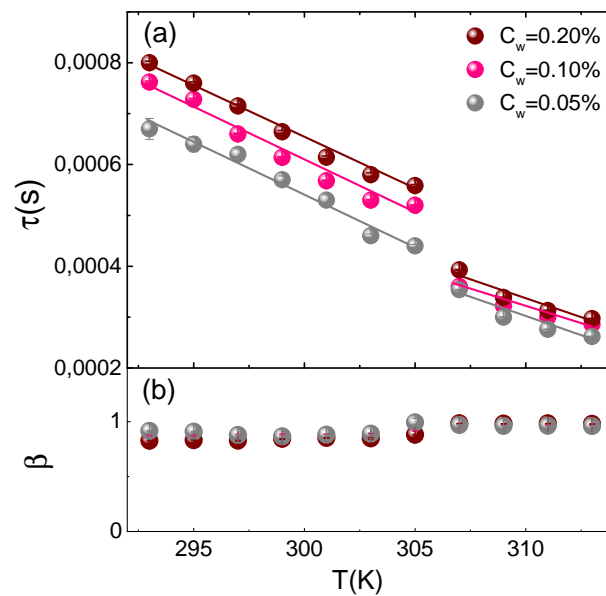


**Figure 3.3:** (a) Relaxation times and (b) stretching parameter from Eq.(2.34) for aqueous suspensions of PNIPAM microgels as a function of temperature for the indicated concentrations. Full lines in (a) are guides for eyes.

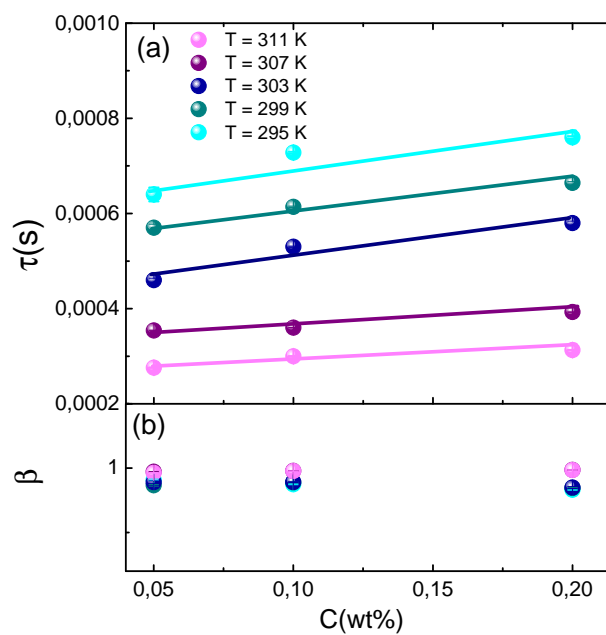


**Figure 3.4:** (a) Relaxation times and (b) stretching parameter for aqueous suspensions of PNIPAM microgels as a function of weight concentration at five fixed temperatures. Full lines in (a) are guides for eyes.

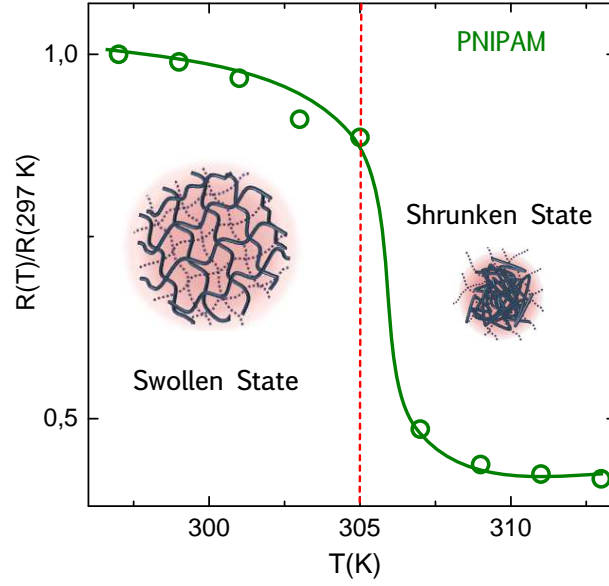


**Figure 3.5:** Normalized radius as obtained from DLS measurements for an aqueous suspension of PNIPAM microgel at  $C_w = 0.10$  % and collected at  $\theta=90^\circ$  with respect to the incident beam. Full lines are guides for eyes.

served, highlighting changes of the dynamics at the VPTT, due to the transition of the microgel particles from the swollen to the shrunken state. On the other hand the stretching parameter  $\beta$  shows a slight increase above the VPT from values slightly below 1 to values around 1, indicating a transition from slightly stretched correlation functions to a simple exponential decay with increasing temperature.

Furthermore a concentration dependence of the relaxation time is observed: the most concentrated sample at  $C_w=0.20$  % exhibits the highest values of  $\tau$  and the largest change above the VPT, whilst the decrease of the relaxation times with concentration suggests a slowing down of the dynamics by increasing concentration. This typical concentration dependence can be better visualized by looking at the relaxation time behavior as a function of concentration at five fixed temperatures, as shown in Fig.3.4: an almost linear increase with increasing concentration is observed, with lower slopes above the VPT. On the contrary, the stretching parameter does not exhibit concentration dependence, being slightly below 1 at temperature below the VPTT and around 1 above it, for all investigated samples.

In the high dilution regime the interparticle interactions can be neglected and the suspensions viscosity approximated by the water one. Therefore the Stokes-Einstein relation (Eq.2.30) can be applied with good approximation and the hydrodynamic radius can be directly estimated. In Fig.3.5 its behavior for an aqueous suspension of PNIPAM microgels at  $C_w=0.10$  % and normalized with respect to its value at 297 K, is reported. A sharp Volume Phase Transition around 305 K from a swollen hydrated state to a shrunken dehydrated one is observed, highlighting a

reduction of the particle size of about 60% due to water release.

This preliminary investigation of aqueous suspensions of PNIPAM microgels, has allowed to improve the synthesis protocol for polymer microgels and at the same time has highlighted those features of the swelling behavior that aqueous suspensions of PNIPAM-PAAc IPN microgels are expected to exhibit. As a result our attention has been focused on the IPN microgels behavior in the same range of temperature as for PNIPAM microgels, in order to provide a clear picture of the swelling and phase behavior when an additional pH-tunability of the VPT is introduced.

### 3.1.2 IPN microgel suspensions in H<sub>2</sub>O solvent

The investigation of colloidal suspensions of IPN microgels in the high dilution regime has been crucial to ensure a good control of the parameters which affect the size and the responsiveness of the microgel particles during the synthesis. In particular different batches of samples with different polymerization times, sizes, cross-linker and acrylic acid contents have been synthesized and tested through DLS measurements, in order to check reliability and reproducibility of the synthesis protocol. In this way the problems due to synthesis procedure have been reduced step by step, thus finally obtaining stable and reproducible samples.

Once a suitable synthesis protocol has been provided, the acquisition time has been changed to test its role in the swelling behavior. In particular measurements with two acquisition times, namely 10 and 60 minutes, have been performed, as reported in Fig.3.6. The temperature behavior of the relaxation time shows that acquisition time does not sensibly affect the quality of the results. Therefore the only limit to the acquisition time is the time required to reach equilibrium temperature. Thereafter the sample stability has been tested by repeating the measurements after a few months. Fig.3.7 shows the temperature behavior of the relaxation time for the same IPN microgel sample, as obtained in two runs of measurements few months apart, showing that any ageing phenomenon occurs in this time frame.

After the above positive tests, a systematic investigation of the dynamics of aqueous suspensions of IPN microgeles in response to changes of temperature, pH and concentration has been performed. In particular diluted aqueous suspension of IPN microgels at four different low weight concentrations ( $C_w=0.10$  %,  $C_w=0.15$  %,  $C_w=0.20$  %,  $C_w=0.30$  %), where the interparticle interactions are negligible and phase separation does not occur, have been characterized at both acidic and neutral pH, namely at pH 5 and 7, respectively. The results obtained on these samples have been published in the Journal of Non-Crystalline Solids (105).

The intensity correlation functions, as those reported in Fig.3.1, show a clear transition occurring at about  $T=305$  K, corresponding to the expected volume phase transition from a swollen to a shrunken state. This behavior is evidenced by

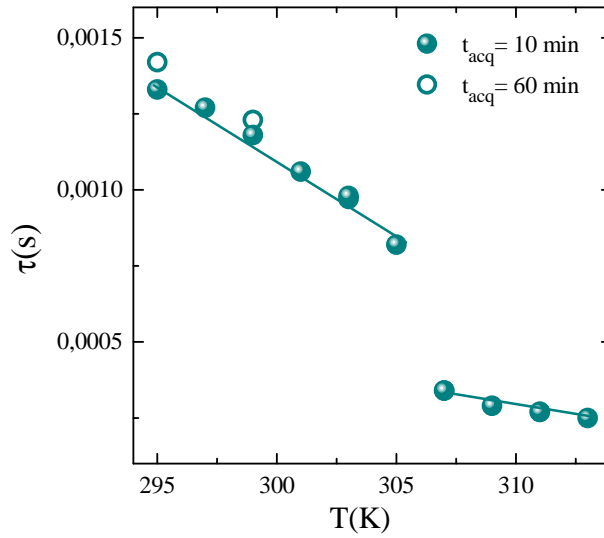


**Figure 3.6:** Comparison of the measured relaxation time of aqueous suspensions of IPN microgels as a function of temperature as collected with acquisition times of 10 minutes (bullets) and 60 minutes (open circles). Full lines are guides for eyes.

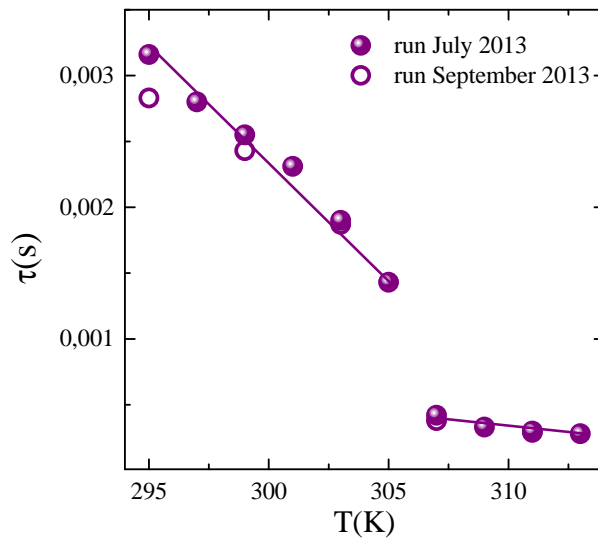


**Figure 3.7:** Relaxation times from Eq.(2.34) for an aqueous suspensions of IPN microgels as a function of temperature as collected in two different far apart in time runs of measurements, namely on July 2013 (bullets) and September 2013 (open circles). Full lines are guides for eyes.



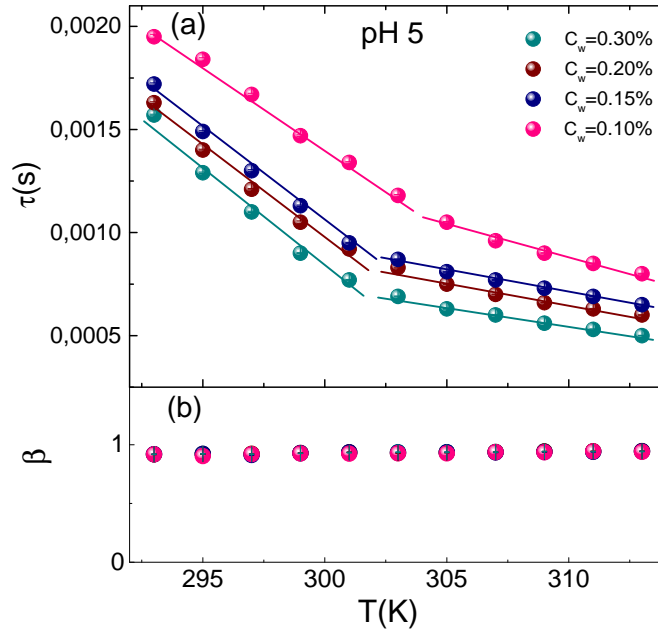


**Figure 3.8:** (a) Relaxation times and (b) stretching parameter from Eq.(2.34) for aqueous suspensions of IPN microgels as a function of temperature at pH 5 for the indicated concentrations. Full lines in (a) are guides for eyes.

looking at the temperature dependence of the relaxation time reported in Fig.3.8 and Fig.3.9 at acidic and neutral pH, respectively. At acidic pH (pH 5) the relaxation time exhibits an almost continuous decrease with increasing temperature, until a change of the slope at temperature above 303 – 305 K, depending on concentration, occurs (Fig.3.8). This behavior highlights a change of dynamics at the VPT, due to the transition of the microgel particles from the swollen to the shrunken state. On the contrary the stretching parameter  $\beta$  does not show any change with temperature and concentration, remaining just below 1, as for slightly stretched correlation functions.

This behavior is strongly affected by the pH of the solution as shown in Fig.3.9, where relaxation times and stretching parameters as a function of temperature at neutral pH (pH 7) are reported. At variance with acidic pH suspensions, in this case a sharp transition is observed. As temperature increases the relaxation time shows a slight decrease until the transition is approached around  $T=305$  K, thereafter, depending on concentrations, different behaviors are observed. For the lowest concentrated sample, at  $C_w=0.10\%$ , above 305 K the relaxation time abruptly reaches its lowest value, corresponding to a transition of the microgel particles from the swollen to the shrunken state. At increasing concentration the jump becomes smaller and smaller with an interesting swap in trend for the highest concentrated sample at  $C_w=0.30\%$ . Moreover, by increasing concentration the

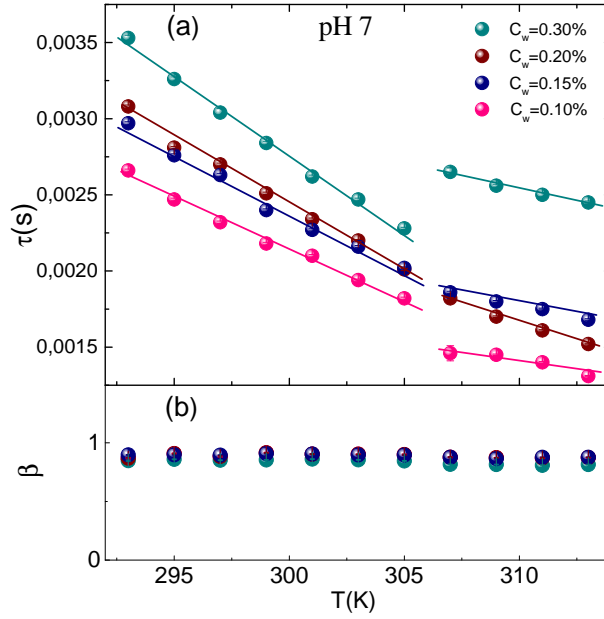


**Figure 3.9:** (a) Relaxation times and (b) stretching parameter from Eq.(2.34) for aqueous suspensions of IPN microgels as a function of temperature at pH 7 for the indicated concentrations. Full lines in (a) are guides for eyes.

relaxation time increases.

Furthermore the behavior of the relaxation time with concentration is reversed at the two pH values investigated. In addition the comparison between Fig.3.9(a) and Fig.3.8(a) shows that at neutral pH the relaxation times are always higher than at pH 5. On the other hand, as in the case of acidic pH, the stretching coefficient  $\beta$  is neither temperature nor concentration dependent and always slightly below 1.

The inversion of trend observed at different pH can be better visualized by comparing the relaxation time and the stretching coefficient behaviors as a function of concentration at both pH (Fig.3.10). Whilst at pH 5 and fixed temperature  $\tau$  rapidly decreases between  $C_w=0.10$  % and  $C_w=0.15$  %, and exhibit a linear decrease above this concentrations, at pH 7 the relaxation time increases almost linearly with concentration at temperature below the VPTT, whilst above the VPTT a non-monotonic increase of the relaxation time is observed, which needs further investigation. However these results show that the pH of the solution strongly affects the relaxation times behavior and in particular that at acidic pH their values are smaller and the transition appears to be less sharp than in the case of neutral pH. This dependence of the VPT, not only on concentration but also on pH, indicates that the presence of PAAc hugely affects the dynamics of the system. This is confirmed by the comparison with the concentration dependence of the relaxation time behavior for pure PNIPAM microgels, reported in Fig.3.4.

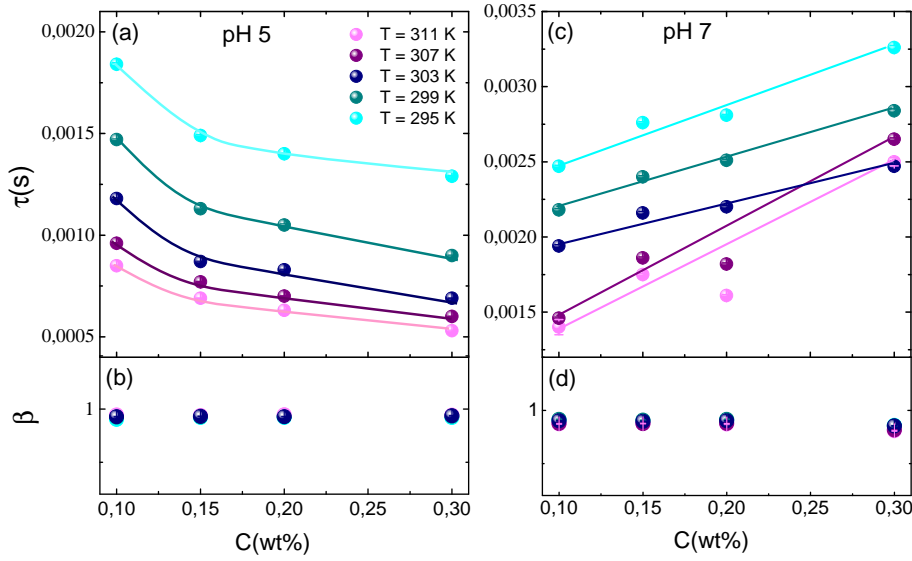


**Figure 3.10:** (a) Relaxation times and (b) stretching parameter for aqueous suspensions of IPN microgels as a function of the weight concentration at five fixed temperatures and pH 7. (c) Relaxation times and (d) stretching parameter as a function of the weight concentration at five fixed temperature values and pH 5. Full lines in (a) and (c) are guides for eyes.

Indeed the relaxation times of the IPN samples are almost an order of magnitude higher than those of pure PNIPAM and the positive slope of their behavior with concentration is preserved only at neutral pH, whilst it is reversed at acidic pH.

In Fig.3.11 the temperature dependence of the normalized hydrodynamic radius with respect to its value at room temperature ( $T=297$  K,  $R=(188.3\pm0.6)$  nm) at  $C_w=0.10$  % and pH 7, is compared to previous results at different concentrations (27, 78). The data are in good agreement, although a slight discrepancy at high temperatures above the VPT is observed. This can be ascribed to the use of the solvent viscosity in the calculation of Eq.(2.30) (instead of that, unknown, of the solution) and/or to the possible failure of the Stokes-Einstein relation at the investigated concentrations, as discussed in Sec.3.1.

In order to investigate the nature of the motion and to obtain information on different length scales we have studied the exchanged wave-vector ( $Q$ ) dependence of the relaxation time and stretching parameter. In Fig.3.12 the normalized intensity correlation functions collected at different scattering angles for a sample at  $C_w=0.20$  %,  $T=303$  K and pH 7 are reported. The behaviors of relaxation time and stretching parameter as obtained through the fit according to Eq.(2.34) are shown in Fig.3.13, as a function of the wave-vector  $Q$ .

The relaxation time, reported in a double logarithmic plot, is strongly  $Q$  dependent, with a typical power law decay described by the relation

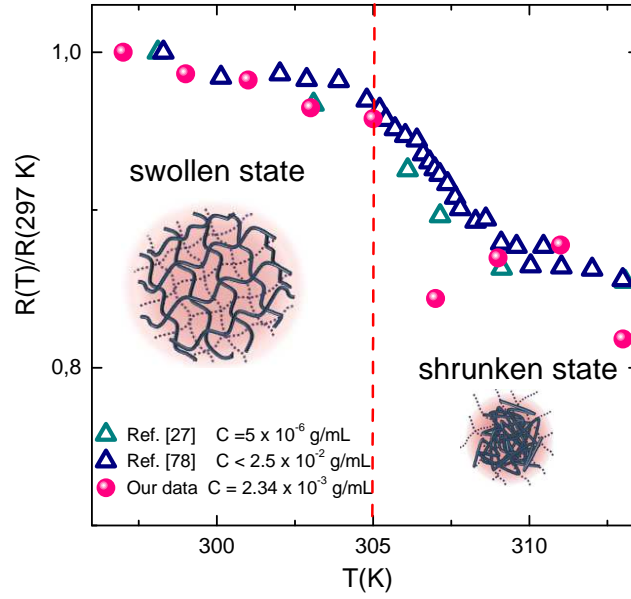


**Figure 3.11:** Normalized radius as obtained from DLS measurements for an aqueous suspension of IPN microgel at  $C_w = 0.10\%$  (equivalent to a weight/volume concentration of  $2.34 \times 10^{-3} \text{ g/mL}$ ), pH 7 and  $\theta=90^\circ$  compared with results from Ref. (27, 78).

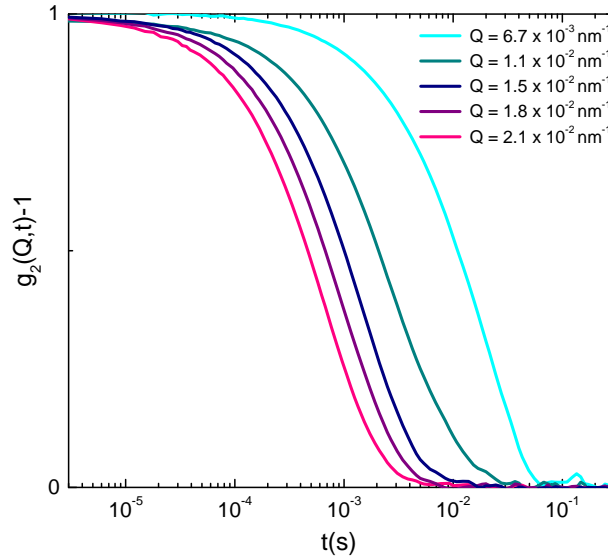


**Figure 3.12:** Normalized intensity autocorrelation curves for aqueous suspension of IPN microgels at  $C_w=0.20\%$ ,  $T=303 \text{ K}$  and pH 7 for the indicated values of the exchanged wave-vector  $Q$ .

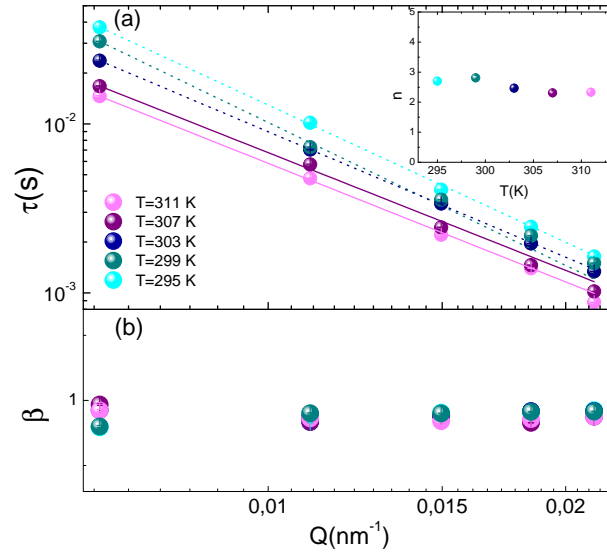


**Figure 3.13:** (a) Relaxation time and (b) stretching parameter from Eq.(2.34) as a function of exchanged wave-vector  $Q$  at  $C_w=0.10$  %, pH 7 for the indicated temperatures. Full lines are fits through Eq.(3.1) with  $n=2.33\pm0.03$  ( $T=311$  K),  $n=2.31\pm0.07$  ( $T=307$  K),  $n=2.465\pm0.008$  ( $T=303$  K),  $n=2.81\pm0.08$  ( $T=299$  K),  $n=2.70\pm0.03$  ( $T=295$  K). Inset: behavior of the exponent  $n$  as a function of temperature at  $C_w=0.10$  % and pH 7.

$$\tau = A Q^{-n} \quad (3.1)$$

where  $A$  is a constant and the exponent  $n$  defines the nature of the motion. The fits according to Eq.(3.1) (full lines) are superimposed to the data (symbols) and values of  $n > 2$  (in particular  $n$  between 2 and 3) are found, in agreement with those reported in previous experimental studies on the same microgel (78) and on different polymers (106, 107). Detailed investigations of the  $Q$ -dependence of the relaxation dynamics will be the subject of further studies. At variance with the relaxation time, the stretching parameter  $\beta$  does not show any dependence on the exchanged wave vector  $Q$ .

### 3.1.3 Deprotonated IPN microgel suspensions in H<sub>2</sub>O solvent

In the previous section we have shown that the swelling behavior of IPN microgels dispersed in water, obtained by introducing acrylic acid into the PNIPAM network, can be tuned by changing the pH of the solution. This behavior is strictly related

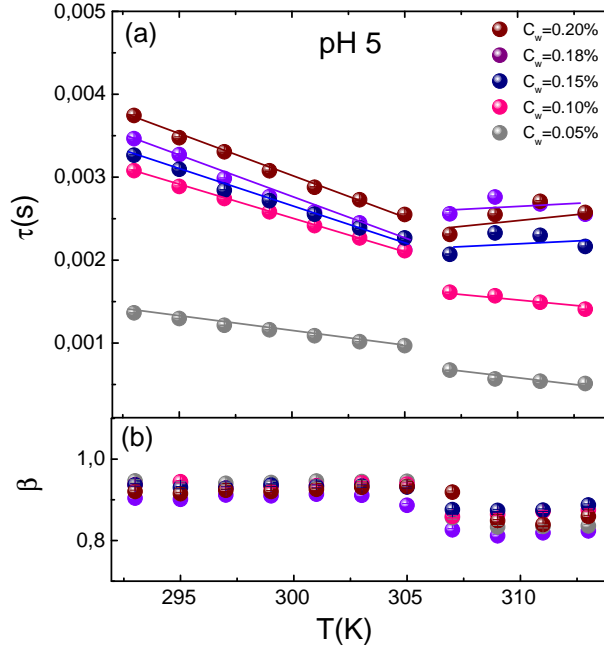


**Figure 3.14:** (a) Relaxation times and (b) stretching parameter from Eq.(2.34) for aqueous suspensions of deprotonated IPN microgels as a function of temperature at pH 5 for the indicated concentrations. Full lines in (a) are guides for eyes.

to the interaction of PAAc with water molecules. Indeed at acidic pH the PAAc chains are not effectively solvated by water and the formation of H-bonds between PAAc and PNIPAM is favored. On the contrary above pH 5 the deprotonation of the PAAc carboxylic groups ( $\text{COOH}^-$ ) results in their effective hydration and H-bonds between PAAc and water molecules are favored. Therefore at neutral pH the two networks are independent: the PNIPAM network is not constrained by the PAAc one and the sharpness of the swelling behavior of the IPN microgel resembles that of pure PNIPAM microgel, although its swelling capability is reduced. After this observation, an IPN microgel with deprotonated carboxylic groups has been synthesized. Indeed by removing a proton  $H^+$  from the carboxylic groups of PAAc through slightly changes in the synthesis procedure, such as the pH conditions, an increase of the PAAc solubility is brought about. As a result PNIPAM and PAAc networks are almost fully independent yet at acidic pH and the sharp transition exhibited by PNIPAM microgels (see Fig.3.5) is expected to be partially restored.

In Fig.3.14 the relaxation time behavior at five low weight concentrations, namely  $C_w=0.05\%$ ,  $C_w=0.10\%$ ,  $C_w=0.15\%$ ,  $C_w=0.18\%$ ,  $C_w=0.20\%$ , and at acidic pH, is shown. All samples exhibit a decrease in the relaxation time as temperature is increased, due to the progressive shrinking of the particles along the VPT at  $T \approx 305$  K. This temperature and concentration behavior is similar to that of previous samples at pH 7 (Fig.3.9), although the transition is less marked.

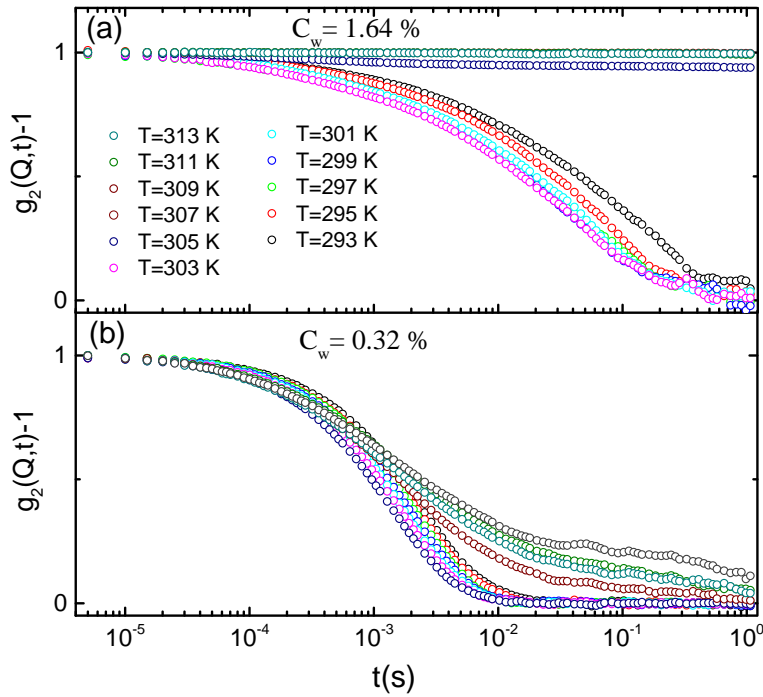


**Figure 3.15:** Normalized intensity autocorrelation curves at pH 5 for the indicated temperatures for (a)  $C_w=1.64$  % and (b)  $C_w=0.32$  %.

On the other hand the stretching coefficient  $\beta$  is always slightly below 1, with a slight decrease above the VPT.

At higher concentrations an additional feature comes out. Indeed, as shown in Fig.3.15, at concentrations  $C_w \geq 0.32$  %, a transition from a complete (below the VPT) to an incomplete (above the VPT) decay of the autocorrelation functions is observed, corresponding to an ergodic to non-ergodic transition in the investigated temporal window. This permits to individuate a transition from a fluid to an arrested state across the VPT by increasing concentration. Our DLS measurements do not allow to evaluate the relaxation time at high concentrations above the VPT and in the high-temperature regime we have turned to a qualitative description via visual inspection.

In Fig.3.16 the comparison of temperature behavior of the relaxation time and the stretching coefficient at pH 5 for deprotonated samples at  $C_w=0.32$  %,  $C_w=0.55$  %,  $C_w=0.86$  %,  $C_w=1.64$  % with the sample at  $C_w=0.18$  %, already discussed in Fig.3.14, is reported. Whilst the sample at  $C_w=0.18$  % is ergodic at all the temperatures and  $\tau$  can be easily derived, at higher concentrations the transition to a non-ergodic dynamics is observed above the VPT: at  $C_w=0.32$  % and  $C_w=0.55$  % the non-ergodic state is reached at  $T \approx 305$  K, whilst at  $C_w=0.86$  % and  $C_w=1.64$  % the system becomes non-ergodic at  $T \approx 303$  K, with a shift backwards of the non-ergodic transition temperature by increasing concentration. A visual inspection of

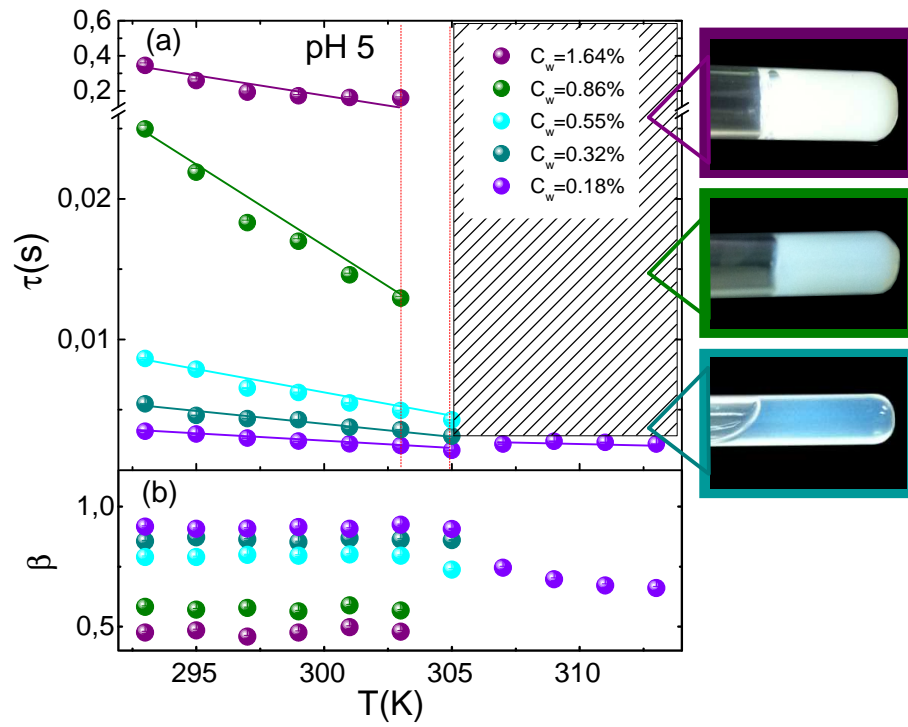


**Figure 3.16:** (a) Relaxation times and (b) stretching parameter from Eq.(2.34) for aqueous suspensions of deprotonated IPN microgels as a function of temperature at pH 5 for four "high" concentration samples  $C_w=0.32$  %,  $C_w=0.55$  %,  $C_w=0.86$  %,  $C_w=1.64$  % compared to the lowest concentrated sample ( $C_w=0.05$  %) investigated. Full lines in (a) are guides for eyes. Images on the right of the Figure are photographs of the indicated samples.



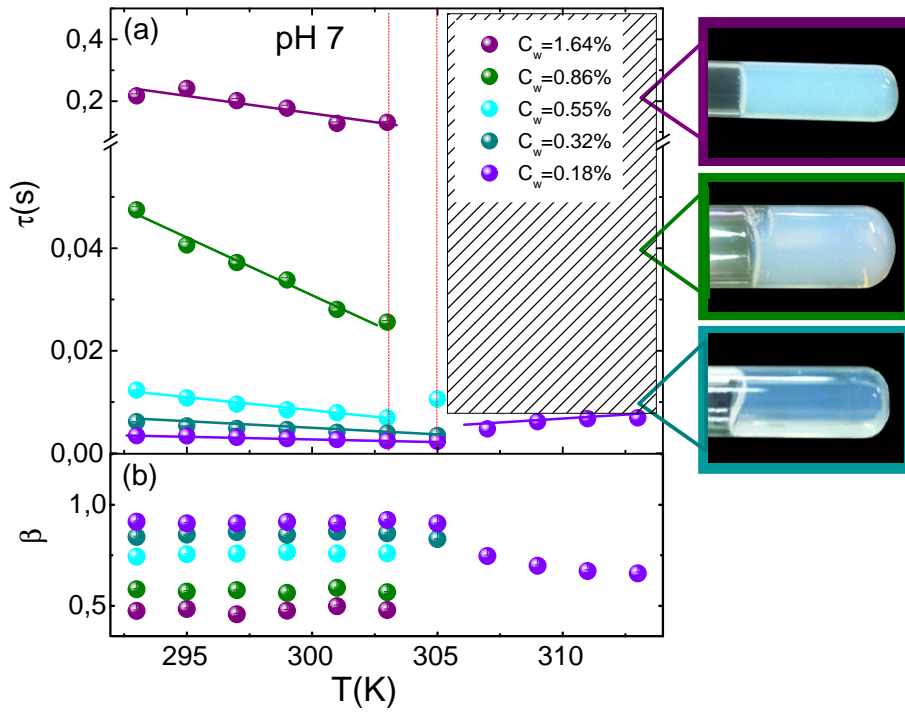


**Figure 3.17:** (a) Relaxation times and (b) stretching parameter for aqueous suspensions of deprotonated IPN microgels from Eq.(2.34) as a function of temperature at the indicated concentrations at pH 7. Full lines in (a) are guides for eyes. Images on the right of the Figure are photographs of the indicated samples.

the samples has confirmed that the viscosity increases by increasing both temperature and concentration and that the samples are completely arrested above the VPT, as shown in the photographs reported in Fig.3.16.

In Fig.3.17 the temperature behavior of the relaxation time and the stretching parameter at neutral pH and at the same concentrations as those reported in Fig.3.16, is shown. The non-ergodic state is achieved above  $T \approx 305$  K for the samples at  $C_w = 0.32\%$  and  $C_w = 0.55\%$  and above  $T \approx 303$  K for the samples at  $C_w = 0.86\%$  and  $C_w = 1.64\%$ , as in the case of pH 5. Nevertheless at pH 7 the sample at  $C_w = 0.55\%$  exhibits an increase of the relaxation time at  $T \approx 305$  K and therefore the dynamics of the system slightly changes already at this temperature. Moreover all the neutral samples are more viscous and achieve the arrested state above the VPT more abruptly than the acidic ones.

The different dynamics observed at neutral pH with respect to the acidic one, can be directly observed by comparing the intensity autocorrelation functions for samples at low concentration, namely at  $C_w = 0.18\%$ , at both acidic and neutral pH (Fig.3.18). Although these are stretched at both pH, as evidenced by the temperature behavior of the stretching parameter (Fig.3.16(b) and Fig.3.17(b)), a

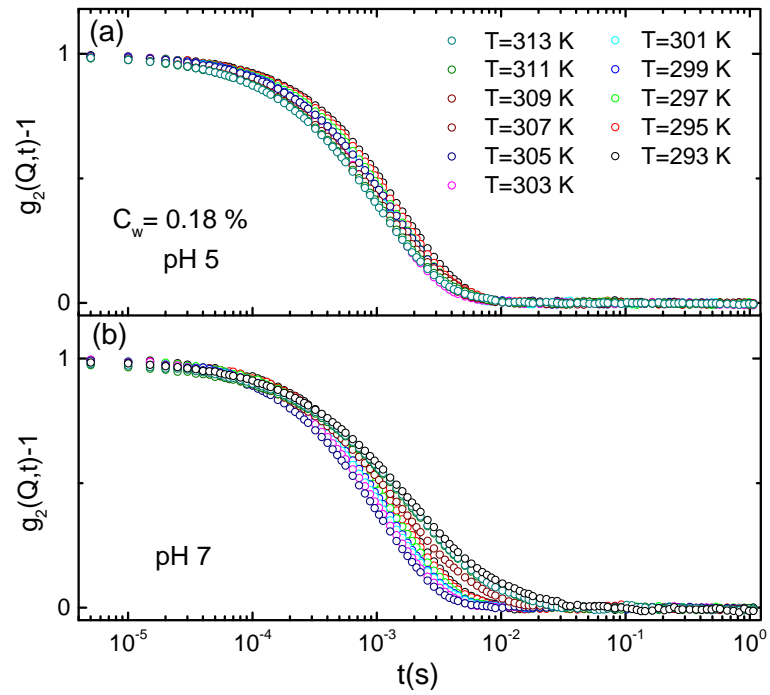


**Figure 3.18:** Normalized intensity autocorrelation curves as a function of temperature in the range  $T=(293 \div 313)$  K for an aqueous suspension of IPN microgels at  $C_w=0.18 \%$  and at (a) pH 5 and (b) pH 7.

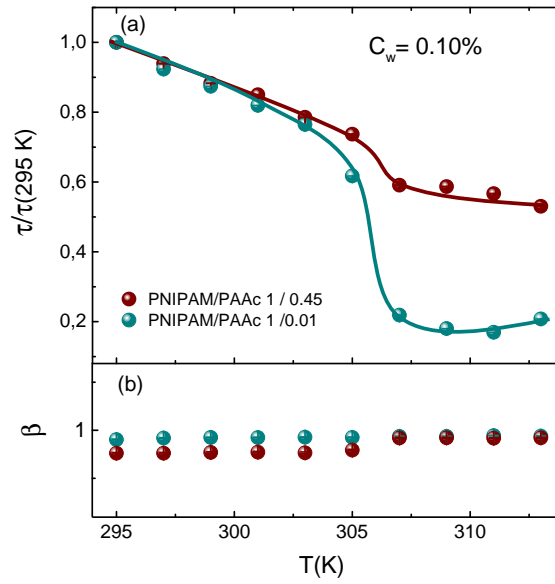


**Figure 3.19:** Comparison between (a) normalized relaxation time and (b) stretching parameter at same concentration  $C_w=0.10$  % and pH 7, for IPN microgel suspensions with different PAAc concentration, PNIPAM / PAAc = 1/0.45 and PNIPAM / PAAc = 1/0.1, respectively. Full lines are guide for eyes.

significant change of the curves and a slower dynamics is observed for pH 7 respect to pH 5.

Therefore the IPN microgel transition towards an arrested state can be controlled not only through temperature and concentration, but also by changing the pH of the solution.

## Tunability of the IPN microgel behavior

The results discussed until now clearly demonstrate that the interpenetration of the PNIPAM network with the PAAc one, leads to a more exotic phase behavior with respect to pure PNIPAM microgels, due to the possibility of tuning the swelling/shrinking transition by changing the pH of the solution, besides concentration and temperature. Therefore the role played by PAAc in the IPN microgel behavior is crucial and its swelling capability will be strongly dependent on both the synthesis procedure and the PAAc concentration.

A preliminary investigation as a function of the content of PAAc has been performed on samples with different PNIPAM/PAAc ratio. In Fig.3.19 the normalized relaxation time and stretching parameter for two samples with a PNIPAM/PAAc ratio of 1/0.45 and 1/0.1 are reported. By increasing the PAAc concentration

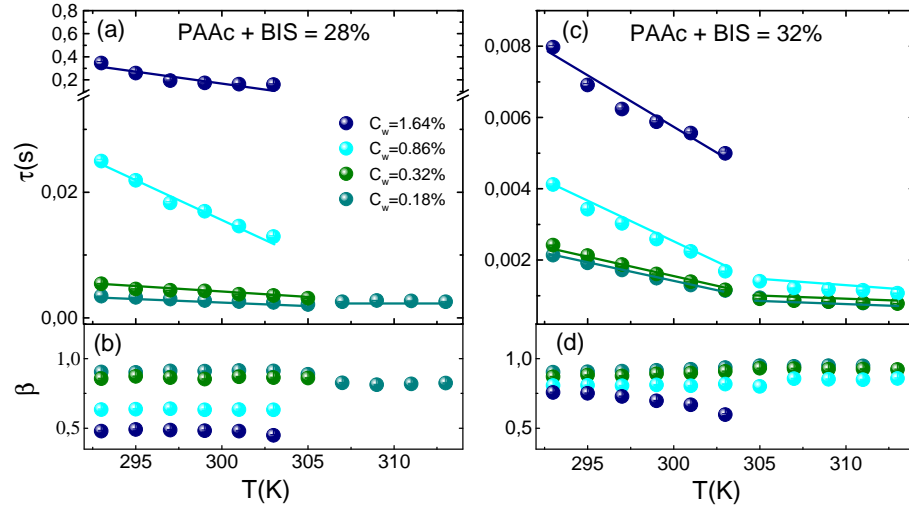


**Figure 3.20:** Relaxation time (a,c) and stretching parameter (b,d) for samples with percentage of PAAc+BIS in IPN microgels of 28 % (right panel) and 32 % (left panel) as a function of temperature, at the indicated weight concentrations and fixed pH 5. Full lines are guides for eyes.

the swelling capability of the IPN microgel is widely reduced, therefore samples with a low PAAc concentration behaves similarly to pure PNIPAM microgels, although with less remarkable transition from the swollen to the shrunken state that is highly reduced as the PNIPAM/PAAc ratio increases. This is confirmed by the temperature behavior of the stretching coefficient. Indeed in samples with low PAAc concentration,  $\beta$  exhibits values around 1, both below and above the transition, resembling the simple exponential decay in the intensity autocorrelation functions usually observed in pure PNIPAM microgels. On the contrary the sample with the highest PAAc concentration, shows a temperature behavior of  $\beta$  encompassing from values slightly below 1 to values around 1 across the VPT, thus indicating a transition from a slightly stretched behavior to a simple exponential decay of the intensity autocorrelation functions.

Beside the influence of PAAc on the swelling behavior, an additional important role is played by the cross-linker concentration. With this aim samples with different concentration of the cross-linker (BIS) have been investigated in the usual range of temperature ( $T=(293 \div 313)$  K). In particular in Fig.3.20 the temperature behavior of the relaxation time and the stretching parameter at four weight concentrations ( $C_w=0.18\%$ ,  $C_w=0.32\%$ ,  $C_w=0.86\%$  and  $C_w=1.64\%$ ), is reported for samples with 28 % and 32 % of PAAc+BIS in IPN microgel, obtained by fixing the percentage of PAAc/IPN around 20 % and by varying the BIS concentration. The concentration dependence of the relaxation time and the transition temperature remains almost unchanged, indicating that the thermodynamics, i.e. the interac-

tion between PNIPAM chains and solvent, which determine the shrinking behavior, are not affected. Nevertheless the relaxation time values are much higher for the sample with lower BIS concentration, indicating a slowing down of the dynamics for poorly cross-linked microgels. Indeed, as expected, the presence of cross-linkers limits the swelling capability of the microgel particles and the swelling ratio (i.e. the particle diameter at the reference state below the VPTT divided by the particle diameter at a given state above the VPTT (Eq.(1.8)) decreases with increasing amount of BIS, as a result of topological constraints introduced into the polymer network through an increasing number of cross-linking points. Furthermore the ergodic to non-ergodic transition occurs earlier at lower BIS concentration, suggesting that the introduction of constraints due to the cross-linker, affects the swelling behavior and as a consequence the transition to the arrested state. Indeed while at low cross-linker concentration the sample at  $C_w=0.32$  %, is already non-ergodic for DLS above the VPT, at higher cross-linker concentration this occurs for samples above  $C_w=0.86$  %. On the other hand similar changes are exhibited also by the stretching parameter (lower panels of Fig.3.20), which is lower than 1 in both the cases, but shows a more evident dependence on concentration in the case of low BIS concentration.

From these results we can observe that at high cross-linker concentration the relaxation time is generally lower, due to the topological constraints introduced by cross-linking points. PNIPAM chains are indeed limited in their swelling capability by the introduction of both the PAAc network and of the cross-linker. The swelling transition results therefore from the competition of four different contributions: the weight concentration of the solution, the PAAc concentration, the pH of the solution and finally the cross-linker percentage in pure IPN microgel suspensions.

### 3.1.4 IPN and Deprotonated IPN microgel suspensions in $D_2O$ solvent

The swelling behavior of  $D_2O$  suspensions of IPN microgel particles has been characterized in the same temperature range  $293\text{ K} \leq T \leq 313\text{ K}$  as in  $H_2O$  through DLS. The aim of this work is to investigate the role of the solvent ( $D_2O$  with respect to  $H_2O$ ), and therefore of the hydrogen bonding on the swelling behavior of IPN microgels. Moreover these DLS measurements are preliminary to the Neutron Scattering ones, since they require H/D isotopic substitution to get more contrast, and allow a direct comparison between dynamics and structure on the same samples.

Therefore measurements as a function of temperature, pH and concentration have been performed on samples with the same chemical composition as those shown in Fig.3.8 and Fig.3.9. Diluted suspensions at four low weight concentrations, namely  $C_w=0.10$  %,  $C_w=0.15$  %,  $C_w=0.20$  %,  $C_w=0.32$  %, have been

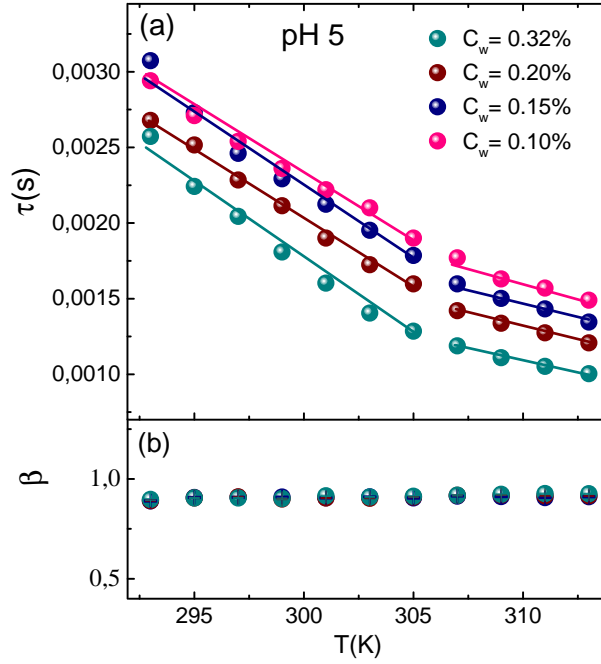


**Figure 3.21:** (a) Relaxation time and (b) stretching parameter from Eq.(2.34) as a function of temperature for deuterated suspensions of IPN microgels at the indicated concentrations and at pH 5. Full lines in (a) and (c) are guides for eyes.

prepared in order to neglect interparticle interactions and avoid phase separation.

The dynamical transition associated to the VPT from a swollen to a shrunken state is evidenced by looking at the temperature dependence of the relaxation time in  $D_2O$  at pH 5 and pH 7, as reported in Fig.3.21 and in Fig.3.22, respectively. The main features of the swelling behavior typical of samples in  $H_2O$  are preserved: the relaxation time decreases as temperature increases with a sharper transition at pH 7 with respect to pH 5, confirming that the presence of PAAc also affects the dynamics in  $D_2O$ . In particular, at pH 5 the decrease in the relaxation time exhibits the same behavior observed in  $H_2O$  (comparison between Fig.3.21 and Fig.3.8), with an almost continuous transition and a change in the slope at  $T=305$  K. Nevertheless a shift of the VPT at higher temperature ( $T=305$  K) is observed with respect to  $H_2O$  ( $T=303$  K). At pH 7 (comparison between Fig.3.22 and Fig.3.9), where the H-bonds interactions between the carboxylic groups of PAAc and water are limited, the VPT in  $D_2O$  occurs at the same temperature as in  $H_2O$ , and the sharpness of the transition is restored.

However, an interesting difference between  $D_2O$  and  $H_2O$  samples is observed: at both pH 5 and pH 7 the relaxation times are higher in  $D_2O$  than in  $H_2O$ , as shown by comparing Fig.3.21 and Fig.3.22 with Fig.3.8 and Fig.3.9, indicating a slowing down of the dynamics in  $D_2O$ , mainly arising from the higher viscosity

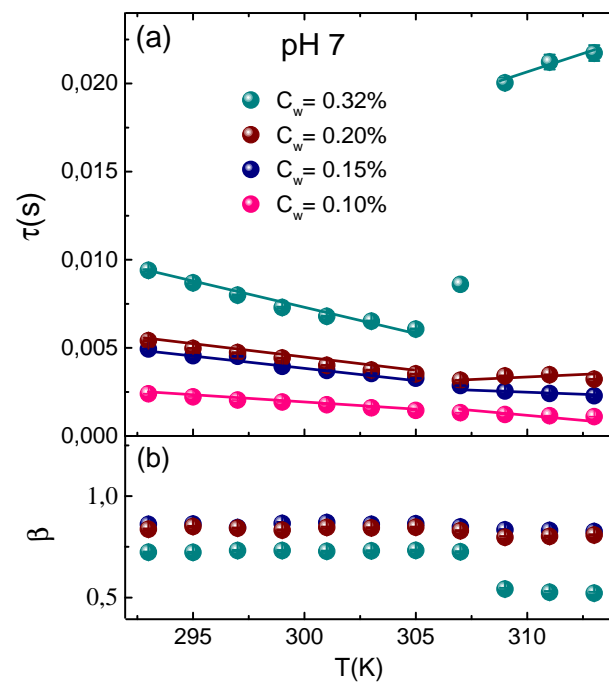


**Figure 3.22:** (a) Relaxation times and (b) stretching parameter from Eq.(2.34) as a function of temperature for deuterated suspensions of IPN microgels at the indicated concentrations and pH 7. Full lines in (a) and (c) are guides for eyes.

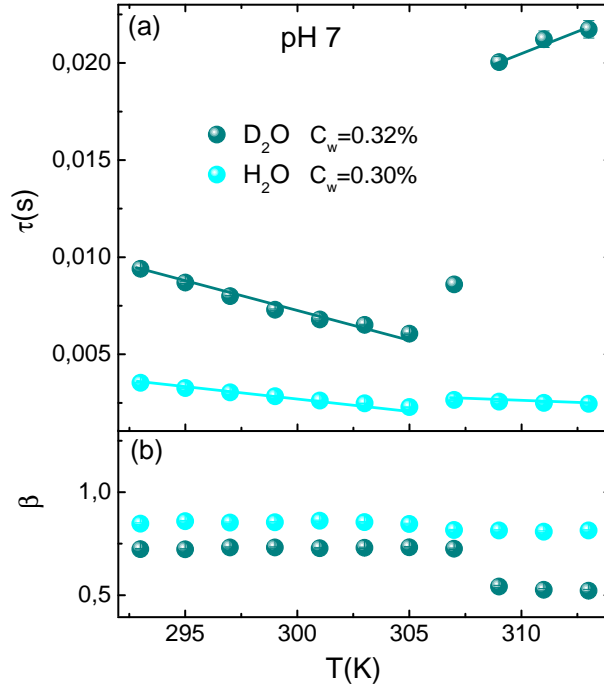


**Figure 3.23:** Comparison between (a) relaxation time and (b) stretching parameter at neutral pH as a function of temperature both for  $D_2O$  and  $H_2O$  suspensions of IPN microgels respectively at concentration  $C_w = 0.32\%$  and  $C_w = 0.30\%$ . A more evident jump above the VPTT occurs in the deuterated samples. Full lines in (a) and (b) are guides for eyes.

of  $D_2O$  than of  $H_2O$ . Nevertheless even if the weight concentrations of  $D_2O$  and  $H_2O$  samples are very close, the differences between their effective packing fractions may be significant. Thus explaining their different behaviors only as a result of the different  $D_2O$  and  $H_2O$  viscosity, may be slightly misleading and estimating their effective packing fractions will be crucial for further investigations. Moreover at pH 7 an additional feature comes out: in  $D_2O$  a faster decreasing of  $\tau$  is observed until the transition is approached at  $T = 307$  K, thereafter the relaxation time jumps to higher values both in  $D_2O$  and  $H_2O$ , but a more evident gap is observed in the  $D_2O$  samples at  $C_w = 0.32\%$  (Fig.3.23). Correspondingly the stretching coefficient decreases above the transition, up to values close to 0.5. This stretched behavior above  $T = 307$  K is evidenced in the normalized autocorrelation functions reported in Fig.3.24, in the usual range of temperature ( $T = (293 \div 313)$  K) for the deuterated suspensions of IPN microgels at  $C_w = 0.32\%$  and pH 7.

Despite of these differences, the concentration dependence of the relaxation time in  $D_2O$  at pH 5 and pH 7, as shown in Fig.3.25, confirms the behavior observed in  $H_2O$ : at pH 5 the lowest values of the relaxation time correspond to the highest concentrated sample, whilst at pH 7 an opposite trend is observed.



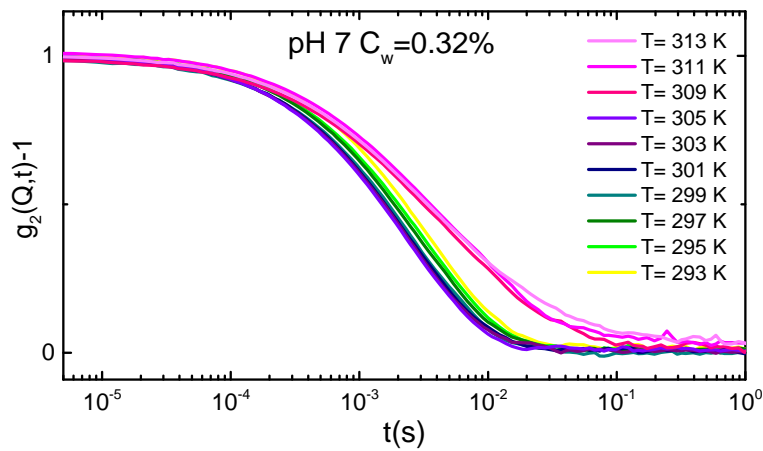


**Figure 3.24:** Normalized autocorrelation function for the deuterated sample at the concentration  $C_w=0.30\%$  and pH 7 as temperature is changed in a range between 295 K and 313 K.

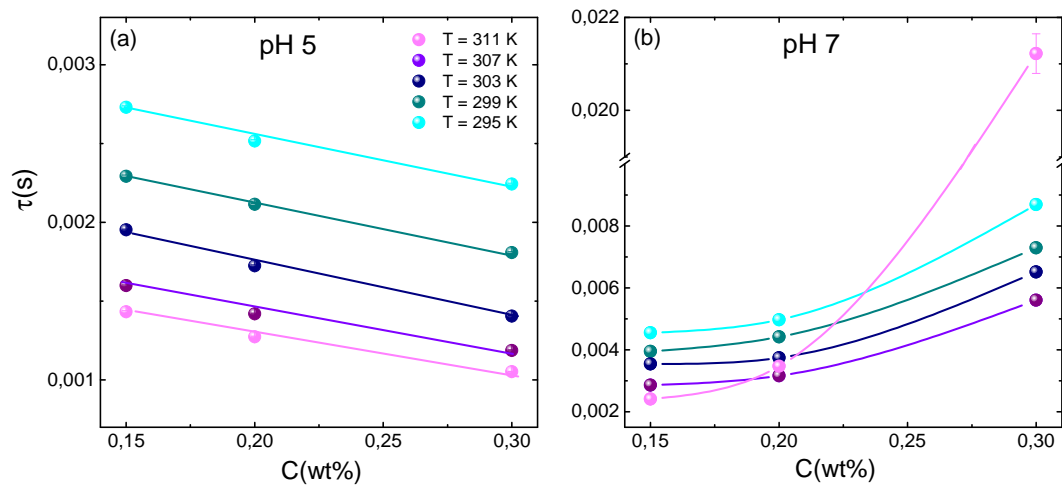


**Figure 3.25:** Relaxation times as a function of the weight concentration at five fixed temperature values at (a) pH 5 and (b) pH 7. Full lines in (a) and (c) are guides for eyes.

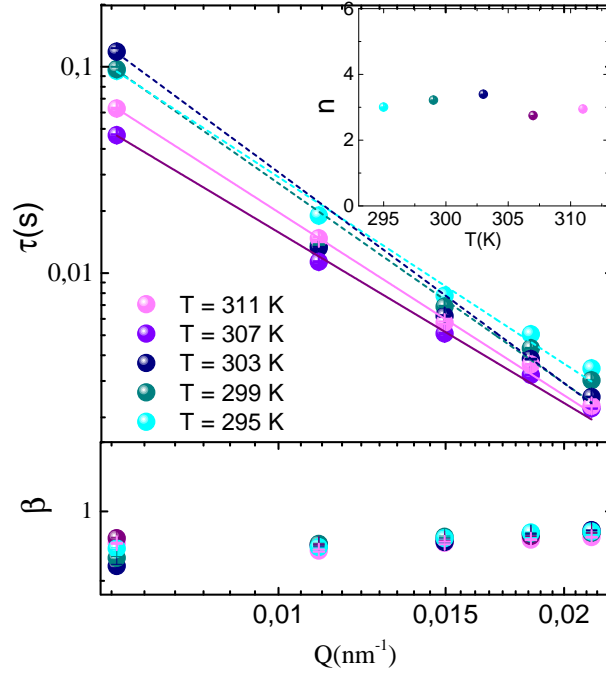


**Figure 3.26:** (a) Relaxation time and (b) stretching parameter as a function of exchanged wave-vector  $Q$  at  $C_w=0.10$  %, pH 7 for the indicated temperatures. Full lines are fits at temperature above the transition through Eq.(3.1) with  $n=2.94\pm0.03$  ( $T=311$  K),  $n=2.749\pm0.002$  ( $T=307$  K), whilst dashed lines are fits at temperature below the transition through Eq.(3.1) with  $n=3.395\pm0.007$  ( $T=303$  K),  $n=3.217\pm0.006$  ( $T=299$  K),  $n=3.004\pm0.003$  ( $T=295$  K). Inset: behavior of the exponent  $n$  as a function of temperature at  $C_w=0.10$  % and at pH 7.

In order to obtain information about the nature of the dynamics in the case of  $D_2O$  IPN microgel suspensions, the relaxation time and the stretching parameter behaviors have been investigated at different length scales. Their behaviors as a function of the exchanged wave-vector  $Q$ , have been obtained by fitting the auto-correlation curves through the same equation used for  $H_2O$  samples (Eq.(2.34)) and they are reported in Fig.3.26 as a function of  $Q$ .

The relaxation time, reported in a double logarithmic plot, results strongly  $Q$  dependent, with the typical power law decay, as discussed in Par.3.1.2 (Eq.(3.1)). The full lines superimposed to the data in Fig.3.26(a) are the fits according to Eq.(3.1) and values of  $n$  between 3 and 4 are found, at variance with  $n$  between 2 and 3 found in light water, as experimentally observed in previous works and confirmed by our findings (Par.3.1.2). This means that by decreasing the length scale (or equivalently by increasing  $Q$ ) the relaxation time decreases faster in  $D_2O$  than in  $H_2O$  solutions. However a theoretical model explaining this behavior has not been provided, therefore these findings require further investigations which

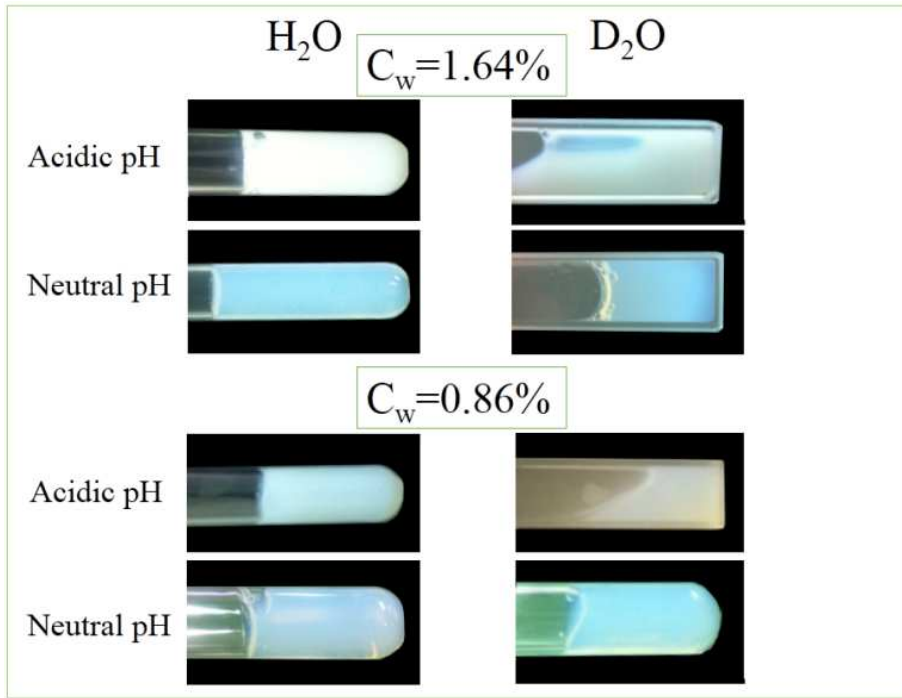


**Figure 3.27:** Photographs of samples in  $H_2O$  and  $D_2O$  solvents for two weight concentrations  $C_w = 0.86\%$  and  $C_w = 1.64\%$ , at acidic ( $pH \approx 5$ ) and neutral ( $pH \approx 7$ ) pH, above the VPT.

may open the way to a better understanding of the nature of the motion for  $D_2O$  polymer microgel suspensions. On the contrary the stretching parameter  $\beta$  reported in Fig.3.26(b), clearly shows no dependence on the wave vector  $Q$ , as already found in  $H_2O$  case.

A different dynamics in  $D_2O$  solutions is also exhibited in the IPN microgel behavior at higher concentrations for  $D_2O$  deprotonated samples. Indeed in the same range of temperature, concentration and pH as those investigated for  $H_2O$  deprotonated suspensions, the non-ergodic state in  $D_2O$  is achieved only at the highest concentrations ( $C_w = 0.86\%$  and  $C_w = 1.64\%$ ) and at neutral pH, as shown in the photographs reported in Fig.3.27. All the other samples exhibit an increasing viscosity above the VPT by increasing concentration and pH, but they do not achieve an arrested state.

Our results suggest that hydrogen-bonds play a crucial role in the polymer-solvent interactions and that the swelling kinetics can be slightly affected by  $D_2O$ . In this case, indeed, stronger H-bondings occur between polymer and solvent with respect to the case of  $H_2O$ , hence changes are expected in the rate of the swelling/shrinking transition (86). On the other hand our results highlight that the H/D isotope substitution affects inter-particle interactions, and thus non-ergodic

---

transition, in a not trivial way which needs further investigations. Nevertheless in  $D_2O$  solvent the main features of the swelling behavior are preserved, thus neutron scattering can be usefully performed to obtain information on the intra-particle structural response to changes of temperature, pH and concentration.

## 3.2 Local Structure: Small-Angle Neutron Scattering

A systematic investigation of the intra-particle structural behavior across the VPT for  $D_2O$  suspensions of PNIPAM-PAAc IPN microgels in the high dilution regime, has been performed through Small-Angle Neutron Scattering on SANS2d at the ISIS neutron spallation source. Additional beamtime on the Larmor instrument at the same neutron source, has provided further details on the local structure of  $D_2O$  suspensions of both pure PNIPAM and highly concentrated IPN microgels, confirming our previous results and opening the way to further investigations.

In literature different models have been proposed to rationalize the reorganization of the polymer structure when cross-linkers are introduced into polymer solution to obtain polymer gels. Nevertheless most of the experimental and theoretical works are focused on the behavior of the large-scale inhomogeneities by approaching gelation. In particular a lattice model of blobs with mesh size  $\xi$  has been introduced to describe the gelation process in term of blobs percolation. The same model can be applied to describe the formation of microgels and thus to represent their intra-particle local structural behavior across the VPT.

In this chapter the results obtained through SANS measurements are presented to provide a clear picture of the intra-particle local structural behavior in response to changes of temperature, pH and concentration. Moreover a preliminary investigation of the low dilution regime is presented, highlighting the occurrence of a more complex behavior at high concentration which needs further investigation.

### 3.2.1 PNIPAM microgel suspensions in $D_2O$ solvent

The temperature behavior of the local structure of  $D_2O$  suspensions of PNIPAM microgels at fixed low concentration ( $C_w=0.30\%$ ), has been investigated through Small-Angle Neutron Scattering. The scattering geometry of the Larmor beamline at ISIS neutron spallation source allows to investigate the  $Q$ -range from 0.004 to  $0.7\text{ \AA}^{-1}$ , thus providing information about the structural inhomogeneities in the range 10-1600  $\text{\AA}$ . Due to the typical size of our PNIPAM microgel particles, these measurements allow to explore structural changes during the cross-over from the fully swollen to the completely shrunken phase, as previously observed (66, 67, 108).

In Fig.3.28 the temperature behavior of the spectra collected at  $C_w=0.30\%$  is reported, once the instrumental effects have been removed by subtraction of the empty cell contribution, normalization to the transmitted beam and subtraction of the incoherent background, as extensively explained in Par.2.2.2. As the temperature increases, the spectral shape clearly changes at both low and intermediate  $Q$  values, suggesting a significant response of the microgel particle structure at

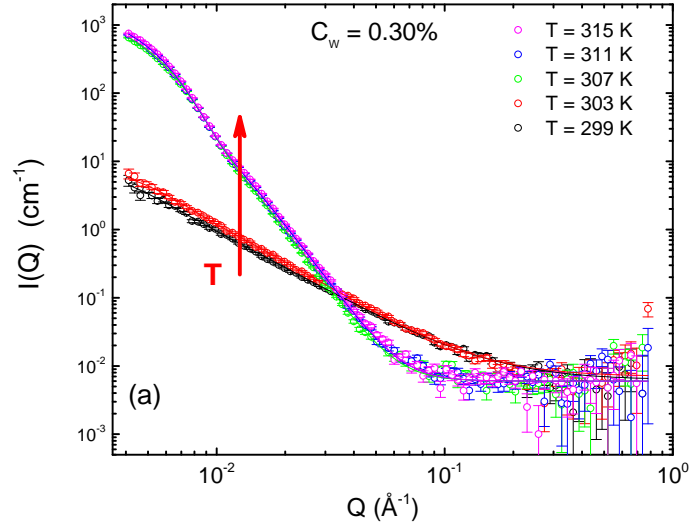


**Figure 3.28:** Differential cross-section for  $D_2O$  suspensions of PNIPAM microgels at  $C_w=0.30\%$  in the temperature range  $T=(299 \div 313)$  K: experimental data are reported as circles, their fits as solid lines. The arrow indicates increasing temperature.

different length scales. In particular a sharp transition is observed around 305 K, suggesting that the swelling/shrinking behavior of the microgel particles at larger length scales is well reflected by the changes in the local structure.

Preliminary details on the system can be obtained through the traditional Porod-Guinier analysis. In this way the low- $Q$  (Guinier) and high- $Q$  (Porod) regions are well separated and information on different length scales are obtained. Nevertheless this analysis may lead to misleading results, being these two contributions strictly related in the case of polymer microgels. Indeed when cross-linkers are employed to synthesize elastic polymer microgels, the polymer chains in solution become connected one to each other. The resulting inhomogeneous structure leads to non uniform distribution and concentration of the polymer chains, which affect the structural behavior at both small and large length scales (or equivalently at high and low  $Q$  regions). Thus, a more reliable analysis has been obtained by modeling the microgel network through a deformable lattice model of blobs. Its behavior is described in terms of a short correlation length,  $\xi$ , which accounts for the rapid fluctuations of the position of the polymer chains, and a long correlation one,  $R_g$ , associated to those regions of the microgel network with higher polymer density and slower dynamics, as extensively explained in Par.2.2.2.

In Fig.3.29 the temperature behavior of the correlation length  $\xi$  and the Porod exponent  $D$ , which provides details about the roughness of the domain interfaces, as obtained from the Lorentzian term of Eq.(2.84) for a  $D_2O$  suspension of PNIPAM microgels at  $C_w=0.30\%$ , is reported. For the correlation length (Fig.3.29(a))

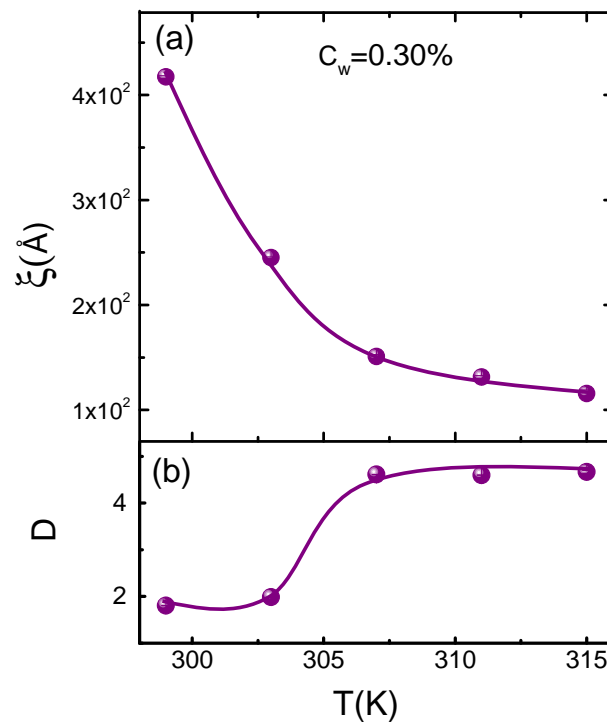


**Figure 3.29:** (a) Correlation length,  $\xi$ , and (b) Porod exponent,  $D$ , for  $D_2O$  suspensions of PNIPAM microgels as a function of temperature at fixed concentration  $C_w=0.30\%$ . Full lines are guides for eyes.

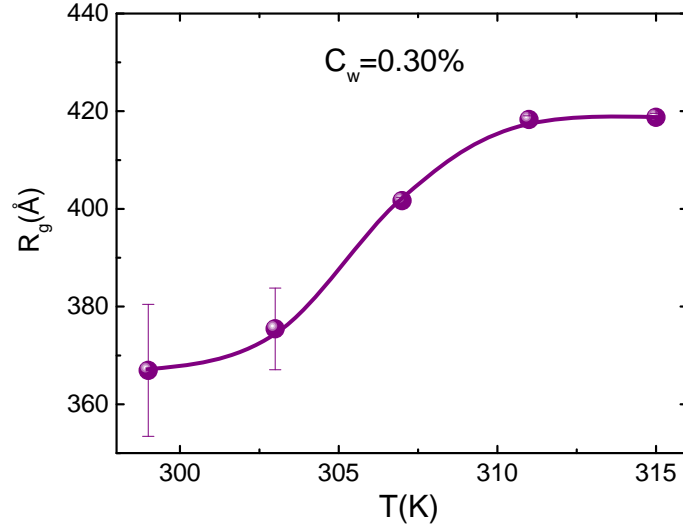


**Figure 3.30:** Gyration radius of the static inhomogeneities for  $D_2O$  suspensions of PNIPAM microgels as a function of temperature at fixed concentration  $C_w=0.30\%$  for  $D_2O$  suspensions of PNIPAM microgels. Full lines are guides for eyes.

a decrease with temperature and a sharp transition to a plateau value above  $T \approx 305$  K is observed. On the other hand a sharp transition of the Porod exponent  $D$  (Fig.3.29(b)), from values around 2 to values around 4, is observed around 305 K.

The presence of cross-links leads to regions with restricted dynamics and higher polymer density well distinguishable when the network is completely swollen. The mean size  $R_g$  of such regions of the lattice is obtained from the Gaussian term of Eq.(2.84) and its temperature behavior is shown in Fig.3.30. The increase with temperature of  $R_g$  suggests a transition from an inhomogeneous to a porous solid-like structure, when the microgel particles undergo a transition from a swollen to a shrunken state. Indeed the shrinking of the polymer chains gives rise to a larger sized cluster of junction points where contrast between polymer-rich and polymer-poor domains is widely reduced.

These results highlight the occurrence of a structural transition within the PNIPAM microgels which corresponds to the volume-phase transition at larger length scales. This preliminary investigation provides useful details on the temperature behavior of the local structure of PNIPAM microgels, thus clarifying some of the aspects for  $D_2O$  suspensions of PNIPAM-PAAc IPN microgels.

In the following the results obtained on IPN microgels are presented, together with an extensive explanation of the model that the investigation of their local structure investigation has provided.



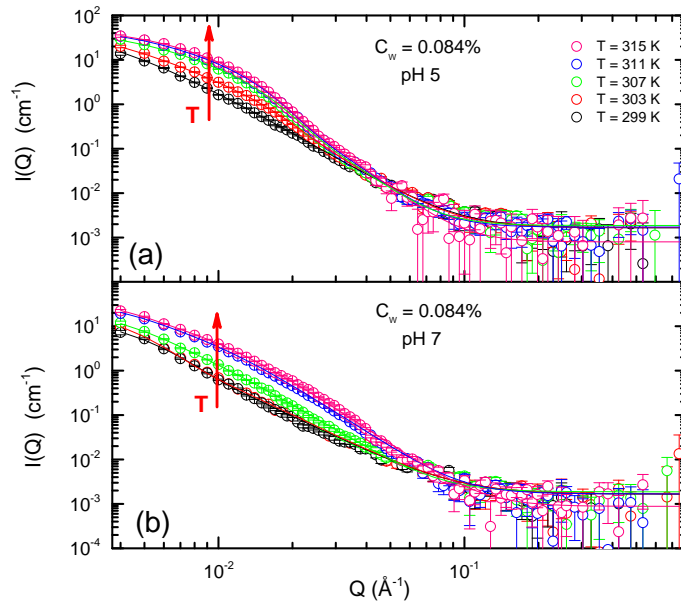


**Figure 3.31:** Differential cross-section for  $D_2O$  suspensions of IPN microgels at  $C_w=0.084\%$  samples at (a) pH 5 and (b) pH 7 in the temperature range  $T=(299 \div 315)$  K: experimental data are reported as circles, their fits as solid lines. The arrows indicate increasing temperature.

### 3.2.2 IPN microgel suspensions in $D_2O$ solvent

The local structure of the IPN microgel particles has been investigated as a function of temperature, pH and concentration through Small-Angle Neutron Scattering, as discussed in Par.2.2.2. Indeed since the average hydrodynamic diameter of the investigated microgel particles is in the range 2000-5000 Å, our measurements on the SANS2d instrument, in the  $Q$ -range from 0.004 to 0.7 Å<sup>-1</sup>, allow to look inside them and to explore changes of their local structure during the cross-over from the fully swollen to the completely shrunken phase, as similarly observed on PNIPAM microgel suspensions (66, 67, 108) and confirmed by our measurements (Par.3.2.1). The results obtained on these IPN microgel samples have been published in The Journal of Chemical Physics (109).

In Fig.3.31 the temperature behavior of the spectra collected at  $C_w=0.084\%$  at pH 5 and pH 7, as obtained after removing the instrumental effects, is reported, as an example. As the temperature or the pH varies, the spectral shape clearly changes at both low and intermediate  $Q$  values. As observed for PNIPAM microgel suspensions, also in this case a significant response of the microgel particle structure occurs at different length scales and the decomposition of the scattering intensity into two contribution is crucial: the excess static scattering at low  $Q$  values is associated to densely crosslinked regions, while the scattering at higher

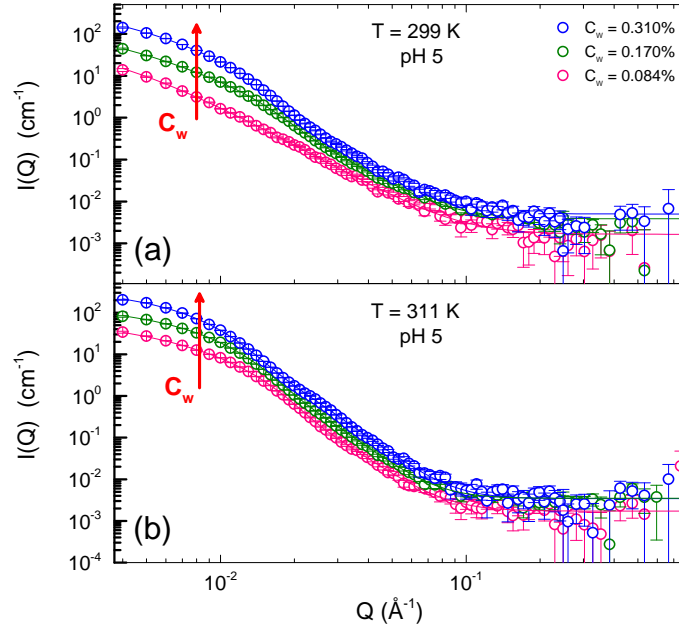


**Figure 3.32:** Differential cross-section for  $D_2O$  suspensions of IPN microgels at pH 5 and two values of temperature below and above the VPT, namely (a)  $T=299$  K and (b)  $T=311$  K, for three different concentrations  $C_w=0.084\%$ ,  $0.170\%$ ,  $0.310\%$ . Experimental data are reported as circles, their fits as solid lines. The arrows indicate increasing concentration.

$Q$  is dominated by the contribution of the surrounding swollen matrix with a solution-like behavior.

According to PNIPAM microgels, the lineshape of  $I(Q)$  for these samples may be described by Eq.(2.84), extensively discussed in Par.2.2.2. We notice that, with increasing temperature, an increase of the intensity at very low  $Q$ ,  $I_L(0) + I_G(0)$ , and of the slope,  $D$ , at higher  $Q$  values is observed also in PNIPAM-PAAc IPN microgel suspensions. The increase of the neutron contrast/scattering intensity is due to the collapse of the polymer chains above the VPT, which leads to a more homogeneous local structure within the microgel particles, and consistently the increase of the Porod exponent  $D$  is due to the decrease of roughness of the domain interfaces.

As for DLS experiments, we notice that the role played by PAAc in modulating the response of the local structure determines interesting differences between acidic and neutral conditions, as it is evident from Fig.3.31. Samples at pH 5 exhibit a continuous variation of the low  $Q$  intensity, suggesting a smooth macroscopic transition from a swollen to a shrunken state at temperatures around 305 K. On the contrary, the transition becomes more evident at neutral pH. This behavior is related to the solvation in water of the PAAc chains at pH values above 5, due

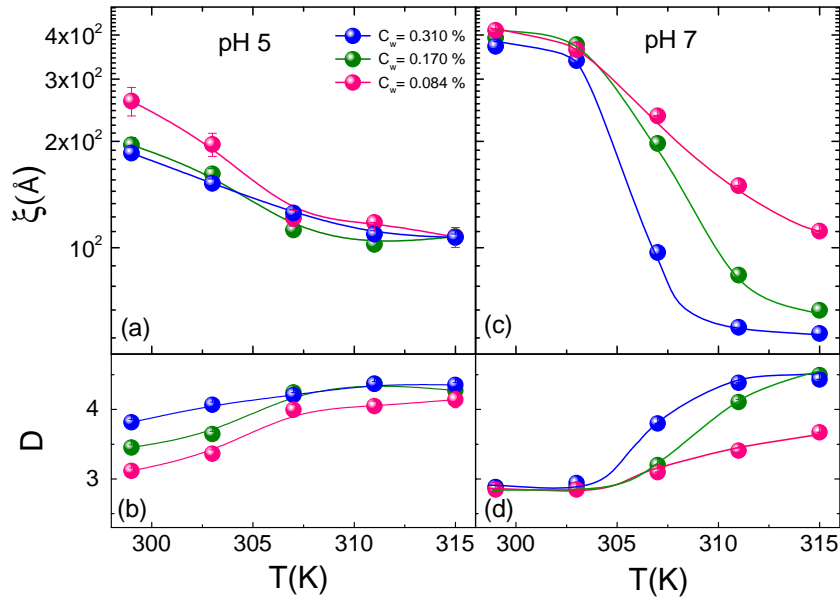


**Figure 3.33:** Correlation length,  $\xi$ , and Porod exponent,  $D$ , for  $D_2O$  suspensions of IPN microgels as a function of temperature for three fixed concentrations  $C_w=0.084\%$ ,  $0.170\%$ ,  $0.310\%$  and two pH values, namely pH 5, panels (a) and (b), and pH 7, panels (c) and (d). Full lines are guides for eyes.

to its deprotonation, with a complete regain of independence between PNIPAM and PAAc networks. Also the changes of  $D$  observed at higher  $Q$  values are more pronounced at pH 7, reflecting a macroscopic transition from states characterized by different structural features.

In addition we notice a concentration dependence of the microgel particles structural response, both above and below the VPT (see Fig.3.32). Indeed, both the low  $Q$  intensity and the slope,  $D$ , of the differential cross section at higher  $Q$  increases with concentration at fixed pH and temperature. How much these quantities change with the concentration is probably tuned by the pH, as we will comment later.

As for PNIPAM microgel suspensions the local intra-particle structural response to external parameters has been rationalized by looking at the behavior of the correlation length  $\xi$  and the Porod exponent  $D$ , obtained from the Lorentzian contribution of Eq.(2.84). Their behavior, reported in Fig.3.33 as a function of temperature at both acidic and neutral pH, for three different concentrations, highlights the existence of a transition from an inhomogeneous to a porous solid-like structure across the VPT.

At pH 5 the correlation length  $\xi$  decreases with temperature, showing a transition to a plateau value above 305 K (Fig.3.33(a)). A similar, although less dramatic, change from a clear temperature dependence to an almost constant value is

observed for the Porod exponent  $D$  (Fig.3.33(b)). Moreover in this case a spread of the Porod coefficient is visible already at low temperatures and masks the transition, in particular at the highest concentration. Therefore a sharp transition at the VPT is not evidenced. Instead at pH 7 a sharper transition is identified at  $T \approx 305$  K in the behavior of both the correlation length (Fig.3.33(c)) and the Porod exponent (Fig.3.33(d)), although in this case a plateau is not reached in the investigated temperature range.

This different behavior can be explained considering that by increasing the pH above 5 the deprotonation of the PAAc chains results in their effective hydration, leading to the independent response to temperature of the PNIPAM and PAAc networks. Therefore, at neutral pH, above the VPT, the PNIPAM network collapses, while the PAAc chains do not. In detail below the VPT, where the polymer coils are completely swollen, the microgel particles have a rough domain surface ( $D \approx 3$ ), while above the VPT they switch to a homogenous solid-like structure, with smooth interfaces between different domains ( $D \approx 4$ ). Additionally, a different behavior with concentration of both the correlation length and the Porod exponent across the transition can be noticed, at the two investigated pH values. At acidic pH, both parameters for the less concentrated sample show the most intense variation with increasing temperature. On the contrary at pH 7 this trend is reversed: the most concentrated sample shows the largest variation of  $\xi$  and  $D$  across the transition and this gap decreases with concentration. This behavior suggests that the role played by the concentration is not trivial and confirms the features of the swelling behavior observed through DLS measurements at larger length scales, as discussed previously.

From the Gaussian contribution of the Eq.(2.84), one can obtain information about the mean size  $R_g$  of those regions of the lattice with restricted dynamics and higher polymer density, due to the presence of cross-links. The behavior of the parameter  $R_g$ , is shown in Fig.3.34 as a function of temperature and concentration at both pH 5 and 7. The average size of the polymer-rich domains ( $R_g$ ) increases with temperature, suggesting a transition from an inhomogeneous structure in the swollen state, to a porous solid-like structure, where a unique larger sized cluster is formed, due to the shrinking of the polymer chains.  $R_g$  increases with temperature at both acidic and neutral pH conditions, nevertheless at pH 7 an evident discontinuity shows up at  $T \approx 305$  K, around the expected VPT, thus confirming that at neutral pH the two networks are independent and the sharpness of the transition is partially restored with respect to the case of pure PNIPAM. On the contrary at pH 5 the differences between polymer-rich/polymer-poor domains are less marked and the sharpness of the elastic response of the system to temperature changes is limited by H-bonding between PNIPAM and PAAc chains. Indeed at pH 5 the PAAc chains are not effectively solvated by water and the formation of H-bonds between PAAc and PNIPAM is favored (110), thus introducing spatial constraints which limit the sharpness of the PNIPAM network swelling. At neutral pH instead

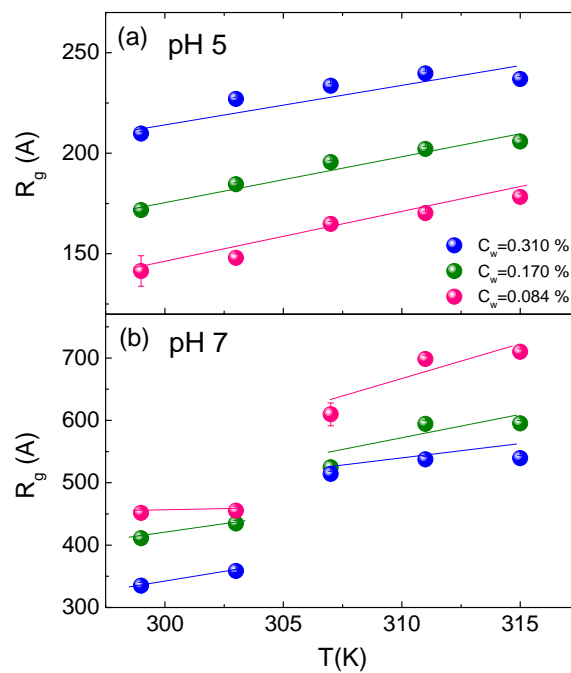


**Figure 3.34:** Gyration radius of the static inhomogeneities for  $D_2O$  suspensions of IPN microgels as a function of temperature and for three fixed concentrations  $C_w=0.084\%$ ,  $0.170\%$ ,  $0.310\%$  at acidic (a) and neutral (b) pH condition. Full lines are guides for eyes.

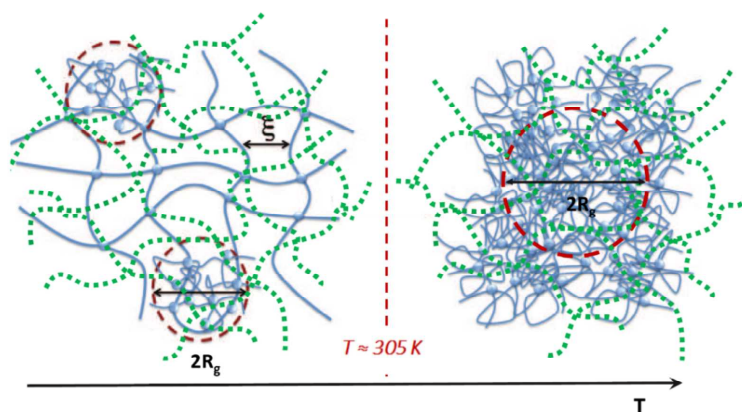


**Figure 3.35:** Cartoon of the local structure inside the IPN microgel particle below (left side) and above (right side) the VPT. The solid and dashed lines represent the two interpenetrating networks with average mesh size  $\xi$ . The dashed red circles in the left side panel (swollen state) evidence the regions of quenched inhomogeneities of average size (radius)  $R_g$ , due to the presence of cross-links. With increasing temperature, the collapse of the polymer networks induces a transition from an inhomogeneous structure to a porous solid-like structure (right side panel).

both compounds are solvated by water that mediates their interaction, giving rise to a lower number of interchain H-bonds. Therefore the H-bonds, depending on the pH, highly affect the swelling behaviour of the system. Moreover, H-bonding between the PNIPAM and PAAc chains, determines additional inhomogeneities in the structure of microgel particles with smaller size compared to the high density regions formed by crosslinking. As a consequence,  $R_g$  is the average size between two different inhomogeneity domains and at acidic pH it results smaller compared to neutral conditions (where H-bonds do not form).

We notice also that the concentration dependence is reversed at neutral and acidic pH: at neutral pH the most concentrated sample shows the lowest value of  $R_g$ , suggesting that the spatial distribution of polymer-rich (or poor) domains becomes narrower as the concentration increases. This behavior seems to confirm the concentration dependence observed by DLS measurements and deserves deeper investigation.

These results return a simple model of the internal structure of the microgel particles across the VPT, as shown in the cartoon of Fig.3.35. The IPN microgels internal structure undergoes a transition from an inhomogeneous interpenetrated network (where dense regions of size  $R_g$  are separated by a lower density network of size  $\xi$ ) to a porous solid-like structure, where the typical nanometric structure of the tridimensional network is lost, as a consequence of the macroscopic swelling/shrinking transition. When the polymer chains are completely swollen

the open network can accommodate a large amount of water, resulting in an inhomogeneous intra-particle structure of high contrast between polymer-rich and -poor regions. With increasing temperature, the collapse of the polymer chains leads to the expulsion of water molecules, along with a shrinking of the microgel particles, whose local structure becomes more homogeneous and characterized by correlation domains with smoother interfaces. As a consequence, the short correlation length,  $\xi$ , decreases when the microgel particles collapse. Instead the Porod exponent,  $D$ , associated to the roughness of the correlation domains interfaces, increases, since their surface becomes smoother as the degree of inhomogeneity within the polymer network decreases. Furthermore, the collapse of the polymer chains leads to the loss of individuality of the frozen blobs within the microgel particle which can be interpreted as an infinite cluster of cross-links points and accordingly leading to the  $R_g$  increasing.

### 3.2.3 Deprotonated IPN microgel suspensions in D<sub>2</sub>O solvent

The role played by acrylic-acid in the intra-particle structural behavior has been further investigated by looking at the local structure of deprotonated IPN microgel particles as a function of temperature, pH and concentration through Small-Angle Neutron Scattering. As for PNIPAM and IPN microgels SANS measurements allow to explore their local structural response to changes of temperature, pH and concentration across the VPT, on length scales between 10 Å and 1600 Å, due to the scattering geometry of the Larmor instrument.

The SANS spectra for deprotonated IPN microgels at  $C_w=0.30$  % have been collected at five temperatures in the range  $T=(299 \div 315)$  K and at pH 5 and 7, as reported in Fig.3.36. As observed for both PNIPAM and IPN microgels the spectral shape clearly changes with temperature at both low and intermediate  $Q$  values, indicating a structural response at different length scales. Furthermore by comparing Fig.3.36 and Fig.3.28, one can observe that the spectral shape resembles that of PNIPAM microgels, suggesting that by deprotonating the sample the independence of the PNIPAM and PAAc networks is almost restored and a sharp response of the local structure is expected.

The same scattering function  $I(Q)$  used for PNIPAM and IPN microgels, given by Eq.(2.84), has been applied to obtain details about the temperature behavior of the intra-particle structure of deprotonated IPN microgel particles. Also in this case an increase with increasing temperature of the intensity at very low  $Q$  and of the slope ( $D$ ) at higher  $Q$  values, is observed, as a result of the swelling/shrinking behavior of the polymer chains across the VPT.

As expected from DLS measurements on deprotonated IPN microgels, the role played by PAAc in modulating the response of their local structure is not trivial.

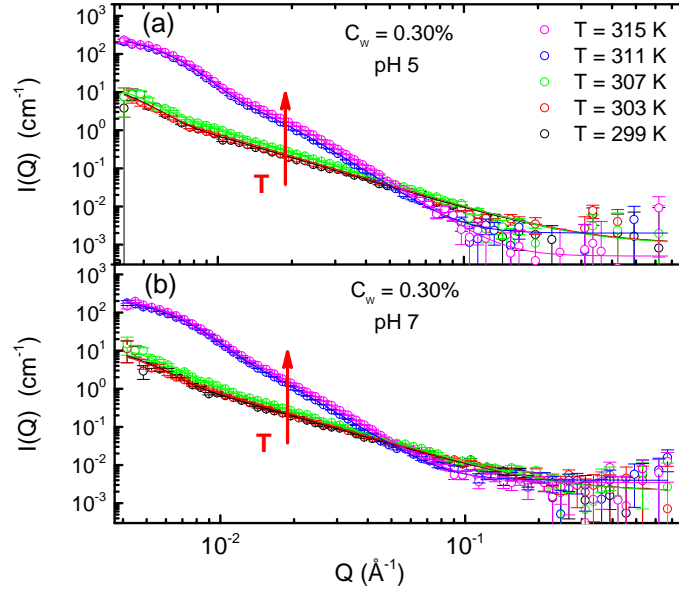


**Figure 3.36:** Differential cross-section for  $D_2O$  suspensions of deprotonated IPN microgels at  $C_w=0.30\%$ , at pH 5 and pH 7, in the temperature range  $T=(299 \div 315)$  K: experimental data are reported as circles, their fits as solid lines. The arrows indicate increasing temperature.

Indeed the SANS spectra exhibit sharp changes in all the investigated  $Q$ -range at both pH 5 and pH 7, as a result of the sharp volume-phase transition from a swollen to a shrunken state, due to the restored independence between PNIPAM and PAAc networks.

The behavior of the local structure of deprotonated IPN microgels can be rationalized by looking at the behavior of the correlation length,  $\xi$ , and the Porod exponent,  $D$ , as a function of temperature and pH, as obtained by following the same fitting procedure applied to IPN microgels. In Fig.3.37 the temperature behavior of  $\xi$  (panel (a)) and  $D$  (panel(b)) is reported at acidic and neutral pH. A decrease of the correlation length and an increase of the Porod exponent with increasing temperature is observed, as a consequence of the polymer chains shrinking, thus confirming our previous results for PNIPAM and IPN microgels. At variance with IPN microgels, in deprotonated IPN microgels a sharp transition is observed for both  $\xi$  and  $D$  at both acidic and neutral pH, thus confirming that by deprotonating the carboxylic groups of PAAc chains through the synthesis procedure, an IPN microgel with independent PNIPAM and PAAc networks is synthesized and the sharpness of the transition is restored.

As for PNIPAM and IPN microgels, the temperature behavior of the mean size  $R_g$  of high polymer dense regions with restricted dynamics, due to the presence of cross-links, can be obtained from the Gaussian contribution of the Eq.(2.84). In



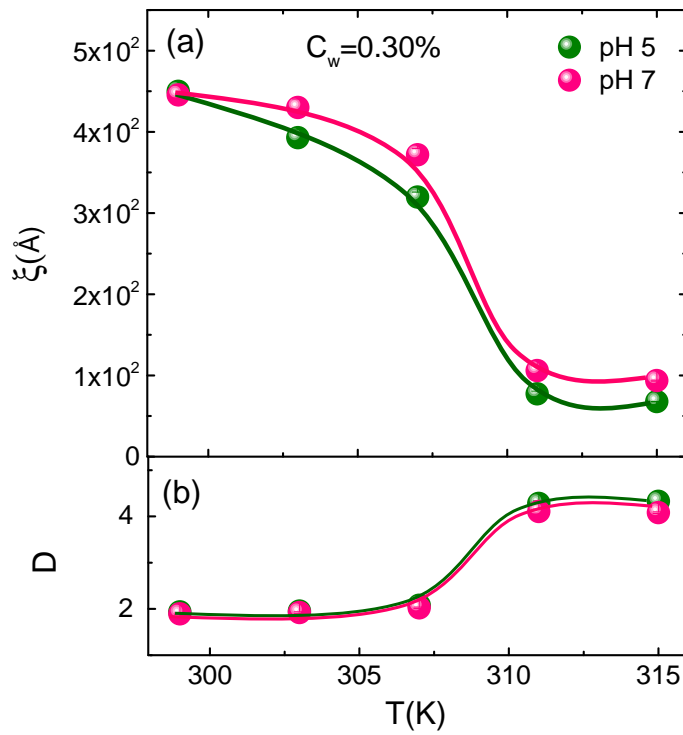


**Figure 3.37:** (a) Correlation length,  $\xi$ , and (b) Porod exponent,  $D$ , for  $D_2O$  suspensions of deprotonated IPN microgels as a function of temperature at fixed concentration  $C_w=0.30\%$  and two pH values, 5 and 7. Full lines are guides for eyes.

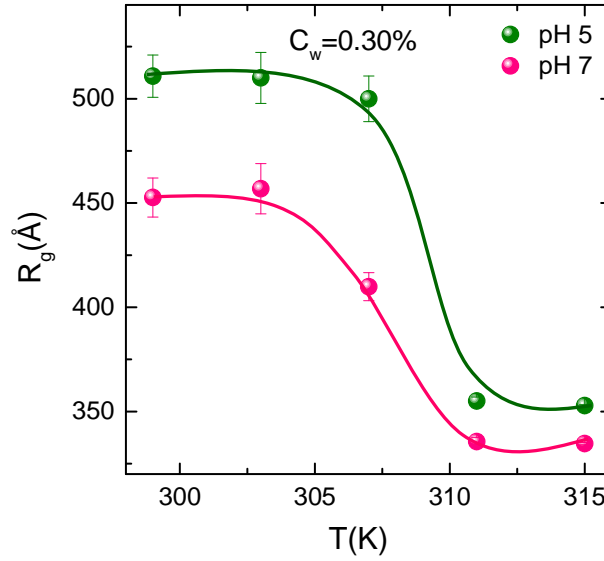


**Figure 3.38:** Gyration radius of the static inhomogeneities for  $D_2O$  suspensions of deprotonated IPN microgels as a function of temperature at fixed concentrations  $C_w=0.30\%$  at acidic and neutral pH conditions. Full lines are guides for eyes.

Fig.3.38 its behavior as a function of temperature at fixed weight concentration and at both pH 5 and 7 is reported. At variance with PNIPAM and IPN microgels, a decrease with temperature of  $R_g$  is observed, suggesting a more complex behavior. Indeed DLS measurements have shown that deprotonated IPN microgels exhibit a non-ergodic transition above the VPTT at concentrations higher or equal to  $C_w=0.30\%$ , at both acidic and neutral pH. In this framework the  $R_g$  behavior may be interpreted as the evidence of the non-ergodic transition, implying that the physical interpretation of  $R_g$  needs to be revised in view of the formation of a network of aggregates. Nevertheless a sharp discontinuity shows up around the expected VPTT at both pH 5 and 7, thus confirming that by deprotonating the carboxylic groups of PAAc, the two networks are independent and the sharpness of the transition is partially restored with respect to the case of pure PNIPAM.

A preliminary investigation of  $D_2O$  suspensions of deprotonated IPN microgels in the low dilution regime has evidenced new behaviors coming out clearly at higher concentrations. In Fig.3.39 the temperature behavior of collected spectra for deprotonated IPN microgels at  $C_w=2.80\%$  at acidic and neutral pH is reported. As for all the others samples, the spectral shape changes at both low and intermediate  $Q$  values, suggesting a temperature-dependent response. Nevertheless interesting differences at acidic and neutral pH are observed, highlighting a pH-dependent structural behavior for deprotonated IPN microgels. Indeed whilst at pH 5 a sharp transition is never observed and the spectral shape significantly changes only in the intermediate  $Q$  region, at pH 7 a sharp transition around 305 K is observed,

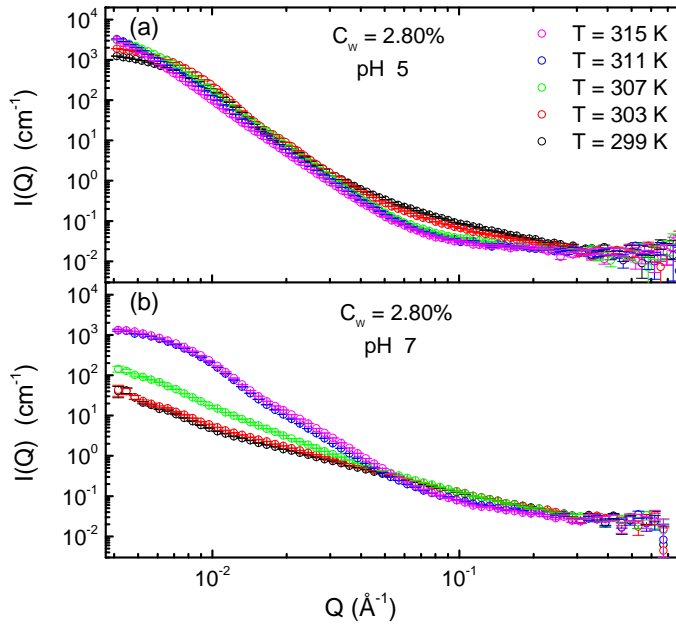


**Figure 3.39:** Differential cross-section for  $D_2O$  suspensions of deprotonated IPN microgels at  $C_w=2.80\%$  at acidic and neutral pH, in the temperature range  $T=(299 \div 315)$  K.

resembling the behavior of deprotonated IPN microgel in the high dilution regime.

Despite these evidences, the structural behavior at high concentrations cannot be rationalized through the model given by Eq.(2.84) in all the investigated temperature range. In particular the model properly fits at high temperature, whilst data and fits disagree at temperature below the VPTT, suggesting a more complex behavior emerging at high concentrations which may require different scattering functions to be described. Indeed the non-ergodic transition at high concentrations for deprotonated IPN microgels gives rise to structurally different arrested states whose nature has to be clarified. Therefore finding a suitable scattering function for analyzing the collected SANS data is crucial to obtain further details on their structural behavior across the VPT.

Moreover the Spin-Echo Small-Angle Neutron Scattering (SESANS) measurements, recently performed on the Offspec beamline at ISIS, are expected to provide new insights into the structural behavior of  $D_2O$  suspensions of IPN and deprotonated IPN microgels in a wide range of temperature, pH and concentrations. Nevertheless extrapolating information about the sample from the depolarization of the scattered neutrons is not trivial and is still in progress.

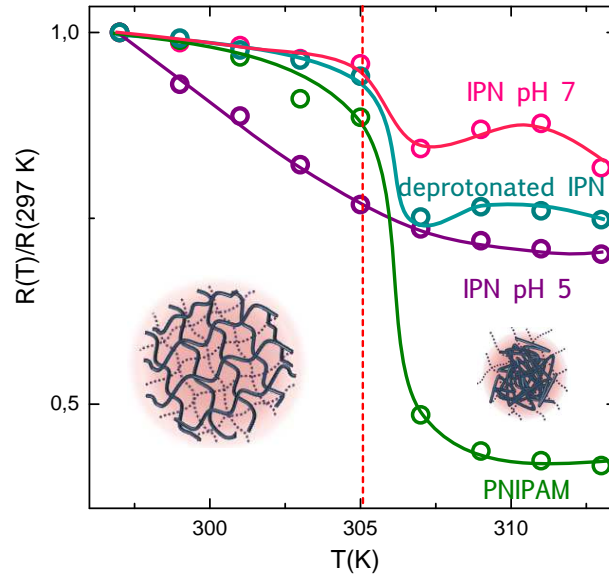


**Figure 3.40:** Temperature behavior of the normalized hydrodynamic radius obtained through DLS measurements, for aqueous suspensions of IPN microgels ( $C_w=0.1$  %) at pH 5, at pH 7 and deprotonated at pH 5, compared with PNIPAM microgels at the same weight concentration. Solid lines are guides for eyes.

### 3.3 Phase Diagram of IPN microgels

The combination of DLS and SANS measurements has allowed to investigate respectively the dynamics and the local structure of colloidal suspensions of IPN microgels.

In Fig.3.40 the temperature behavior of the normalized hydrodynamic radius as obtained from DLS is shown for aqueous suspensions of IPN microgels at the three investigated conditions, pH 5, pH 7 and deprotonated (at pH 5), as compared to PNIPAM microgels at the same weight concentration ( $C_w=0.10$  %). A cross-over from a swollen to a shrunken state is observed for all the samples at temperature  $T \approx 305$  K. Moreover the presence of acrylic acid in IPN microgels reduces the swelling capability with respect to PNIPAM microgels giving rise to a weaker transition. Furthermore the sharpness and the amplitude of the transition can be tuned by changing pH or by deprotonating the sample. In particular at high pH (pH 7, neutral conditions) the transition is sharper and narrower with respect to low pH (pH 5, acidic conditions).

This behavior is in full agreement with the results obtained through SANS measurements that evidenced, at both acidic and neutral pH conditions, an increase with temperature of the average size of the polymer-rich domains ( $R_g$ ) reflecting the transition from an inhomogeneous to a porous solid-like structure, due to the shrinking of the polymer chains. Moreover it has been found (see Fig.3.34)

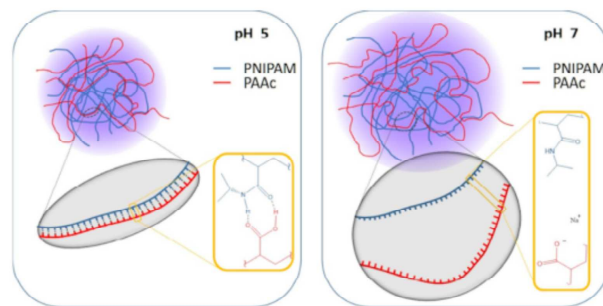


**Figure 3.41:** Cartoon of the H-bonds interaction between PAAc (red) and PNIPAM chains (blue) at acidic (left panel) and neutral (right panel) pH. Hydrogen bonds are formed when the pH of the solution is lower than the critical value of solubility of PAAc (pH 5) determining additional constraints to the interpenetrated network.

that at pH 5 the differences between polymer-rich/polymer-poor domains are less marked than at pH 7 where an evident discontinuity shows up with temperature, resembling PNIPAM microgel behavior.

This behavior can be interpreted by looking at the role played by the PAAc in IPN microgels. Indeed at low pH the acrylic acid is insoluble in water and is mainly in ionic state, H-bonds between its carboxylic ( $\text{COOH-}$ ) groups and the isopropyl ( $\text{CONH-}$ ) groups of PNIPAM are formed as shown in Fig.3.41 and make IPN microgels more hydrophobic. Therefore when heated above the VPTT, due to the increased hydrophobic interactions, IPN microgels expel a large amount of water giving rise to a very dense shrunken state. If the pH is increased above 5 (critical solubility value of PAAc) the carboxylic groups of PAAc are deprotonated, leading to a strong charge repulsion which limits the formation of hydrogen-bonds with PNIPAM (see Fig.3.41 right panel) so that the two networks result independent and the sharpness of the transition is partially restored with respect to the case of pure PNIPAM.

This mutual interference between PNIPAM and PAAc chains well explains the behavior of deprotonated IPN microgels. In this case in fact the carboxylic groups of PAAc are mainly deprotonated also at acidic pH and a sharp transition is observed at both pH.

The volume phase transition observed in IPN microgels can be considered as the driving mechanism of the ergodic-non ergodic transition found at higher concentrations. Indeed as the microgel particles collapse in the shrunken state at the VPTT ( $T \approx 305$  K), the viscosity and the structural relaxation time of the system dramatically increases until the system stops flowing and arrests. The comparison between DLS, SANS and visual inspection have allowed to draw a preliminary phase diagram for both water and heavy water suspensions of PNIPAM-PAAc IPN microgels across the VPT, in the temperature range  $T = (293 \div 313)$  K and

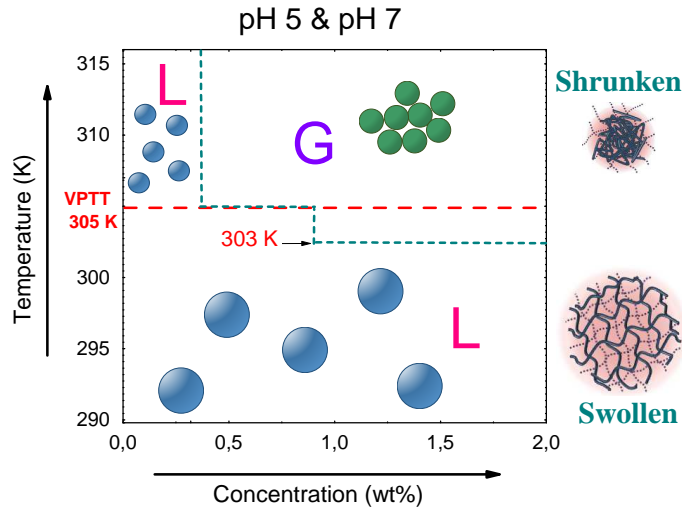


**Figure 3.42:** Phase diagram for aqueous suspensions of PNIPAM-PAAC IPN microgels upon crossing the VPT, in the range of temperature  $T=(293\div 313)$  K and of concentrations  $C_w=(0.05\div 1.64)$  % at both acidic and neutral pH. **L** indicates the liquid phase while **G** indicates the non-ergodic (Gel or Glass) state.

of concentrations  $C_w=(0.05\div 1.64)$  % at both acidic and neutral pH, as shown in Fig.3.42 and Fig.3.43 respectively for  $H_2O$  and  $D_2O$  solutions.

In the case of IPN aqueous suspensions (Fig.3.42) the same phase diagram is found for acidic and neutral pH. At low concentrations the system is always liquid (**L**) and the VPT is signaled by a change from a transparent to an opaque (even white) sample and by an increase of the viscosity. At higher concentrations, by crossing the VPT, the system undergoes a transition from a liquid phase (**L**) to a non-ergodic state (**G**), whose exact nature (of Gel or Glass) has to be further investigated. By increasing concentration this transition is shifted to lower temperature ( $T\approx 303$  K).

A similar phase diagram can be drawn for the  $D_2O$  suspensions of IPN microgels (Fig.3.43). In this case deuterium substitution affects the swelling kinetics and the volume phase transition of the microgel. Indeed a slowing down of the swelling kinetics is observed for IPN microgels in  $D_2O$  with respect to  $H_2O$ . This is probably due to the higher viscosity of  $D_2O$  and to the stronger polymer-solvent interactions in  $D_2O$  than in  $H_2O$ , which leads to stronger H-bonding with the water network (86). On the other hand interesting differences can be observed in the phase behavior: while  $H_2O$  samples undergo a non-ergodic transition at concentrations above  $C_w=0.32$  % at both acidic and neutral pH, in  $D_2O$  samples the arrested state is found only at neutral pH and at concentration above  $C_w=0.86$  %. This may suggest that the deuterium isotope effect on the dynamics of the system is not trivial and open the way to further investigations of the role played

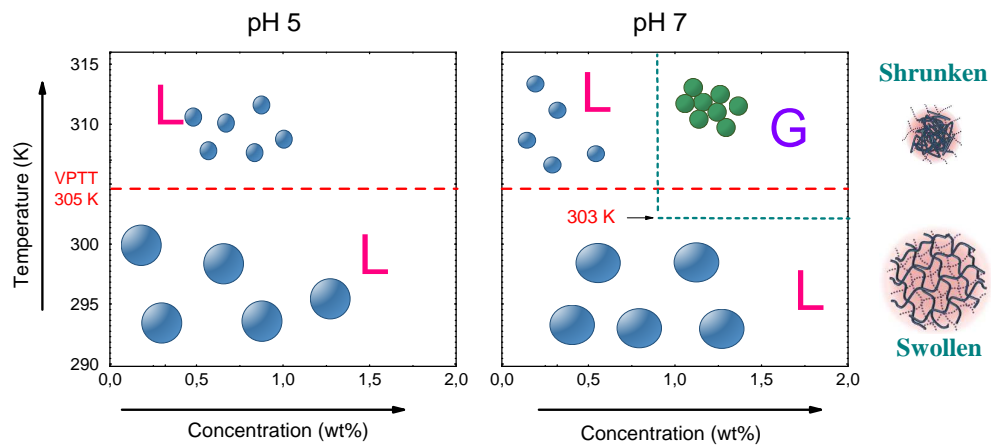


**Figure 3.43:** Phase diagram for heavy water suspensions of PNIPAM-PAAc IPN microgels upon crossing the VPT, in the range of temperature  $T=(293\div 313)$  K and of concentrations  $C_w=(0.05\div 1.64)$  % at both acidic and neutral pH. **L** indicates the liquid phase while **G** indicates the non-ergodic (Gel or Glass) state.

by H-bonding in the inter-particle interactions.

# Conclusions

In this thesis a systematic investigation of the dynamics and local interparticle structure of colloidal suspensions of IPN microgels based on PNIPAM and PAAc has been performed.

The dynamics of the system has been probed through Dynamic Light Scattering (DLS) in a range of scattering vector  $Q = (6.2 \times 10^{-4} \div 2.1 \times 10^{-3}) \text{ \AA}^{-1}$  and time window  $t = (10^{-6} \div 1) \text{ s}$ . The swelling behavior and the formation of an arrested state across the Volume Phase Transition (VPT) have been investigated as a function of temperature, pH and concentration both in  $H_2O$  and  $D_2O$  solutions. The H/D isotopic substitution is important either to understand the role played by the H-bonding in the dynamics of the system and also to get enough contrast in neutron scattering experiments.

The response of the local intraparticle structure across the VPT has been investigated through Small-Angle Neutron Scattering (SANS) in the  $Q$ -range  $(0.004 \div 0.7) \text{ \AA}^{-1}$  to get information about the topological inhomogeneities within each particle as a function of temperature, pH and concentration.

The following main results, discussed in this thesis, have been obtained:

- **Volume Phase Transition at low concentrations.**

- **Temperature and pH dependence of the VPT.** The presence of PAAc introduces an additional pH-sensitivity with respect to PNIPAM, originating interesting differences in the volume phase transition. In particular the system undergoes a VPT from a swollen hydrated state to a shrunken dehydrated one at temperature around  $305 - 307 \text{ K}$ , as in the case of pure PNIPAM microgels, with a reduced swelling capability. Moreover the VPT is sharper at pH 7 than at pH 5, with a discontinuous and a continuous transition respectively. Indeed the H-bondings between PNIPAM and PAAc are favored at acidic pH, where the acrylic acid is not solvated by water and the high hydrophobicity of the systems leads to a continuous but significant transition. On the contrary, at neutral pH, where the carboxylic groups of the PAAc are deprotonated and do not form H-bonds with the isopropyl groups of



PNIPAM, the two networks are independent and a sharper but weaker transition with respect to acidic pH is observed.

- **Concentration dependence of the VPT.** In the limit of high dilution ( $C_w = (0.10 \div 0.30) \%$ ) the relaxation time reaches the highest value at the highest concentration at neutral pH, while the concentration dependence is inverted at acidic pH.
  - **VPT in deprotonated samples.** The swelling capability of the PNIPAM network can be partially restored if, as a result of the synthesis procedure, the carboxylic groups of PAAc are deprotonated. In this case a sharp transition is observed at both acidic and neutral pH, even if it results sharper and sharper as the pH is increased. The concentration dependence of the relaxation time is in agreement with the behavior observed for neutral not deprotonated samples: the highest value of the relaxation time is reached at the highest concentration.
- **Non-ergodic transition at high concentrations.**
    - **Ergodic to non-ergodic transition across the VPT.** At low concentrations the systems is liquid below and above the VPT, while by increasing concentrations a transition from a liquid to a non-ergodic state across the VPT is observed for  $C_w \geq 0.32 \%$ . This transition is pH dependent, becoming sharper and sharper with increasing pH.
  - **Effect of isotopic substitution in the solvent.** H/D isotopic substitution plays an important role on the kinetics of the swelling, preserving the same physical properties of the swelling behavior in  $H_2O$ , but affecting its time scale.
    - **Volume Phase Transition at low concentrations.** Same phenomenology is observed in  $D_2O$  and in  $H_2O$ , even if the VPT Temperature (VPTT) is shifted forward in deuterated samples, mainly arising from the higher viscosity in  $D_2O$  than in  $H_2O$ .
    - **Non-ergodic transition at high concentrations.** The presence of  $D_2O$  affects the phase behavior at high concentrations making more hard to achieve the non-ergodic state. In particular at acidic pH and in the investigated range of concentrations the system remains fluid above the VPT, although a huge increase of the viscosity is observed with concentration. At neutral pH the non-ergodic state is reached above the VPT only for the highest concentrated samples ( $C_w \geq 0.86 \%$ ).
  - **Intraparticle structural transition across the VPT.**

- **Model.** The model proposed by Shibayama and coworkers for pure PNIPAM microgels to describe the topological inhomogeneities due to the presence of cross-links has been successfully applied to pure PNIPAM and IPN microgels of PNIPAM and PAAc.
- **Temperature and pH dependence of intraparticle structural transition.** The local intraparticle structure undergoes a structural transition from a water-rich open inhomogeneous structure to a homogeneous porous solid-like one, associated to the collapse of the polymer chains across the VPT. In particular below the VPT, when the microgel particles are fully swollen, the local structure of the network is characterized by regions with restricted dynamics due to the elastic constraints brought about by the presence of crosslinking sites. Their typical size  $R_g$  depends on pH and weight concentration, due to the different elastic responses of the sample. Above the VPT, when water is expelled from the particles, a transition to a more homogeneous local structure is found as a consequence of the shrinking of the network and this structure is characterized by shorter mesh size and larger domains of static inhomogeneities, separated by smoother interfaces. Moreover the H-bonding between PNIPAM and PAAc at pH 5 leads to additional topological constraints which are not present at pH 7.
- **Concentration dependence of the intraparticle structural transition.** The behavior of the relevant parameters confirms the concentration dependence observed through DLS measurements. Indeed at pH 5 the less concentrated sample exhibits the more intense response to temperature changes, while at pH 7, the opposite trend is observed.

The combination of all the listed results has allowed to draw preliminary temperature-concentration phase diagrams as a function of pH and solvent conditions. Two main regions have been distinguished varying the concentrations: at low  $C_w$ , across the VPTT, a transition from a swollen to a shrunken fluid is found, while the scenario is completely different at high  $C_w$  where an arrested state is found above the VPTT except for the case of IPN microgels in heavy water at acidic conditions. These findings open the way to further investigations in the formation of arrested states in this smart IPN microgel belonging to the intriguing class of soft colloids.

# Bibliography

- [1] P. J. LU, E. ZACCARELLI, F. CIULLA, A. B. SCHOFIELD, F. SCIORTINO, AND D. A. WEITZ. **Gelation of particle with short range attraction.** *Nature*, **453**:499–503, 2008. 1, 5, 9
- [2] C. P. ROYALL, S. R. WILLIAMS, T. OHTSUKA, AND H. TANAKA. **Direct observation of a local structural mechanism for dynamical arrest.** *Nat. Mater.*, **7**:556–561, 2008. 1, 5
- [3] B. RUZICKA, E. ZACCARELLI, L. ZULIAN, R. ANGELINI, M. SZTUCKI, A. MOUSSAÏD, T. NARAYANAN, AND F. SCIORTINO. **Observation of empty liquids and equilibrium gels in a colloidal clay.** *Nat. Mater.*, **10**:56, 2011. 1, 5
- [4] P. N. PUSEY AND W. VAN MEGEN. **Phase behaviour of concentrated suspensions of nearly hard colloidal spheres.** *Nature*, **320**:340, 1986. 1, 5, 6
- [5] A. IMHOF AND J. K. G. DHONT. **Experimental Phase Diagram of a Binary Colloidal Hard-Sphere Mixture with a Large Size Ratio.** *Phys. Rev. Lett.*, **75**:1662–1665, 1995. 1, 5
- [6] K. N. PHAM, A. M. PUERTAS, J. BERGENHOLTZ, S. U. EGELHAAF, A. MOUSSAÏD, P. N. PUSEY, A. B. SCHOFIELD, M. E. CATES, M. FUCHS, AND W. C. K. POON. **Multiple Glassy States in a Simple Model System.** *Science*, **296**:104, 2002. 1, 5, 7
- [7] T. ECKERT AND E. BARTSCH. **Re-entrant glass transition in a colloid-polymer mixture with depletion attractions.** *Phys. Rev. Lett.*, **89**:125701, 2002. 1, 5, 7
- [8] R. ANGELINI, E. ZACCARELLI, F. A. DE MELO MARQUES, M. SZTUCKI, A. FLUERASU, G. RUOCCO, AND B. RUZICKA. **Glass-glass transition during aging of a colloidal clay.** *Nat. Commun.*, **5**:4049, 2014. 1, 5

- [9] C. N. LIKOS, N. HOFFMANN, H. LÖWEN, AND A. A. LOUIS. **Exotic fluids and crystals of soft polymeric colloids.** *J. Phys. Cond. Matter*, **14**:7681–7698, 2002. 1, 5, 9
- [10] P. E. RAMÍREZ-GONZÁLEZ AND M. MEDINA-NOYOLA. **Glass transition in soft-sphere dispersions.** *J. Phys. Cond. Matter*, **21**:075101, 2009. 1, 5, 9
- [11] D. M. HEYES, S. M. CLARKE, AND A. C. BRANK. **Elasticity of compressed microgel suspensions.** *J. Chem. Phys*, **131**:204506, 2009. 1, 5, 9
- [12] L. A. LYON AND A. FERNANDEZ-NIEVES. **The Polymer/Colloid Duality of Microgel Suspensions.** *Annu. Rev. Phys. Chem.*, **63**:25–43, 2012. 1, 9, 11, 22, 29
- [13] D. PALOLI, P. S. MOHANTY, J. J. CRASSOUS, E. ZACCARELLI, AND P. SCHURTENBERGER. **Fluid–solid transitions in soft-repulsive colloids.** *Soft Matter*, 2012. 1, 2, 9, 22, 24
- [14] P. S. MOHANTY, D. PALOLI, J. J. CRASSOUS, E. ZACCARELLI, AND P. SCHURTENBERGER. **Effective interactions between soft-repulsive colloids: Experiments, theory and simulations.** *J. Chem. Phys.*, **140**:094901, 2014. 1, 2, 9, 22, 24, 25
- [15] B. R. SAUNDERS AND B. VINCENT. **Microgels particles as model colloids: theory, properties and applications.** *Adv. Colloid Interface Sci.*, **80**:1–25, 1999. 1, 12
- [16] R. H. PELTON. **Temperature-sensitive aqueous microgels.** *Adv. Colloid Interface Sci.*, **85**:1–33, 2000. 1, 12, 26
- [17] S. V. VINOGRADOV. **Colloidal microgels in drug delivery applications.** *Curr. Pharm. Des.*, **12**:4703–4712, 2006. 1
- [18] M. DAS, H. ZHANG, AND E. KUMACHEVA. **MICROGELS: Old Materials with New Applications.** *Annu. Rev. Mater. Res.*, **36**:117–142, 2006. 1, 12
- [19] J. S. PARK, H. N. YANG, D. G. WOO, S. Y. JEON, AND K. H. PARK. **Poly(N-isopropylacrylamide-co-acrylic acid) nanogels for tracing and delivering genes to human mesenchymal stem cells.** *Biomaterials*, **34**:8819–8834, 2013. 2, 12

- [20] M. HAMIDI, A. AZADI, AND P. RAFIE. **Hydrogel nanoparticles in drug delivery.** *Adv. Drug Deliv. Rev.*, **60**:1638–1649, 2008. 2
- [21] N. M. B. SMEETS AND T. HOARE. **Designing Responsive Microgels for Drug Delivery Applications.** *J. Polym. Sci. A Polym. Chem.*, **51**:3027–3043, 2013. 2, 12
- [22] S. SU, ALI MD. MONSUR, C. D. M. FILIPE, Y. LI, AND R. H. PELTON. **Microgel-Based Inks for Paper-Supported Biosensing Applications.** *Biomacromolecules*, **9**:935–9419, 2008. 2, 12
- [23] H. WANG, X. WU, Z. ZHU, C. S. LIU, AND Z. ZHANG. **Revisit to phase diagram of poly(N-isopropylacrylamide) microgel suspensions by mechanical spectroscopy.** *J. Chem. Phys.*, **140**:024908, 2014. 2, 23, 24, 25
- [24] T. HELLWEG, C.D. DEWHURST, E. BRÜCKNER, K.KRATZ, AND W.EIMER. **Colloidal crystals made of poly(N-isopropylacrylamide) microgel particles.** *Colloid. Polym. Sci.*, **278**:972–978, 2000. 2, 23
- [25] J. WU, B. ZHOU, AND Z. HU. **Phase behavior of thermally responsive microgel colloids.** *Phys. Rev. Lett.*, **90**(4):048304, 2003. 2, 23
- [26] Z. HU AND X. XIA. **Hydrogel nanoparticle dispersions with inverse thermoreversible gelation.** *Adv. Mater.*, **16**(4):305–309, 2004. 2, 28, 66
- [27] X. XIA AND Z. HU. **Synthesis and Light Scattering Study of Microgels with Interpenetrating Polymer Networks.** *Langmuir*, **20**:2094–2098, 2004. 2, 28, 29, 30, 65, 79, 80
- [28] J. MA, B. FAN, B. LIANG, AND J. XU. **Synthesis and characterization of Poly(N-isopropylacrylamide)/Poly(acrylic acid) semi-IPN nanocomposite microgels.** *J. Colloid Interface Sci.*, **341**:88–93, 2010. 2, 27, 28, 29
- [29] Z. XING, C. WANG, J. YAN, L. ZHANG, L. LI, AND L. ZHA. **pH/temperature dual stimuli-responsive microcapsules with interpenetrating polymer network structure.** *Colloid Polym. Sci.*, **288**:1723–1729, 2010. 2, 28
- [30] K. KRATZ, T. HELLWEG, AND W. EIMER. **Influence of charge density on the swelling of colloidal poly(N-isopropylacrylamide-co-acrylic acid) microgels.** *Colloids Surf. A*, **170**:137–149, 2000. 2, 27, 28, 29

- [31] C. D. JONES AND L. A. LYON. **Synthesis and Characterization of Multiresponsive Core-Shell Microgels.** *Macromolecules*, **33**:8301–8303, 2000. 2, 28
- [32] Z. MENG, J. K. CHO, S. DEBORD, V. BREEDVELD, AND L. A. LYON. **Crystallization Behavior of Soft, Attractive Microgels.** *J. Phys. Chem. B*, **111**:6992–6997, 2007. 2, 23, 27, 28, 29, 30
- [33] J. ZHOU, G. WANG, L. ZOU, L. TANG, M. MARQUEZ, AND Z. HU. **Viscoelastic Behavior and In Vivo Release Study of Microgel Dispersions with Inverse Thermoreversible Gelation.** *Biomacromolecules*, **9**:142–148, 2008. 2, 28
- [34] C. N. LIKOS. **Effective interactions in soft condensed matter physics.** *Phys. Rep.*, **348**:267–439, 2001. 5, 7, 9
- [35] E. ZACCARELLI. **Colloidal Gels: Equilibrium and Non-Equilibrium Routes.** *J. Phys.: Condens. Matter*, **19**:323101, 2007. 5, 9
- [36] E. ZACCARELLI, G. FOFFI, K. A. DAWSON, S. V. BULDYREV, F. SCIORTINO, AND P. TARTAGLIA. **Confirmation of anomalous dynamical arrest in attractive colloids: A molecular dynamics study.** *Phys. Rev. E*, **66**:041402, 2002. 5, 7
- [37] E. ZACCARELLI, F. SCIORTINO, AND P. TARTAGLIA. **Numerical study of the glass-glass transition in short-ranged attractive colloids.** *J. Phys.: Condens. Matter*, **16**:S4849–S4860, 2004. 5
- [38] A. M. PUERTAS, E. ZACCARELLI, AND F. SCIORTINO. **Viscoelastic properties of attractive and repulsive colloidal glasses.** *J. Phys.: Cond. Matt.*, **17**:021501, 2005. 5
- [39] P. N. PUSEY, E. ZACCARELLI, C. VALERIANI, E. SANZ, W. C. K. POON, AND M. E. CATES. **Viscoelastic properties of attractive and repulsive colloidal glasses.** *Phil. Trans. R. Soc. A*, **367**:4993– 5011, 2009. 5
- [40] W. GÖTZE. *Liquids, Freezing and Glass Transition*, page 287. 1991. 5
- [41] L. FABBIAN, W. GÖTZE, F. SCIORTINO, P. TARTAGLIA, AND F. THIERY. **Ideal glass-glass transitions and logarithmic decay of correlations in a simple system.** *Phys. Rev. E*, **59**:1347–1350, 1998. 5, 7

- [42] W. VAN MEGEN AND S. M. UNDERWOOD. **Glass Transition in Colloidal Hard Spheres: Mode-Coupling Theory Analysis.** *Phys. Rev. Lett.*, **70**:2766, 1993. 6
- [43] W. VAN MEGEN AND S. M. UNDERWOOD. **Glass transition in colloidal hard spheres: Measurement and mode-coupling-theory analysis of the coherent intermediate scattering function.** *Phys. Rev. E*, **49**:4206–4220, 1994. 6
- [44] J. ZHU, M. LI, R. ROGERS, W. MEYER, R. H. OTTEWILL, STS-73 SPACE SHUTTLE CREW, W. B. RUSSEL, AND P. M. CHAIKIN. **Crystallization of hard-sphere colloids in microgravity.** *Nature*, **387**:883–885, 1997. 7
- [45] M. D. RINTOUL AND S. TORQUATO. **Metastability and Crystallization in Hard-Sphere Systems.** *Phys. Rev. Lett.*, **77**:4198–4201, 1996. 7
- [46] G. BRAMBILLA, D. EL MASRI, M. PIERNO, L. BERTHIER, AND L. CIPELLETTI. **Probing the Equilibrium Dynamics of Colloidal Hard Spheres above the Mode-Coupling Glass Transition.** *Phys. Rev. Lett.*, **102**, 2009. 7
- [47] J. BERGENHOLTZ AND M. FUCHS. **Nonergodicity transitions in colloidal suspensions with attractive interactions.** *Phys. Rev. E*, **59**:5706, 1999. 7
- [48] E. ZACCARELLI, S. V. BULDYREV, F. SCIORTINO, AND P. TARTAGLIA. *Short-ranged attractive colloids: What is the gel state?*, pages 181–194. *Unifying Concepts in Granular Media and Glasses*. Elsevier, Amsterdam, 2004. 7
- [49] P. J. FLORY. **Molecular Size Distribution in Three Dimensional Polymers. I. Gelation.** *J. Am. Chem. Soc.*, **63**:3083–3090, 1941. 8
- [50] W. H. STOCKMAYER. **Theory of Molecular Size Distribution and Gel Formation in Branched - Chain Polymers.** *J. Chem. Phys.*, **11**, 1943. 8
- [51] E. ZACCARELLI, C. MAYER, A. ASTERIADI, C. N. LIKOS, F. SCIORTINO, J. ROOVERS, H. IATROU, N. HADJICHRISTIDIS, P. TARTAGLIA, H. LÖWEN, AND D. VLASSOPOULOS. **Tailoring the flow of soft glasses by soft additives.** *Phys. Rev. E*, **95**:268301, 2005. 9
- [52] C. VON FERBER, A. JUSUFI, M. WATZLAWEK, C. N. LIKOS, AND H. LÖWEN. **Polydisperse star polymer solutions.** *Phys. Rev. E*, **62**:6949–6956, 2000. 9
- [53] H. TANAKA, J. MEUNIER, AND D. BONN. **Nonergodic states of charged colloidal suspensions: Repulsive and attractive glasses and gels.** *Phys. Rev. E*, **69**:031404, 2004. 10

- [54] K. DUŠ AND D. PATTERSON. **Transition in swollen polymer networks induced by intramolecular condensation.** *J. Polym. Sci. Par. A-2*, **6**:1209–1216, 1968. 11
- [55] T. TANAKA. **Collapse of gels and the critical gelpoints .** *Phys. Rev. Lett.*, **40**:820–823, 1978. 11
- [56] J. HROUZ, M. ILAVSKÝ, K. ULBRICH, AND J. KOPEČEK. **The photoelastic behaviour of dry and swollen networks of poly (N,N-diethylacrylamide) and of its copolymer with N-tert.butylacrylamide.** *Europ. Polym. J.*, **17**:361–366, 1981. 11
- [57] M. KARG AND T. HELLWEG. **New “smart” poly(NIPAM) microgels and nanoparticle microgel hybrids: Properties and advances in characterisation.** *Curr. Opin. Colloid Interface Sci.*, **14**:438–450, 2009. 12
- [58] P. SCHEXNAILDER AND G. SCHMIDT. **Nanocomposite polymer hydrogels.** *Colloid. Polym. Sci.*, **287**:1–11, 2009. 12
- [59] A.K. LELE, M.M. HIRVE, M.V. BADIGER, AND R.A. MASHELKAR. **Predictions of bound water content in poly (N-isopropylacrylamide) gel.** *Macromolecules*, **30**:157–159, 1998. 12
- [60] T. HINO AND J. M. PRAUSNITZ. **Swelling Equilibria for Heterogeneous Polyacrylamide Gels.** *J. Appl. Polym. Sci*, **62**:1635–1640, 1996. 12, 13
- [61] P.J. FLORY. *Principles of Polymer Chemistry.* Cornell University, Ithaca, New York, 1953. 12, 13, 15, 20
- [62] K. OTAKE, H. INOMATA, M. KONNO, AND S. SAITO. **Thermal-analysis of the volume phase-transition with N-Isopropylacrylamide gels.** *Macromolecules*, **23**:283–289, 1990. 12
- [63] J. WU, G. HUANG, AND Z. HU. **Interparticle Potential and the Phase Behavior of Temperature-Sensitive Microgel Dispersions.** *Macromolecules*, **36**:440–448, 2003. 15
- [64] W.B. RUSSEL, D.A. SAVILLE, AND W.R. SCHOWALTER. *Colloidal Dispersions.* Cambridge University, Cambridge, England, 1992. 16
- [65] S. MALLAM, F. HORKAY, A. M. HECHT, A. R. RENNIE, AND E. GEISSLER. **Microscopic and macroscopic thermodynamic observations in swollen poly(dimethylsiloxane) networks.** *Macromolecules*, **24**:543–548, 1991. 16, 63



- [66] M. SHIBAYAMA, T. TANAKA, AND C. C. HAN. **Small angle neutron scattering study of poly(N-isopropyl acrylamide) gels near their volume-phase transition temperature.** *J. Chem. Phys.*, **97**:6829, 1992. 16, 17, 18, 21, 63, 97, 101
- [67] M. SHIBAYAMA. **Small angle neutron scattering on polymer gels: phase behavior, inhomogeneities and deformation mechanisms.** *Polym. J.*, **43**:18–34, 2011. 16, 17, 18, 63, 97, 101
- [68] F. IKKAI AND M. SHIBAYAMA. **Static Inhomogeneities in Thermoreversible Physical Gels.** *Phys. Rev. Lett.*, **82**:24, 1999. 16, 18
- [69] F. IKKAI AND M. SHIBAYAMA. **Gel-size dependence of temperature-induced microphase separation in weakly-charged polymer gels.** *Polym. J.*, **48**:2387–2394, 2007. 16, 18
- [70] T. SUZUKI, T. KARINO, F. IKKAI, AND M. SHIBAYAMA. **pH dependence of macroscopic swelling and microscopic structures for thermo/pH-sensitive gels wit different charge distributions.** *Macromolecules*, **41**:9882–9889, 2008. 16, 18
- [71] N. GUNDOGAN, O. OKAY, AND W. OPPERMAN. **Swelling, Elasticity and Spatial Inhomogeneity of Poly(N,N-dimethylacrylamide) Hydrogels Formed at Various Polymer Concentrations.** *Macromol. Chem. Phys.*, **205**:814–823, 2004. 17
- [72] J. BASTIDE AND L. LEIBLER. **Large-scale heterogeneities in randomly cross-linked networks.** *Macromolecules*, **21**:2647, 1998. 17
- [73] P.M. DOTY, B.H. ZIMM, AND R. S. STEIN. **Classical theory of light scattering from solutions. A review.** *Polym. Bull.*, **1**, 1945. 17
- [74] B.H. ZIMM. **The scattering of light and the radial distribution function of high polymer solutions.** *J.Chem.Phys.*, **16**:1093–1099, 1948. 17
- [75] G.C. BERRY. *Soft-Matter Characterization*, **1**, pages 41–132. Springer, Würzburg, 1977. 17
- [76] M. SHIBAYAMA. **Spatial inhomogeneity and dynamic fluctuations of polymer gels.** *Macromol. Chem. Phys.*, **199**:1–30, 1998. 18, 63

- [77] S. PANYUKOV AND Y. RABIN. **Statistical physics of polymer gels.** *Phys. Rep.*, **269**:1–132, 1996. 19
- [78] J. MATTSSON, H. M. WYSS, A. FERNANDEZ-NIEVES, K. MIYAZAKI, Z. HU, D. REICHMAN, AND D. A. WEITZ. **Soft colloids make strong glasses.** *Nature*, **462**(5):83–86, 2009. 22, 79, 80, 81
- [79] S. TANG, Z. HU, Z. CHENG, AND J. WU. **Crystallization Kinetics of Thermosensitive Colloids Probed by Transmission Spectroscopy.** *Langmuir*, **20**:8858–8864, 2004. 23
- [80] Y. WANG, G. YANG, P. TANG, F. QIU, Y. YANG, AND L. ZHU. **Mixed homopolymer brushes grafted onto a nanosphere.** *J. Chem. Phys.*, **134**:134903, 2011. 26
- [81] F. SCHEFFOLD, P. DÍAZ-LEYVA, M. REUFER, N.B. BRAHAM, I. LYNCH, AND J. L. HARDEN. **Brush-like Interactions between Thermoresponsive Microgel Particles.** *Phys. Rev. Lett.*, **104**:128304, 2012. 26
- [82] R. ROMEO AND M.P. CIAMARRA. **Elasticity of compressed microgel suspensions.** *Soft Matter*, **9**:5401–5406, 2013. 26
- [83] T. PATEL, G. GHOSH, S. YUSA, AND P. BAHADUR. **Solution Behavior of Poly(n-Isopropylacrylamide) in Water: Effect of Additives.** *J. Dispersion Sci. Technol.*, **32**:1111–1118, 2011. 26, 27
- [84] X. WU, R. H. PELTON, A. E. HAMIELEC, D. R. WOODS, AND W. MCPHEE. **The kinetics of poly(N-isopropylacrylamide) microgel latex formation .** *Colloid. Polym. Sci.*, **272**:467–477, 1994. 27
- [85] P. W. ZHU AND D. H. NAPPER. **Light scattering studies of poly(N-isopropylacrylamide) microgel particle in mixed water-acetic acid solvents.** *Macromol. Chem. Phys.*, **200**:1950–1955, 1999. 27
- [86] H. SHIROTA AND K. HORIE. **Deuterium Substitution and Fluorescence Studies on Polymer Hydrogels and Complexes.** *Macromol. Symp.*, **207**:79–93, 2004. 27, 95, 114
- [87] K. KRATZ, T. HELLWEG, AND W. EIMER. **Effect of connectivity and charge density on the swelling and local structure and dynamic properties of colloidal PNIPAM microgels.** *Ber. Bunsenges. Phys. Chem.*, **102**(11):1603–1608, 1998. 28

- [88] W. XIONG, X. GAO, Y. ZAO, H. XU, AND X. YANG. **The dual temperature/pH-sensitive multiphase behavior of poly(Nisopropylacrylamide-co-acrylic acid) microgels for potential application in *in situ* gelling system.** *Colloids Surf. B: Biointerfaces*, **84**:103–110, 2011. 28
- [89] L. A. LYON, J. D. DEBORD, S. B. DEBORD, C. D. JONES, J. G. MCGRATH, AND M. J. SERPE. **Microgel Colloidal Crystals.** *J. Phys. Chem. B*, **108**:19099–19108, 2004. 28
- [90] P. HOLMQVIST, P. S. MOHANTY, G. NÄGELE, P. SCHURTENBERGER, AND M. HEINEN. **Structure and Dynamics of Loosely Cross-Linked Ionic Microgel Dispersions in the Fluid Regime.** *Phys. Rev. Lett.*, **109**:048302, 2012. 28
- [91] S. B. DEBORD AND L. A. LYON. **Influence of Particle Volume Fraction on Packing in Responsive Hydrogel Colloidal Crystals.** *J. Phys. Chem. B*, **107**:2927–2932, 2003. 28
- [92] X. XIA, Z. HUA, AND M. MARQUEZ. **Physically bonded nanoparticle networks: a novel drug delivery system.** *J. Control. Release*, **103**:21–30, 2005. 28
- [93] X. LIU, H. GUO, AND L. ZHA. **Study of pH/temperature dual stimuli-responsive nanogels with interpenetrating polymer network structure.** *Polymers*, **61**(7):1144–1150, 2012. 28
- [94] E. SIBAND, Y. TRAN, AND D. HOURDET. **Thermoresponsive Interpolyelectrolyte Complexation: Application to Macromolecular Assemblies.** *Macromolecules*, **44**, 2011. 29
- [95] B.J. BERNE AND R. PECORA. *Dynamic Light Scattering*. Wiley, New York, 1976. 34, 37
- [96] R. KOHLRAUSCH. **Thermoresponsive poly-(N-isopropylmethacrylamide) microgels: Tailoring particle size by interfacial tension control.** *Pogg. Ann. Phys. Chem.*, **91**:179–214, 1854. 43
- [97] G. WILLIAMS AND D. C. WATTS. **Non-Symmetrical Dielectric Relaxation Behavior Arising from a Simple Empirical Decay Function.** *J. Chem. Soc. Faraday Trans.*, **66**:80–85, 1970. 43

- [98] F. IANNI AND R. DI LEONARDO AND S. GENTILINI AND G. RUOCCO. **Aging after shear rejuvenation in a soft glassy colloidal suspension: Evidence for two different regimes.** *Phys. Rev. E*, **75**:011408, 2007. 44
- [99] R.J. ROE. *Methods of X-ray and Neutron Scattering in Polymer Science*. Oxford University Press, 2000. 46, 54
- [100] V.F. SEARS. *Electromagnetic Neutron-Atom Interactions*, **5**, pages 281–317. Physics Reports, North-Holland, Amsterdam, 1986. 46
- [101] J.S. HIGGINS AND H. C. BENOÎT. *Polymers and Neutron Scattering*, **8** of *Oxford Series on Neutron Scattering in Condensed Matter*. Clarendon Press, 1994. 50, 54
- [102] L.A. FEIGIN AND D.I. SVERGUN. *Structure Analysis by Small-Angle X-Ray and Neutron Scattering*. Princeton Resources Princeton, New Jersey, 1987. 58
- [103] S.M. KING. **Small Angle Neutron Scattering.** *Commentary published by Bristol Colloid entre*, 2002. 58
- [104] **ISIS-TS2 is the second target station of the ISIS pulsed neutron source operating in the UK. More information is available on the website: <http://www.isis.stfc.ac.uk/>.** 64
- [105] V. NIGRO, R. ANGELINI, M. BERTOLDO, V. CASTELVETRO, G. RUOCCO, AND B. RUZICKA. **Dynamic light scattering study of temperature and pH sensitive colloidal microgels.** *J. Non-Cryst. Solids*, **407**:361 – 366, 2015. 75
- [106] J. COLMENERO, A. ALEGRÍA, J. M. ALBERDI, F. ALVAREZ, AND B. FRICK. **Dynamics of the  $\alpha$  relaxation of a glass-forming polymeric system: Dielectric, mechanical, nuclear-magnetic-resonance, and neutron scattering studies.** *Phys. Rev. B*, **44**:7321–7329, 1991. 81
- [107] J. COLMENERO, A. ALEGRÍA, AND A. ARBE. **Correlation between Non-Debye behavior and  $Q$ -behavior of the  $\alpha$ -relaxation in glass-forming polymeric systems.** *Phys. Rev. Lett.*, **69**:478–481, 1992. 81
- [108] B. SIERRA-MARTIN, J. R. RETAMA, M. LAURENTI, A. F. BARBERO, AND E. L. CABARCOS. **Structure and polymer dynamics within PNIPAM-based microgel particles.** *Adv. Colloid Interface Sci.*, **205**:113–123, 2014. 97, 101
- [109] V. NIGRO, R. ANGELINI, M. BERTOLDO, F. BRUNI, M.A. RICCI, AND B. RUZICKA. **Local structure of temperature and pH-sensitive colloidal microgels.** *J. Chem. Phys.*, **143**:114904, 2015. 101

- 
- [110] G. SUDRE, D. HOURDET, C. CRETON, F. COUSIN, AND Y. TRAN. **Probing pH-Responsive Interactions between Polymer Brushed and Hydrogels by Neutron Reflectivity.** *Langmuir*, **30**:9700–9706, 2014. 104

## Acknowledgements

I would like to acknowledge Prof. Maria Antonietta Ricci, my scientific supervisor at the University "Roma Tre", for giving me the possibility to deeply learn about the neutron scattering technique. At the same time I want to thank Dr. Barbara Ruzicka and Dr. Roberta Angelini, my co-supervisors from the University "La Sapienza" of Roma, for introducing me to the soft matter science and the light scattering techniques. Thank you all for guiding me during this Ph.D. with scientific rigor and dedication and for your support since the very early stages.

I would also like to thank Dr. Monica Bertoldo and her co-workers for the chemical synthesis of all the samples I have characterized in these years. I want to thank Prof. Fabio Bruni for its interest and help in my work. A particular thank go to Dr. Emanuela Zaccarelli, the referee of my thesis, for the critical reading of the manuscript and her precious scientific advices.

I would like to thank all the people who shared with me these three years, making the Ph.D. time much nicer: Laura, Eleonora and Annalaura, my colleagues at University "Roma Tre", Dr. Armida Sodo e Dr. Alfonso Russo, I thank you for the time spent together and your advices and patience.

Finally I'm grateful to all my family, my sister and my parents, for making this possible through their never-ending support and a big thank go to Claudio, who has always encouraged me and taken care of me over the last years.

Valentina Nigro, Rome, January 2016